Calorimetry of a Phase Slip in a Josephson Junction

Mehmet Efe Gumus

THÈSE

Pour obtenir le grade de

DOCTEUR DE L'UNIVERSITÉ GRENOBLE ALPES

École doctorale : PHYS - Physique
Spécialité : Nanophysique
Unité de recherche : Institut Néel

Calorimétrie d'un saut de phase dans une jonction Josephson

Calorimetry of a Phase Slip in a Josephson Junction

Présentée par :

MEHMET EFE GÜMÜŞ

Direction de thèse :

Clemens WINKELMANN Maître de conférences HDR, Grenoble INP	Directeur de thèse
Hervé COURTOIS Professeur des Universités, Université Grenoble Alpes	Co-directeur de thèse

Rapporteurs :

HUGUES POTHIER
Directeur de recherche, CEA CENTRE DE PARIS-SACLAY
VILLE MAISI
Professeur associé, Lunds Universitet

Thèse soutenue publiquement le **28 avril 2023**, devant le jury composé de :

BENJAMIN HUARD Professeur des Universités, ENS DE LYON	Examinateur
JULIA MEYER Professeur des Universités, UNIVERSITE GRENOBLE ALPES	Présidente
HUGUES POTHIER Directeur de recherche, CEA CENTRE DE PARIS-SACLAY	Rapporteur
VILLE MAISI Professeur associé, Lunds Universitet	Rapporteur

Contents

Abstract

Magnetic flux which is continuous quantity in the classical world, becomes quantized when confined at the center of a superconducting loop. A quantum of flux can penetrate in/out of the loop under certain conditions via thermal activation or macroscopic quantum tunneling. Josephson junction, a key building block of the superconducting quantum devices, provides a straightforward implementation of this event where the transfer of a Cooper pair between the two superconducting reservoirs is visualized as the transverse tunneling of the magnetic flux quantum.

By bringing these concepts together in a superconducting quantum interference device (SQUID), it becomes possible to generate a so-called phase slip where a flux quantum enters/leaves the loop and the superconducting phase winds by 2π in a deterministic manner. This event is of dissipative nature when the SQUID operates in the strongly screening (hysteretic) regime therefore can be detected via calorimetry methods.

In this thesis, we demonstrate the real time detection of a phase slip which is manifested as the abrupt increase and the subsequent relaxation of the electronic temperature of the Normal island placed in the SQUID loop as a weak link. The system is embedded in a microwave resonator. The phase slips are generated by nanosecond pulses sent on an on-chip flux line, and the temperature excursion is read via the variation of the transmitted power by exploiting the proximity effect as a secondary thermometer.

By addressing the observation of an elementary dissipative event, this work provides an insight on the role of dissipation ubiquitous in superconducting devices and showcases the potential use of the fast nano-calorimeters in the field of quantum sensors.

Resumé

Le flux magnétique qui est une quantité continue dans le monde classique, devient quantifié lorsqu'il est confiné au centre d'une boucle supraconductrice. Un quantum de flux peut pénétrer ou quitter la boucle sous certaines conditions via une activation thermique ou un effet tunnel quantique macroscopique. La jonction Josephson, un élément clé des dispositifs quantiques supraconducteurs, fournit une mise en œuvre simple de cet événement lors duquel le transfert d'une paire de Cooper entre les deux réservoirs supraconducteurs est visualisé comme le tunneling transversal du quantum de flux magnétique.
En réunissant ces concepts dans un dispositif d'interférence quantique supraconducteur (SQUID), il devient possible de générer un saut de phase où un quantum de flux pénètre ou quitte la boucle et la phase du supraconducteur s'enroule de 2π de manière déterministe. Cet événement est de nature dissipative lorsque le SQUID fonctionne dans le régime hystéretique et peut donc être détecté par des méthodes de calorimétrie. Dans cette thèse, nous démontrons la détection en temps réel d'un saut de phase qui se manifeste par l'augmentation abrupte et la relaxation subséquente de la température électronique du métal normal qui sert de lien faible du SQUID. Notre système est intégré dans un résonateur micro-onde. Les sauts de phase sont générés par des impulsions nanosecondes envoyées sur un ligne de flux 'on-chip', et l'excursion de température est lue via la variation de la puissance transmise par exploitant l'effet de proximité comme thermomètre secondaire.
En abordant l'observation d'un événement dissipatif élémentaire, cette thèse souligne le rôle de la dissipation omniprésente dans les dispositifs supraconducteurs et met en valeur l'utilisation potentielle des nano-calorimètres rapides dans le domaine des capteurs quantiques.

Outline

Superconductivity is a fascinating property of metals where the conduction electrons condensate into a common ground state and the entire system acts as a charged superfluid. The story of superconductivity began in the early 1900s with the technical advances on the liquefaction of helium and progressively matured into a vibrant branch of physics over the course of the 20th century.

One of the various counter-intuitive features that superconductors harbour is the quantization of the magnetic flux. When confined at the center of a superconducting loop, the magnetic flux which is a continuous quantity in the classical world, admits only the integer multiples of a universal constant ($\Phi_0 = h/2e \approx 2.068 \times 10^{-15}$ Wb) denoted as the magnetic flux quantum. This intriguing phenomenon stems from the condition that the wavefunction $\Psi = |\Psi|e^{j\phi}$ which represents the superconductor must be a single-valued function of position and therefore can only accumulate integer multiples (n) of $\phi = 2\pi$ upon a complete tour around the loop. Despite being confined at the center of the superconducting loop, under certain conditions, a magnetic flux quantum can tunnel in/out of the loop which corresponds to a momentary collapse and revival of the wavefunction where the phase winds by 2π. This event is shortly called as a phase slip.

Within the framework of Josephson junctions, another fascinating sprout of the superconductivity where two superconducting reservoirs are separated by a weak link, the transfer of Cooper pairs from one reservoir to the other provides an equivalent picture for Φ_0 tunneling as a Josephson vortex in the transverse axis of the current flow (Fig. 1a).

In this thesis, we deal with the real-time detection of a single phase slip in a Josephson junction by measuring its thermal signature with a fast calorimetry method. Our work builds upon the previous reports on the proximity thermometer [1–3], superconducting quantum interference device with an SNS Josephson junction [4] and the pertaining fast readout methods [5, 6]. Our main ingredients are

1. Superconducting quantum interference device (SQUID) which brings together the concepts of flux quantization and the Josephson effect. When engineered to operate in the hysteretic regime (strong screening), the SQUID becomes a reliable tool for generating phase slips in a deterministic way. When driven beyond a threshold bias, the so-called phase particle representing the system state falls into the next potential minimum and the difference in the internal energy is simply dissipated in the form of Joule heat (Fig. 1b, c).

2. SNS Josephson junction formed by two superconducting electrodes (S) and a normal metal (N) in the middle. The importance of this hybrid structure for our experiment cannot be stressed enough. It features Josephson effect and operates intrinsically in the overdamped regime. Therefore, when used in a SQUID, the SNS junction provides the suitable mode of operation for generating single phase slips rather than switching to the running state. Moreover, thanks to the poor thermal conduction of superconductors, the N island is thermally isolated on both ends and the heat transport occurs dominantly through phonons. Given the weak electron-phonon scattering rates at sub-K temperatures, we can therefore use N as a calorimeter which absorbs the heat generated by a phase slip.

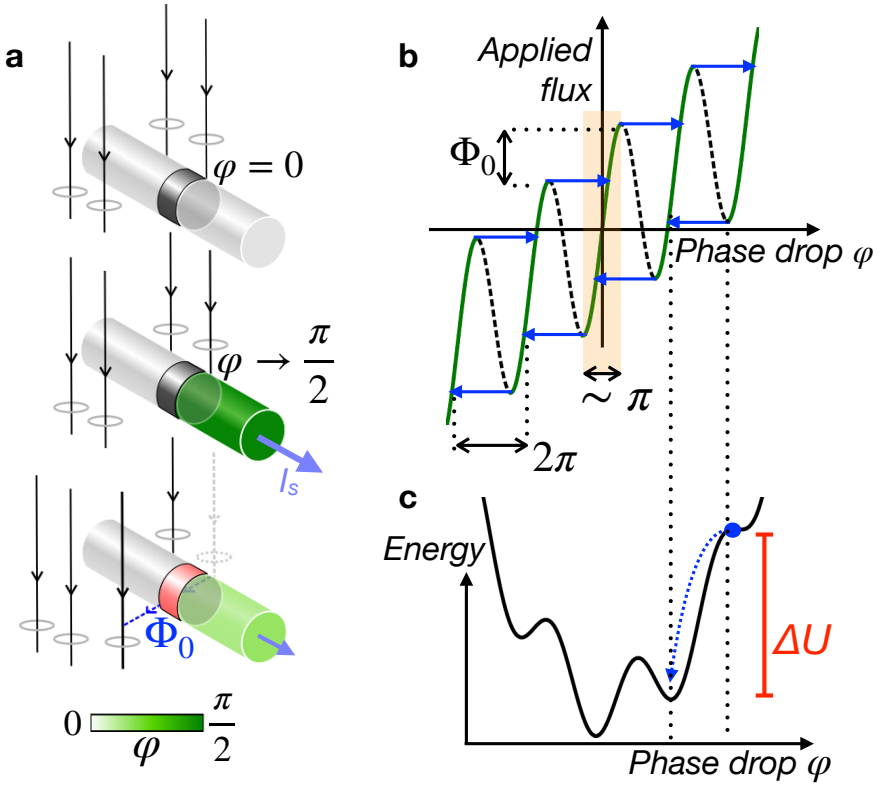

Figure 1: ***a.*** *Schematic description of the phase slip mechanism in a Josephson junction. A quantum of flux tunnels perpendicular to the Josephson junction, releasing heat.* ***b.*** *The applied flux vs. phase drop curve for a hysteretic SQUID. The applied flux versus the phase drop across the Josephson junction in a hysteretic SQUID. The phase slips are marked in blue arrows.* ***c.*** *The potential landscape of the system. The external flux tilts the potential in one direction an causes the so-called phase particle to stabilize in the neighboring local minimum. The difference in the internal energy (ΔU) is dissipated in the form of Joule heat.*

3. N'IS thermometer: As mentioned previously, the dissipation followed by a phase slip is of ohmic nature. Therefore, it is absorbed by the electron population of N. To probe the electronic temperature of the absorber, we add a third superconducting electrode separated from the island by an oxide layer. When probed at zero bias voltage, the tunneling conductance of the hybrid system made of a proximitized metal (N'), the isolating layer

(I) and the superconducting electrode (S) provides a sensitive secondary thermometer.
4. Fast readout scheme: probing the tunneling conductance of the $NI'S$ junction with conventional lock-in methods suffers from a reduced bandwidth ($\sim$ kHz) due to the parasitic capacitive couplings. To circumvent this issue, we embed our device in a resonant RLC circuit with a large bandwidth ($\sim$ 10 MHz), probe the system at resonance ($\sim$ 575 MHz) and read the temperature of N via changes on the S_{21} parameter.
5. Rapid flux line Macroscopic coils used to generate phase slips in the SQUID proves slow. Therefore, we converge to an on-chip coupling solution where a monolithically fabricated flux line carries the fast flux pulses. We will see that the mutual coupling between the rapid flux line and the SQUID, therefore the device geometry and the material choice have to be engineered carefully.
The organisation of this manuscript is as the following: we begin by discussing the theoretical background of the building blocks of this project in Chapter 1. The superconductivity and the Josephson effect are explained with a somewhat historical perspective. Next, we delve into the fundamental relations of the Josephson effect, discuss the resistively shunted capacitive junction (RSCJ) model and elaborate on the SNS type Josephson junctions. We detail the principles of the coherent transport in SNS junctions together with the different transport regimes at several limit conditions. Then, we make our way to the phase slips in a SQUID by discussing the Meissner effect, the flux quantization in a superconducting ring and the fundamentals of RF-SQUID in the given order.
In Chapter 2, we quickly review the fundamental concepts of thermodynamics at the basic level and the primary/secondary thermometer types. We elaborate on the working principles of the superconducting hybrid junctions including NIS, SNS and N'IS as thermometers. The following two sections discuss the bolometers and the calorimeters and details the thermal model of our system.
Chapter 3 opens with a discussion on resonance, driven damped systems and the quality factor. We move on to the discussion of microwave concept of S parameters, the readout schemes and I-Q mixing. Next, we discuss the design of our resonator which is realized as a stand-alone superconducting chip. We compare the lumped element values and the resonance with the previous reports from the literature. Finally, we explain and discuss the results of our experiment on capturing in real time the switching between dissipative and coherent states in an SNS junction, which served as the first field test for our fast proximity thermometer. In Chapter 4, the experiment on the real-time detection of single phase slips is discussed in detail. We begin by elucidating the role of the normal metal and the impact of the drive signal on the thermal model. Next, the conditions for obtaining a SQUID device in the hysteretic regime are explained. In what follows, we adopt a chronological narrative to highlight the evolution of our sample design and the engineering challenges on achieving a sufficient mutual inductive coupling between the flux line and the SQUID. We discuss the measurement protocol of the real time detection and finally discuss the results.

During my time at the Néel Institute for my PhD, I actively participated in two projects that resulted in successful collaborations and the publication of the articles:

- Calorimetry of a phase slip in a Josephson junction.
Gümüş E, Majidi D, Nikolić D, Raif P, Karimi B, Peltonen JT, Scheer E, Pekola JP, Courtois H, Belzig W, Winkelmann CB.
Nature Physics. 2023 Jan 5:1-5.
Following the initial discussions on the subject with C. Winkelmann, I designed the device and optimized it on several iterations. The samples were fabricated together with D. Majidi and P. Raif. I had the main responsibility on the experiments and the data analysis. I wrote the major part of supplementary information and contributed to the writing of the main paper.

- High-Impedance Surfaces for Above-IC Integration of Cooled Bolometer Arrays at the 350-µm Wavelength.
Dussopt L, Aliane A, Kaya H, Goudon V, Rodriguez L, Delisle C, Tollet T, Revéret V, Poglitsch A, Gümüs E, Winkelmann CB., Hamdi M
Journal of Low Temperature Physics. 2022 Aug 10:1-6.
I was involved in the characterization of the samples over several iterations and the data interpretation.

Chapter 1

Theoretical Background

1.1 Josephson Effect

1.1.1 Superconductivity

Superconductivity refers to a particular phase of metals where direct consequences of quantum mechanics become visible at macroscopic scale and electrodynamic/thermal properties differ drastically from the normal metallic phase. Below a critical temperature (T_c), conduction of electrons becomes resistance-free. Magnetic field is expelled from the bulk and a gap opens in the excitation spectrum of quasiparticles. Specific heat presents a discontinuity at $T = T_c$ and is dominated by an exponential dependence on temperature for $T < T_c$. The family of elements, compounds and alloys featuring such a transition are simply called superconductors.

The study of superconductivity was initiated by the discovery of the perfect DC conductance by Heike Kamerlingh Onnes in 1911 upon cooling mercury (Hg) below 4.2 K [7]. Later on, Meissner and Ochsenfeld [8] observed the expulsion of the magnetic field from the superconducting bulk for the first time in 1933. On the theoretical aspect, London brothers proposed the first model [9] in 1935, shortly after the discovery of Meissner-Ochsenfeld effect. London equations brought a successful explanation on the experimental observations however the model was unable to elucidate the origin of superconductivity. It was not before 1950's that a full microscopic picture was developed.

Within the framework of Ginzburg - Landau theory [10] proposed in 1950, a complex order parameter, Ψ, is associated with the superconducting state such that

$$\Psi(r) = \begin{cases} 0 & T > T_c \\ |\Psi(r)|e^{j\phi(r)} & T < T_c \end{cases}$$

Bardeen, Cooper, and Schrieffer (BCS) [11] completed the microscopic picture with three key ingredients (i) attractive electron - electron interaction which leads to the formation of electron (Cooper) pairs [12] (ii) the instability of Fermi sea against the formation of Cooper pairs, hence a new ground state (iii) a many-body wavefunction representing

the coherent ground state of the superconductor. Later on, Gor'kov [13, 14] linked the two models by demonstrating that GL order parameter Ψ corresponds to the BCS wavefunction such that the density of Cooper pairs, ρ, in a superconductor is related to the order parameter amplitude as $\rho = |\Psi|^2$.

1.1.2 Fundamental relations

Next, we focus on the case where two superconductors are brought in close proximity. In the late 1950's, tunneling of single electrons through an insulating barrier was already demonstrated in semiconductors [15]. Later on, experiments done by Giaever showed that the same phenomenon was apparent in superconductor-insulator-superconductor structures which eventually led to the demonstration of the existence of a gap in SC density of states [16]. In his experiments, Giaever had also observed a finite DC current at zero voltage bias which he falsely attributed to the pinholes in the oxide layer. On the theoretical aspect, the possibility of a Cooper pair tunneling through an insulating barrier, necessary mechanism for tunneling supercurrent, was studied by Pippard [17]. At that time, common understanding was that such event would require simultaneous tunneling of two incoherent electrons which would make the observation unlikely.
In 1962, Josephson predicted that Cooper pair tunneling was a coherent event and the resultant supercurrent was in the same order of magnitude as the quasiparticle current [18]. He further showed that the tunneling supercurrent was given by the equation:

$$I_s(\varphi) = I_c \sin\varphi \tag{1.1}$$

where I_c is the the critical current and φ corresponds to the gauge-invariant phase difference across the barrier. A finite voltage drop (V) across the junction leads to time evolution of φ as

$$\frac{d\varphi}{dt} = \frac{2e}{\hbar}V \tag{1.2}$$

hence yielding an AC current

$$I_s(\varphi) = I_c \sin\left(\varphi_0 + \frac{2e}{\hbar}Vt\right) \tag{1.3}$$

with $\omega = \frac{2e}{\hbar}V$, Josephson junction acts as a voltage-controlled oscillator. Eq. (1.1) and Eq. (1.2) form the essence of Josephson's findings and are called DC and AC Josephson effect respectively. Josephson's prediction was followed by the experimental proof in 1963 [19] and Josephson junction became the generic name for the systems of weakly coupled superconductors.
Josephson's theoretical work considered an SIS junction. Obviously, the choice was inspired by the tunneling experiments of the time. With the improvements in fabrication

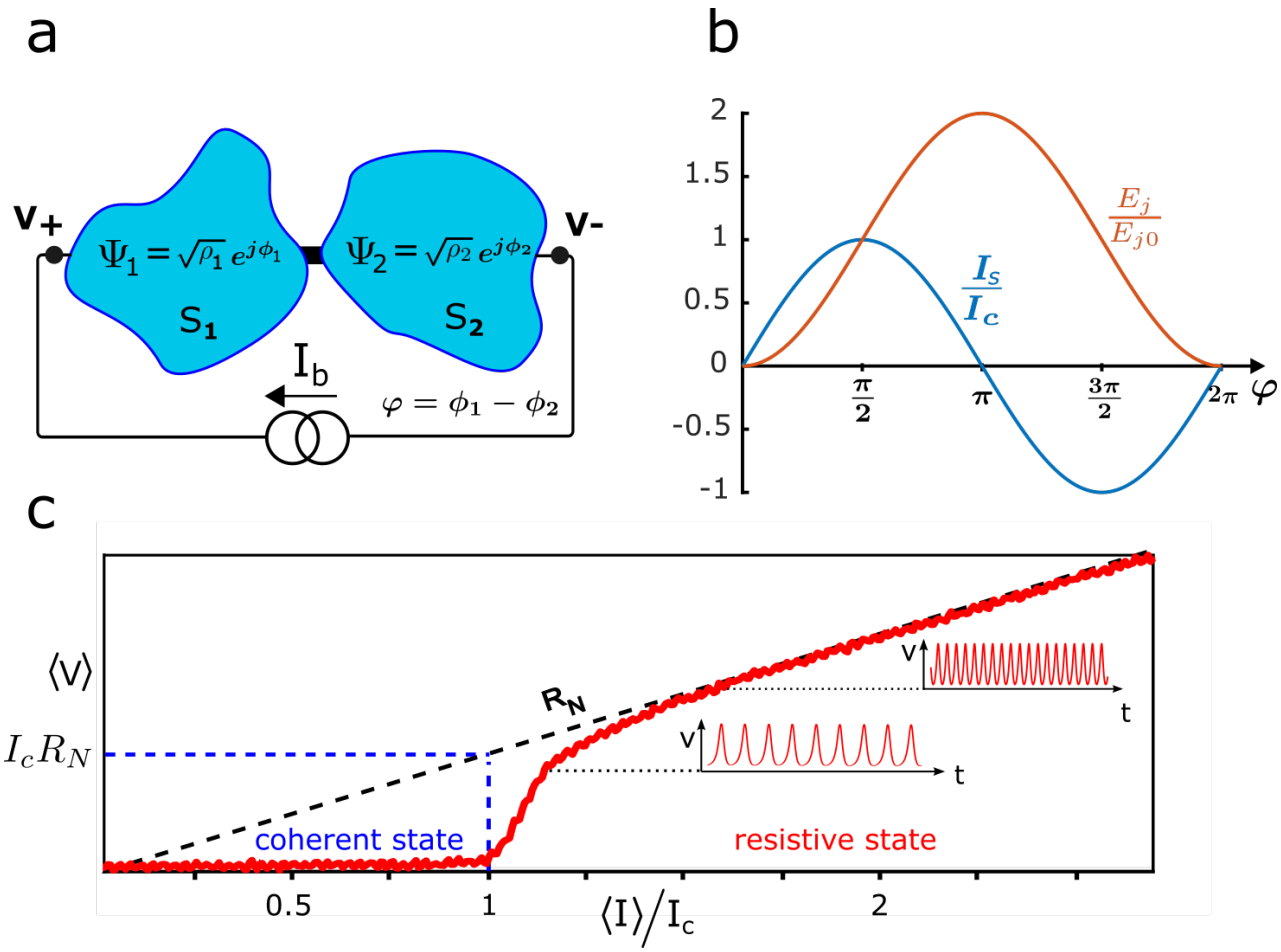

Figure 1.1: ***a.*** *Schematic representation of a current-biased Josephson junction. Superconductors $S_{1,2}$ (blue) are represented by the wavefunctions $\Psi_{1,2}$. In a typical measurement setup, bias current I_b is swept and the voltage across $(V_+ - V_-)$ is measured.* ***b.*** *supercurrent (I_s) in units of critical current (I_c) and the stored energy (E_j) normalized to Josephson energy E_{j0} plotted as a function the Josephson phase (φ)* ***c.*** *V-I measurement of a Josephson junction (red). Junction is in coherent state for $I_b \leq I_c$. Time evolution of V at resistive state is shown in inset. Oscillation frequency increases with bias current I.*

methods and ever-growing interest in the field since then, a plethora of device configurations were shown to display Josephson effect [20–22]. To mention a few, microbridges where the weak link is formed by a constriction of the same superconducting material were investigated as early as 1964 [23]. Initial works on Pb - Cu - Pb sandwiches [24, 25] set the stage for superconductor (S) - normal (N) - superconductor (S) junctions by showing that a coherent current over N was possible thanks to the proximity effect, a phenomenon predicted by de Gennes [26]. Later on, ferromagnet (F) interlayers were introduced which led to the observation of π-state in SFS junctions [27, 28]. Hybrid structures such as graphene [29–31], and topological insulator (TI) [32, 33] based Josephson junctions have been also studied. Definitive observation of Majorana bound states in S-TI combined structures is an active field of research [34–37].

1.1.3 Coherent vs Resistive States

Experimentally, DC Josephson effect can be observed by imposing an external bias current (I_b) through the junction and measuring the voltage across (Fig. 1.1a). The coherent nature of the Cooper pair tunnelling leads to a current flow with zero-voltage drop across the junction between $-I_c \leq I_b \leq I_c$. In return, the applied current sets the phase bias between $-\pi/2 \leq \varphi \leq \pi/2$ in a steady-state manner. We name this regime the coherent state.

Josephson Energy. Although the junction is in coherent state, one sees that time evolution of the phase $0 \rightarrow \pi/2$ requires a finite voltage as Eq. (1.2) shows. This seemingly paradoxical situation is resolved when we consider the energy stored in a Josephson junction. Setting up a supercurrent through Josephson junction requires energy. In this framework, the temporary emergence of the finite voltage provides the power (I_bV) delivered to the system to accelerate the Cooper pairs. Considering a time window t_0 for ramping up the I_b, we can calculate the work done on Josephson junction by the external source as

$$E_j = \int_0^{t_0} I_s V dt \tag{1.4}$$

Inserting Eq. (1.1) and Eq. (1.2) in Eq. (1.4)

$$E_j = \int_0^{\varphi} I_c \sin\tilde{\varphi} \frac{\hbar}{2e} d\tilde{\varphi} \tag{1.5}$$

and evaluating the integral, we reach

$$\boxed{E_j = E_{j0}(1 - \cos\varphi), \quad E_{j0} = \frac{\hbar I_c}{2e}} \tag{1.6}$$

where E_{j0} is called the Josephson energy. Fig. 1.1b shows the phase dependence of I_c and the energy stored in a Josephson junction.

Resistive state. What happens when we drive the junction at $I_b > I_c$? As the supercurrent obeys the condition $-I_c \leq I_s \leq I_c$, the excess current needs to be ensured

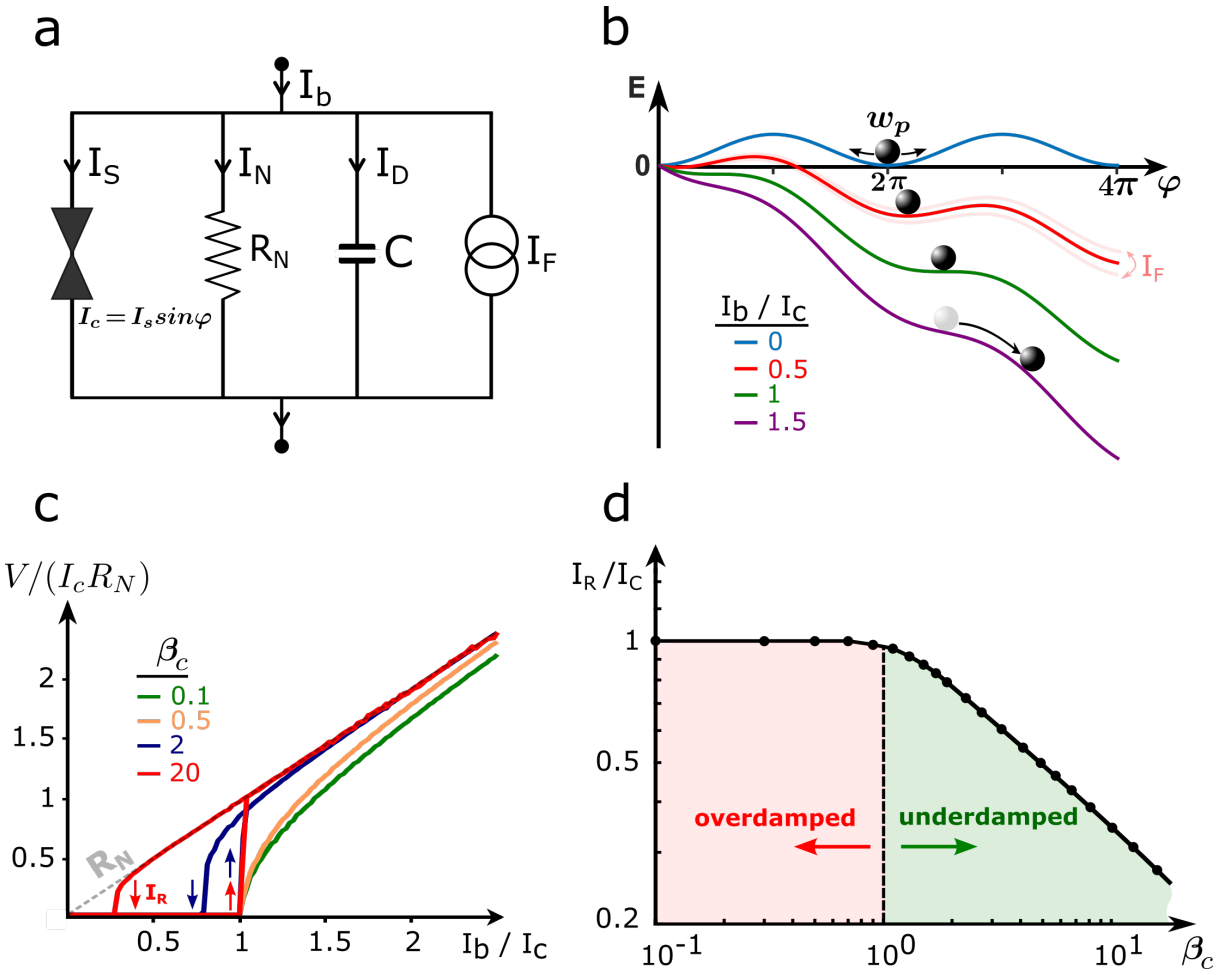

Figure 1.2: ***a.*** *Resistively and capacitively shunted junction model of a Josephson junction* ***b.*** *Motion of the so-called phase particle in a tilted washboard potential. The system oscillates at* $\omega = \omega_p$ *at* $I_b = 0$*. Increasing* I_b *tilts the potential downwards. The phase particle rolls downhill for* $I_b \geq I_c$ ***c.*** *Calculated voltage (V) for different* β_c *values, in units of* $I_c R_N$ *as a function of* I_b *normalized to* I_c*.* R_N *is the normal-state resistance.* β_c *is the Stewart-McCumber parameter. [38, 39]* $I_{c,b}$ *is the critical (bias) current.* ***d.*** *Retrapping current* I_R *in units of* I_c *plotted versus Stewart-McCumber parameter. The Josephson junction is overdamped (underdamped) for* $\beta_c < 1$ *(*$\beta_c > 1$*).*

by other transport mechanisms. For $T > 0$, superconducting leads have non-vanishing quasiparticle density due to the thermal break up. Moreover, accelerating the superfluid transfers energy to the Cooper pairs such that they break up when the gap energy 2Δ is overcome. Hence, a resistive transport channel (R_N) opens up for $I_b > I_c$, resulting in a tunneling current of quasiparticles (I_N) and a finite voltage ($V = I_N R_N$) across the junction (Fig. 1.1c). Consequently, this regime is called the resistive or normal state.

Displacement current. In the presence of finite voltage (V), the phase evolves in time according to Eq. (1.49) and generates an oscillating supercurrent. The fact that the total current is fixed by I_b causes I_N to oscillate as well. In return, oscillating I_N yields $\frac{dV}{dt} \neq 0$. For the case $\frac{dV}{dt} \neq 0$, the capacitive aspect of the Josephson junction becomes important. Thus, we can talk about a third transport mechanism which carries the displacement current, given as $I_D = C\frac{dV}{dt}$.

1.1.4 Resistively Shunted Capacitive Junction Model

So far, we elaborated on different current-carrying mechanisms in a Josephson junction. The interplay between these channels will lead to a rich electrodynamic behaviour which we can encapsulate in a lumped circuit model called **resistively and capacitively shunted junction model** (RCSJ) (Fig. 1.2a). Including a noise term, I_F, we can write the total current via Kirchoff's rule as

$$I_b = I_S + I_N + I_D + I_F \tag{1.7}$$

inserting Eq. (1.1) in Eq. (1.7), we obtain

$$I_b = I_c \sin\varphi + \frac{V}{R_N} + C\frac{dV}{dt} + I_F \tag{1.8}$$

Let us rewrite Eq. (1.8) in terms of φ

$$I_b = I_c \sin\varphi + \frac{1}{R_N}\frac{\Phi_0}{2\pi}\frac{d\varphi}{dt} + C\frac{\Phi_0}{2\phi}\frac{d\varphi^2}{dt^2} + I_F \tag{1.9}$$

Hence, we reach the equation of motion for the phase. Eq. (1.9) can be reformulated as [40]

$$\left(\frac{\hbar}{2e}\right)^2 C\frac{d^2\varphi}{dt^2} + \left(\frac{\hbar}{2e}\right)^2 \frac{1}{R_N}\frac{d\varphi}{dt} + \frac{d}{d\varphi}\left(E_{j0}\left[1 - \cos\varphi - \frac{I_b}{I_c}\varphi + \frac{I_F}{I_c}\varphi\right]\right) = 0 \tag{1.10}$$

to make an analogy with the motion of a particle having a mass, m, in a viscous liquid with damping η, in a potential U:

$$m\frac{dx^2}{dt^2} + \eta\frac{dx}{dt} + \nabla U = 0 \tag{1.11}$$

The motion of the so-called phase particle in potential $U = E_{j0}[1 - \cos\varphi - \frac{I_b}{I_c}\varphi + \frac{I_F}{I_c}\varphi]$ is shown in Fig. 1.2b. For $I_b \leq I_c$, the particle is trapped in one of the valleys and oscillates around the potential minimum at frequency

$$\omega = \omega_p\big(1 - \frac{I_b^2}{I_c^2}\big)^{0.25} \tag{1.12}$$

where ω_p is the plasma frequency. As the average phase is constant ($\langle\dot{\varphi}\rangle = 0$), the $I - \varphi$ relation is static, agreeing with the coherent state. Increasing I_b tilts the potential landscape such that for $I_b > I_c$ the potential barrier is removed and the particle slides continuously, leading to a finite voltage across the junction.

Underdamped vs. Overdamped. Starting from the resistive state ($I_b > I_c$) and sweeping I_b in the negative direction, the phase particle is retrapped at $I_b \leq I_c$. The current value at which the transition occurs is called the retrapping current, I_R, which depends on the junction parameters. I_R defines two distinct regimes which we can understand with the help of the analogy we previously established. The junction with large capacitance (big mass) and high resistance (low damping) continues rolling down the potential despite the existing local minima thanks to its sufficient kinetic energy. For this reason, the potential landscape has to be tilted upwards further for retrapping ($I_R < I_c$). Junctions featuring such behaviour are called "underdamped". Conversely, having a small capacitance (small mass) and low resistance (high damping), phase particle is retrapped as soon as $I_b = I_c$, hence yielding $I_R = I_c$ (Fig. 1.2c,d). The junctions in this regime are "overdamped".

Characteristic frequencies. RCSJ model allows us to think of Josephson junction as a parallel RLC resonator where L represents the Josephson inductance given as $L_j = \frac{\phi_0}{2\pi I_c}$. Hence, the plasma frequency $\big(w_p = \frac{1}{\sqrt{L_j C}}\big)$ mentioned above corresponds to the resonant frequency when $I_b = 0$. We can define two more characteristic frequencies (1) the decay time (τ_c) of supercurrent I_S over the normal channel (R_N) yields the characteristic frequency $w_c = \frac{1}{\tau_c} = \frac{R_N}{L_J}$ (2) the discharge of the junction capacitance over R_N gives $\omega_{RC} = \frac{1}{\tau_{RC}} = \frac{1}{R_N C}$. It is now straightforward to understand the under/over damped regimes in terms of the resonator's quality factor:

$$Q = \sqrt{\beta_c} = \frac{\omega_p}{\omega_{RC}} = \frac{\omega_c}{\omega_p} \tag{1.13}$$

where β_c is the Stewart [38]-McCumber [39] parameter. High Q ($\beta_c > 1$) and low Q ($\beta_c < 1$) correspond to underdamped and overdamped regimes respectively.

1.1.5 SNS Junction

Proximity Effect

What happens when we bring a superconductor where a macroscopic wavefunction represents the highly correlated electrons in contact with a normal metal where these correlations cannot exist naturally ? It turns out that pair correlations leak into N and

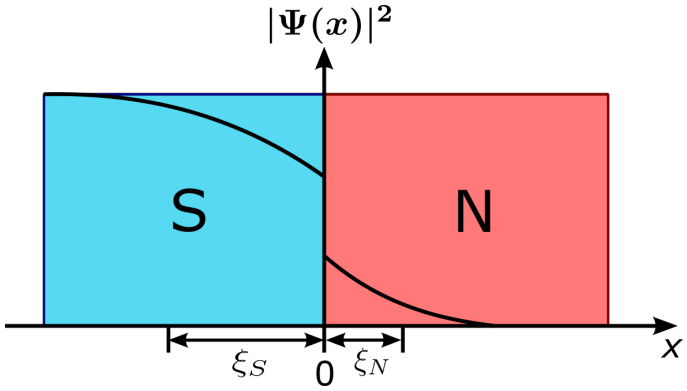

Figure 1.3: ***Proximity effect.*** *Spatial dependence of the density of pairs* $|\Psi(x)|^2$ *near the interface between a superconductor* $(x < 0)$ *and a normal metal* $(x > 0)$*. (adapted from [41])*

travel a finite distance before decohering in the absence of attractive electron-electron interactions. This process, known as the proximity effect, diminishes the density of pair correlations near the boundary in S and leads to an evanescent tail on the N side (Fig. 1.3). The spectral properties of normal metal undergoes certain modifications with the proximity effect. A minigap opens in quasiparticle density of state [42, 43], energy exchange between electrons and phonons weakens [44], and specific heat deviates from the normal case and becomes phase tunable [45].

Bogoliubov-de Gennes formalism [46] provides the theoretical framework of the proximity effect. In this method, electron-like and hole-like excitations inside the superconducting bulk are represented by a two-component wavefunction $\Psi = (\Psi_e, \Psi_h)$ which is the solution of a coupled set of Schrödinger equations:

$$\begin{pmatrix} \hat{H} & \Delta e^{j\phi} \\ \Delta e^{-j\phi} & -\hat{H}^* \end{pmatrix} \begin{pmatrix} \Psi_e \\ \Psi_h \end{pmatrix} = E \begin{pmatrix} \Psi_e \\ \Psi_h \end{pmatrix} \tag{1.14}$$

At low temperatures, only the excitation near Fermi energy are relevant ($E, \Delta \ll E_F$). Therefore, BdG equation can be simplified to a system of first-order differential equations with a plane wave solution $\Psi_{e,h}(x) \propto \tilde{\Psi}_{e,h}(x) e^{jk_F x}$

$$\begin{pmatrix} -j\hbar v_F \frac{d}{dx} & \Delta e^{j\phi} \\ \Delta e^{-j\phi} & j\hbar v_F \frac{d}{dx} \end{pmatrix} \begin{pmatrix} \tilde{\Psi}_e \\ \tilde{\Psi}_h \end{pmatrix} = E \begin{pmatrix} \tilde{\Psi}_e \\ \tilde{\Psi}_h \end{pmatrix} \tag{1.15}$$

which is known as the Andreev approximation [47, 48] (Fig. 1.4a). In the following section, we will provide a qualitative description of the Andreev reflection.

Andreev Reflection

Andreev reflection is the microscopic mechanism which allows the transfer of quasiparticles with excitation energy $\epsilon < \Delta$ through NS interface [51]. In this counter-intuitive process, an electron (e_1) with a momentum $\hbar k_{e1} = \hbar k_F + \epsilon / v_F$ and spin $\uparrow$ hitting the boundary from N side reflects as a hole (h_1) with $\hbar k_h = \hbar k_F - \epsilon / v_F$ and spin $\uparrow$. The process can

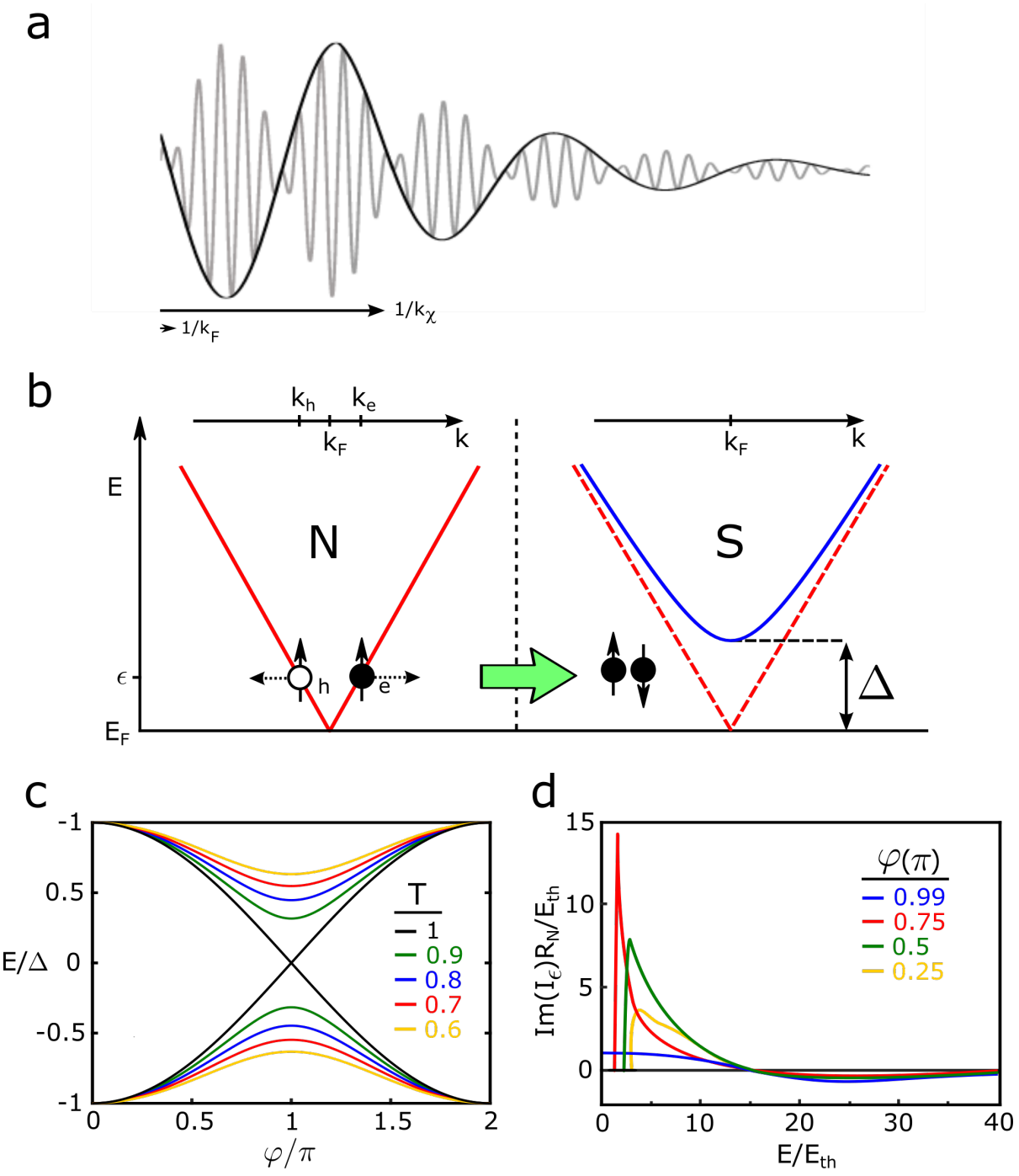

Figure 1.4: ***a.*** *Andreev approximation: for $E << E_F$, a slow varying envelope wavefunction $\tilde{\Psi}_{e,h}(x)$ (black) which ignores the fast oscillations at k_F (gray) is used (adapted from [49])* ***b.*** *Andreev reflection: an electron (e) with momentum $\hbar k_e$ and spin $\uparrow$ impinges on NS boundary and reflects as a hole with momentum $\hbar k_h$ and spin $\uparrow$. Net charge of 2e is transferred to S (adapted from [48])* ***c.*** *Spectrum of Andreev bound states as a function of Josephson phase φ at different contact transparency $T \in [0, 1]$* ***d.*** *The product of spectral supercurrent $Im(I_\epsilon)$ and R_N as a function of energy in units of E_{Th} for different values of Josephson phase φ. R_N is the normal state resistance, E_{Th} is the Thouless energy (adapted from [50])*

also be pictured as the pairing of e_1 with e_2 with momentum $\hbar e_2 = -k_F + \epsilon/v_F$ and spin $\downarrow$. Therefore, a net charge of 2e is transferred to S as a Cooper pair. Note that h_1 has a negative group velocity $\left(v_g = \frac{dE}{dk}\right)$ although $k_{h_1} \approx k_{e1}$. Therefore, Andreev reflection is quasi perfect retro-reflection .

By solving Eq. (1.15) in N ($x > 0$, $\Delta = 0$) it can be shown that the reflected hole gains a phase shift with respect to impinging electron as :

$$\varphi_h = \varphi_e + \varphi_S - \arccos(\epsilon/\Delta) \tag{1.16}$$

which depends both on the excitation energy ϵ and the phase of the superconducting condensate, φ_S. If we now make an SNS sandwich, then Andreev reflections take place at both NS interfaces. The Andreev pairs inside N carry the phase information of both interfaces and lead to the formation of Andreev bound states [52, 53] below Δ whenever round-trip reflection accumulates a phase shift of $2\pi n$. These discrete sub-gap states act as phase dependant channels carrying the coherent current through SNS junction (Fig. 1.4c).

Diffusive transport. Transport mechanism with discrete sub-gap states applies particularly to the ballistic regime where the weak link length is shorter than the elastic mean free path ($L < l_e$) [52]. At a broader scale, the transport properties of SNS systems, hence the possible regimes, are determined by a competition among several characteristic lengths shown in Fig. 1.5a. For the case $L > l_e$, a quasiparticle pair entering N with excitation energy $\pm\epsilon$ is subject to multiple elastic collisions and dephases in time by $e^{-i2\epsilon t/\hbar}$ and covers a distance $L_\epsilon = \sqrt{\hbar D/\epsilon}$ before completely decohering. $D = \frac{1}{3} v_F l_e$ is the diffusion constant [54]. Therefore, the transport in this regime is called "diffusive". In the diffusive regime, quasiparticle trajectories obtain a statistical distribution of the net traveled distance due to a high concentration of scatterers which leads to the broadening of Andreev bound states. As a consequence, the spectral composition of the super current becomes a continuous function of energy unlike the ballistic case (Fig. 1.4d). In the low energy limit ($\epsilon \to 0$), L_ϵ is limited by (L_φ) where L_φ is the characteristic distance related to the dephasing caused by inelastic reflections and spin-flip scatterings.

Quasiclassical theory of diffusive transport. BdG formalism is frequently employed for the theoretical treatment of various ballistic systems [56–58]. However, it proves impractical for diffusive regime as the disorder concentration makes the scattering matrix intractable. A more suitable approach is provided by Green Functions (GF) in quasiclassical limit [59, 60]. Within the context of superconductivity, GFs turn into two-point correlators which carry the information on coherence. They are the solution of Eilenberger equation [61], analogous of Boltzmann transport equation [48] endowed with coherence. In the dirty limit ($L \gg l_e$), Eilenberger equation is further simplified by disregarding the anisotropic term of GF (angular averaging). Hence, we reach Usadel equation which is the coherent counterpart of the drift-diffusion equation [62]. In 1-D, it

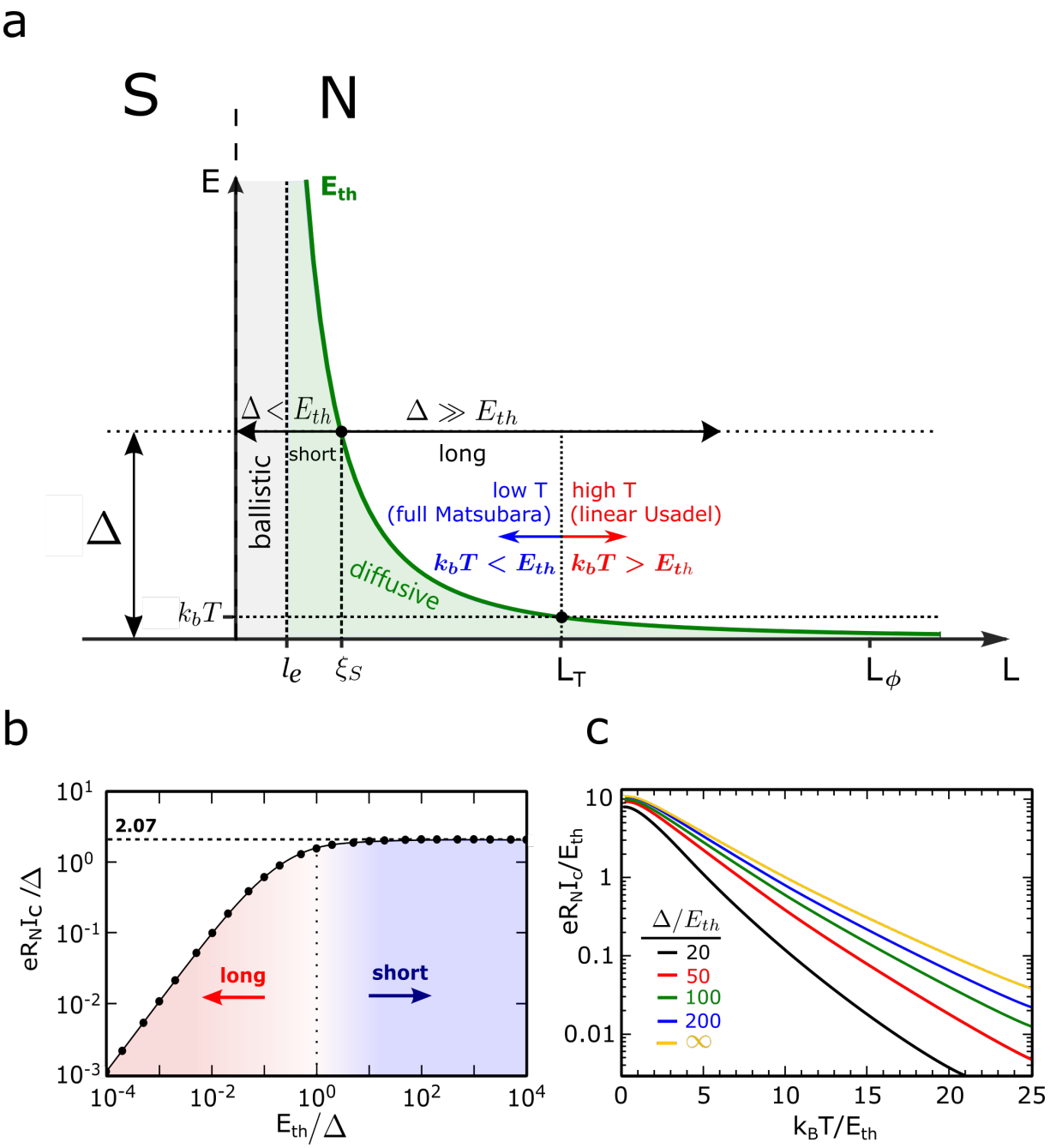

Figure 1.5: **a.** *Diagram showing the different transport regimes of a Josephson junction. Transport is ballistic (diffusive) when $L < l_e$ ($L > l_e$). Diffusive regime is divided into short ($\Delta < E_{Th}$) and long ($\Delta \gg E_{Th}$) limits. At low T ($k_BT < E_{Th}$), all Matsubara frequencies contribute to the supercurrent. Therefore, full Usadel equation has to be solved. For high T ($k_BT > E_{Th}$), Usadel equation can be linearized. E_{Th} is the Thouless energy* **b.** *Calculated dependence of eR_NI_c product in units of Δ as a function of the ratio E_{Th}/D. I_c is the Josephson critical current, R_N the normal-state resistance. The Josephson junction is in the short (long) regime for $E_{Th}/\Delta > 1$ ($E_{Th}/\Delta < 1$) The horizontal dashed line marks the limit given by Kulik-Omel'yanchuk formula [52] (adapted from [55])* **c.** *Calculated temperature dependence of the eR_NI_c product. The different curves correspond to various values of the ratio Δ/E_{Th} in the long-juction regime. The curve for $\Delta/E_{Th} \to \infty$ is universal in the sense that it does not depend on Δ. (taken from [55])*

is written as:

$$\frac{\hbar D}{2}\frac{\partial^2\theta}{\partial x^2}+iE\sin\theta-\underbrace{\left(\frac{\hbar}{\tau_{sf}}+\frac{\hbar D}{2}\left(\frac{\partial\varphi}{\partial x}+\frac{2e}{\hbar}A(x)\right)^2\right)\cos\theta\sin\theta}_{\substack{\text{pair breaking}\\ \tau_{sf}\text{: spin-flip scattering time constant}\\ \text{A(x): magnetic vector potential}}}+\underbrace{\Delta(x)\cos\theta}_{\text{pairing interaction}}=0 \quad (1.17)$$

$$\frac{\partial}{\partial x}\left[\left(\frac{\partial\varphi}{\partial x}+\frac{2e}{\hbar}A(x)\right)\sin^2\theta\right]=0 \quad (1.18)$$

where Eq. (1.17) describes the position dependence of the complex quantity called the pairing angle $\theta(x,E)$ and Eq. (1.18) represents the current conservation [63]. The pairing angle, θ, is the product of angular paramaterization of GFs. It encapsulates the properties of a proximity system at equilibrium. For instance, the spectral current density, j_s, can be written as

$$j_s(x,E,\varphi)=Im\left[-\frac{\partial\varphi}{\partial x}\sinh^2\theta(x,E)\right] \quad (1.19)$$

Then, the supercurrent at equilibrium is given by the integral

$$I_S=\frac{e}{2}n_0D\int_{-\infty}^{+\infty}dE(1-2f(E))Im[-\sinh^2\theta(x,E)] \quad (1.20)$$

which is basically the spectral current density weighted by the distribution function, f(E).

Short vs. long junctions. A particularly important energy scale related to the quasiparticle time of flight inside N is called Thouless energy [64]:

$$E_{Th}=\frac{\hbar D}{L^2} \quad (1.21)$$

The comparison between E_{Th} and the superconducting energy gap Δ divides the junctions in the diffusive regime into two categories (Fig. 1.5b):

1. Short-junction limit ($\Delta < E_{Th}$): The critical current (I_c) is dictated by the superconducting energy gap Δ. At T=0, it is given as [52]

$$I_c(T=0)=1.32\frac{\pi}{2}\frac{1}{eR_N}\Delta_{T=0} \quad (1.22)$$

and the current-phase relation peaks at $\varphi\approx 1.25\frac{\pi}{2}$.

2. Long-junction limit ($\Delta \gg E_{Th}$): The Thouless energy takes over Δ and becomes the relevant energy scale as the high energy quasiparticles ($E \gg E_{Th}$) dephase at a distance $L_\epsilon < L$. At T=0, I_C is given as [55]

$$I_c(T=0)=10.82\frac{1}{eR_N}E_{Th} \quad (1.23)$$

(Fig. 1.5c) and the $max(I_S)$ occurs at $\varphi\approx 1.27\frac{\pi}{2}$.

Low temperature vs. high temperature limit. In thermal equilibrium at $T \neq 0$, the supercurrent integral can be reformulated as a sum over fermionic Matsubara frequencies $\omega_n = (2n+1)\pi k_B T$ [65–67].

1. High temperature limit ($k_B T \gg E_{Th}$): The pair amplitude, $F = \sin(\theta_n)$, inside N is weakened (Fig. 1.6a). Hence, two S reservoirs can be considered as decoupled which allows the linearization of the Usadel equation. In this regime, the analytical expression of I_c is given as [55]

$$eR_N I_c(T) = 64\pi k_b T \sum_{n=0}^{\infty} \frac{L}{L_{\omega_n}} \frac{\Delta^2 e^{-L/L_{\omega_n}}}{\left(\omega_n + \Omega_n + \sqrt{2(\Omega_n^2 + \omega_n \Omega_n)}\right)^2} \tag{1.24}$$

where $\Omega_n = \sqrt{\Delta^2 + \omega_n^2}$ and $L_{\omega_n} = \sqrt{\hbar D / 2\omega_n}$. The major contribution to I_c comes from ω_0. In the long junction limit ($\Delta \gg E_{Th}$), I_c is simplified to

$$eR_N I_c(T) = \frac{32}{3+2\sqrt{2}} E_{Th} \left(\frac{2\pi k_B T}{E_{Th}}\right)^{1.5} e^{-\sqrt{\frac{2\pi k_B T}{E_{Th}}}} \tag{1.25}$$

2. Low temperature limit ($k_B T \ll E_{Th}$): Contribution of higher Matsubara frequencies to the critical current is not negligible (Fig. 1.6b). Therefore, the full Usadel equation needs to be solved numerically. In the long junction limit ($\Delta \gg E_{Th}$), an empirical expression which fits well the Usadel solution is given as [68]

$$\frac{eR_N I_c(T)}{E_{Th}} = b(1 - 1.3e^{-\frac{bE_{Th}}{3.2k_B T}}) \tag{1.26}$$

where $b = \left(\frac{eR_N I_c}{E_{Th}}\right)_{T=0}$.

Minigap. Proximity effect induces a gap in the density of states (DoS) of N (Fig. 1.7a) which is given by $n(x,E) = n_0 Re[\cos\theta(x,E)]$ where n_0 is the normal DoS, within the quasiclassical GF formalism. The phenomenon is called the minigap. It has been the subject of both theoretical [69–71], and experimental [42, 72, 73] studies over the past years. The minigap is dependent on the junction phase (φ) and disappears completely at $\varphi = \pi$. (Fig. 1.7b) Its magnitude (Δ_g) depends on [74]:

1. Transparency of the SN contact: characterised by the ratio $r = G_N/G_B$ where G_N is the normal metal conductance and G_B is the barrier conductance (Fig. 1.7c). G_B can be expressed as $G_B = NG_0\tau$ which is basically the conductance quantum (G_0) multiplied by the number of channels (N) and the transmission coefficient $\tau \in [0,1]$.

2. Concentration of magnetic impurities: given by the spin-flip scattering rate Γ_{sf} which represents the main pair breaking mechanism (Fig. 1.7d).

Considering the ideal case ($r = 0$, $\Gamma_{sf} = 0$), it was shown by Ref. [74] that $\Delta_g \sim 3.1 E_{Th}$ in the long junction limit ($\Delta \gg E_{Th}$).

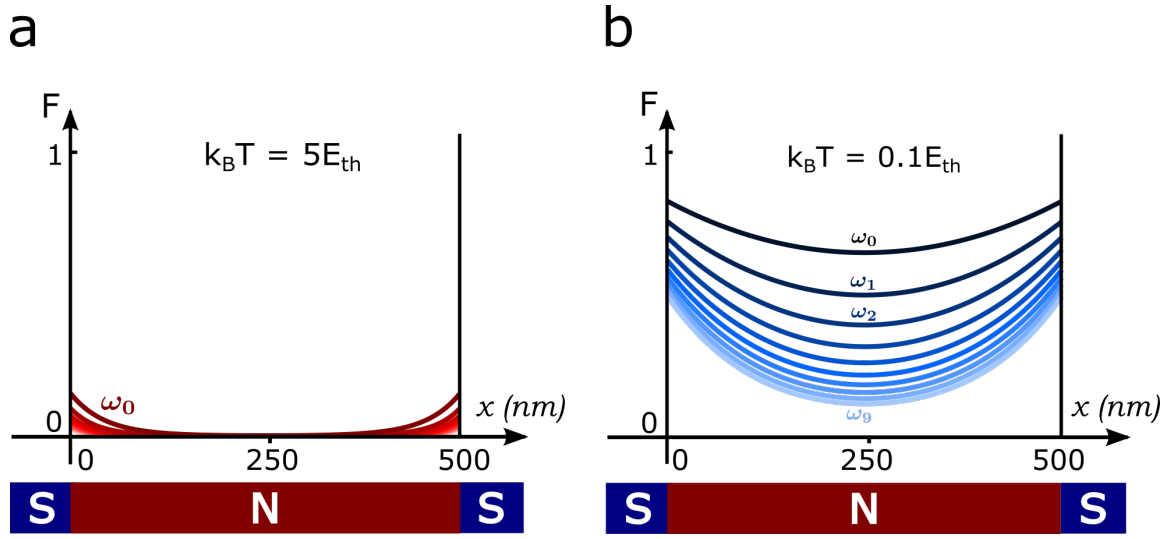

Figure 1.6: Spatial dependence of the pair amplitude $\sin\theta_n$ *inside N, calculated at* ***a.*** $k_bT = 5E_{Th}$ ***b.*** $k_bT = 0.1E_{Th}$ *for the first ten Matsubara frequencies by numerically solving 1-D Usadel equation. The dimensions of N are taken as (500 nm, 220 nm, 35 nm) and the diffusion constant is* $D = 75\,cm^2/s$*, yielding* $E_{Th} \approx 20\,\mu eV$*. An ideal case with zero spin-flip scattering rate (*$\Gamma_{sf} = 0$*) and fully transparent contact is considered.*

1.2 Meissner-Ochsenfeld Effect

One of the hallmarks of superconductivity is the expulsion of magnetic field ($\vec{B}$) from the superconducting bulk as the material transitions from normal (N) to superconducting (S) state. The expulsion is made possible by the emerging supercurrent which circulates near superconductor surface and generates the exact opposite flux, leading to the cancellation of $\vec{B}$ inside the bulk. Intuitively, one can expect a non-zero $\vec{E}$ field as $\frac{d\Phi}{dt} \neq 0$ during transition. The momentary presence of $\vec{E}$ should then be enough to set the condensate in motion, leading to the circulating currents with zero resistance. The current density near superconductor surface is given as:

$$\vec{J} = \rho\frac{\hbar}{m}\left(\nabla\theta - \frac{q}{\hbar}\vec{A}\right) \tag{1.27}$$

where ρ, θ and $\vec{A}$ represent the Cooper pair density, phase of the wavefunction $\psi(r) = \sqrt{\rho}e^{j\theta(r)}$ and magnetic vector potential (defined as $\vec{B} = \vec{\nabla}\times\vec{A}$) respectively.

London penetration depth (λ_L): Although superconductors are known to display perfect diamagnetism, the presence of such persistent currents near surface hints at a thin layer into which $\vec{B}$ can penetrate. This characteristic length scale is called London penetration depth (λ_L). Derivation of λ_L from $\vec{J}$ is straightforward.

In Eq. (1.27), applying curl operator ($\nabla\times$) on both sides and using the vector identity $\nabla \times \nabla\theta = 0$, we obtain

$$\nabla \times \vec{J} = -\frac{\rho}{m}(\nabla \times \vec{A}) = -\frac{\rho}{m}\vec{B} \tag{1.28}$$

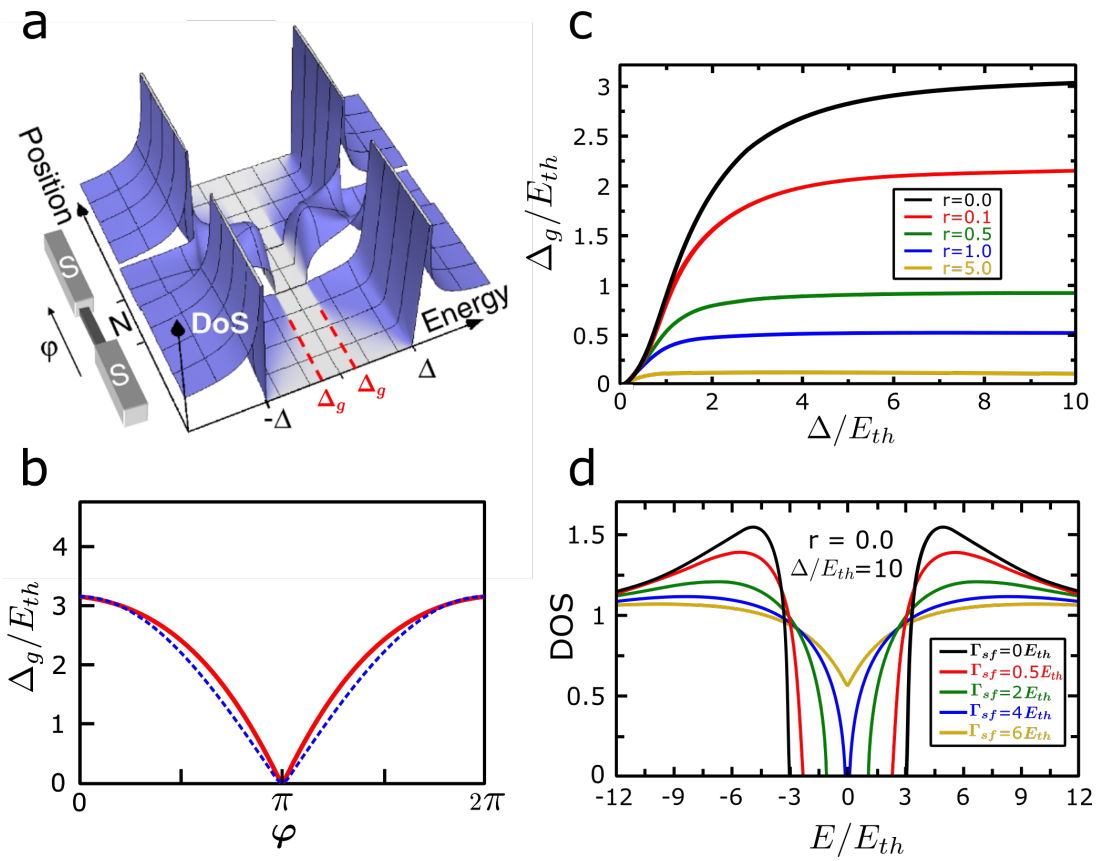

Figure 1.7: ***a.*** *Local DoS in a 1D SNS structure.* Δ *is the superconductor gap.* Δ_g *is the minigap (dashed red) (adapted from [43]).* ***b.*** Δ_g *in units of* E_{Th} *as a function of the Josephson phase* φ *(red).* Δ_g *closes completely at* $\varphi = \pi$*. The analytical curve* $\Delta_g/E_{Th} = 3.15|\cos(\varphi/2)|$ *is given in dashed blue.* E_{Th} *is the Thouless energy. (adapted from [75])* ***c.*** Δ_g *as a function of* Δ *in units of* E_{Th} *at different values of contact transparency, r. Note that in the long junction limit (*$\Delta \gg E_{Th}$*)* $\Delta_g \sim 3.1E_{Th}$ *for* $r = 0$*. (adapted from [74])* ***d.*** *DoS in the long junction limit (*$\Delta/E_{Th} = 10$*) with ideal contacts* $r = 0$*, as a function of energy normalised to* E_{Th} *at different values of spin-flip scattering rate,* Γ_{sf}*. (adapted from [74])*

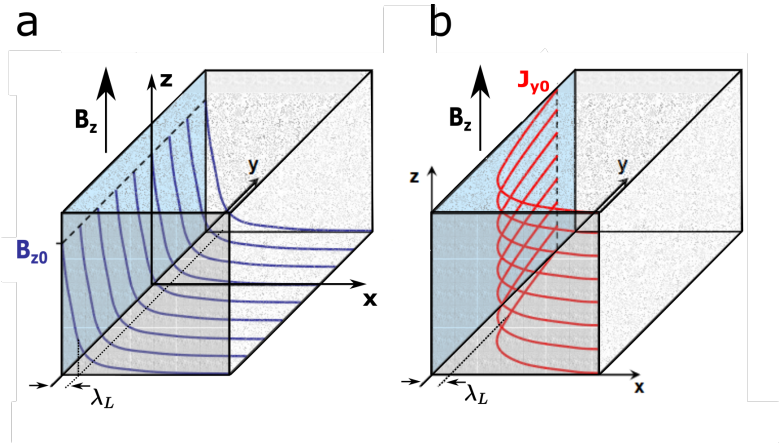

Figure 1.8: Exponential decay of ***a.*** *the magnetic field B (blue)* ***b.*** *the supercurrent density* J_s *(red) with distance x into a bulk superconductor (taken from [40]).*

We can now manipulate Ampère's Law

$$\nabla \times (\nabla \times \vec{B}) = \mu_0(\nabla \times \vec{J}) \tag{1.29}$$

Using vector identity $\nabla \times (\nabla \times \vec{B}) = -\nabla^2\vec{B}$ and inserting Eq. (1.28) in Eq. (1.29), we reach

$$\nabla^2\vec{B} = k^2\vec{B} \quad \left(k^2 = \frac{\mu_0 n q^2}{m}, \quad \rho = nq\right) \tag{1.30}$$

Eq. (1.30) represents the time independent form of a wave equation and yields two eigenfunctions. Opting for the decaying (Be^{-kx}) solution, we find λ_L as:

$$\boxed{\lambda_L = \frac{1}{k} = \sqrt{\frac{m}{\mu_0 n q^2}}} \tag{1.31}$$

The penetration of $\vec{B}$ in the superconducting bulk and the resultant surface current is shown in Fig. 1.8.

1.3 Flux Quantization

Trapped flux. We consider a superconducting ring with thickness $t > \lambda_L$ and ignore its width. As sketched in Fig. 1.9, we first let the transition N $\rightarrow$ S take place in presence of $\vec{B}$ by cooling the system below T_c. Then, we turn off $\vec{B}$. What can we say about the behaviour of our device in such experiment? We can guess that some magnetic flux (Φ) crossing the bulk will be deviated to the center of the loop as the ring becomes superconductor. Next, let us consider a closed path deep inside the ring bulk, any magnetic flux leaving this loop would generate emf according to Faraday's law of induction $\oint \vec{E}.d\vec{r} = -\frac{d\Phi}{dt}$. However, as mentioned in the previous section, superconducting bulk is field-free ($\vec{B} = 0, \vec{E} = 0$). Therefore, $\frac{d\Phi}{dt} = 0$ and Φ inside the ring is trapped.

Quantization. The topological change from simply connected (slab) to multiply connected (ring) shape brings an additional feature to the trapped flux: quantization [77, 78]. In the presence of a magnetic vector potential $\mathbf{A}$ such that $\mathbf{B} = \boldsymbol{\nabla} \times \mathbf{A}$, Aharonov-Bohm effect [79] describes the phase accumulation ($\Delta\theta$) by the wavefunction, Ψ of a charged particle ($q = 2e$) upon displacement from point $\mathbf{a}$ to $\mathbf{b}$ via certain path P in the region where $\mathbf{B} = 0$ and $\mathbf{A} \neq 0$ as

$$\Delta\theta = \theta_b - \theta_a = \frac{2e}{\hbar}\int_P \mathbf{A} \cdot dr \tag{1.32}$$

As $\Psi(x)$ must be a single-valued function of position, $\Delta\theta$ over a complete cycle around the ring can only accept multiples of 2π as value:

$$\frac{2e}{\hbar}\oint_P \mathbf{A} \cdot dr = 2\pi n \tag{1.33}$$

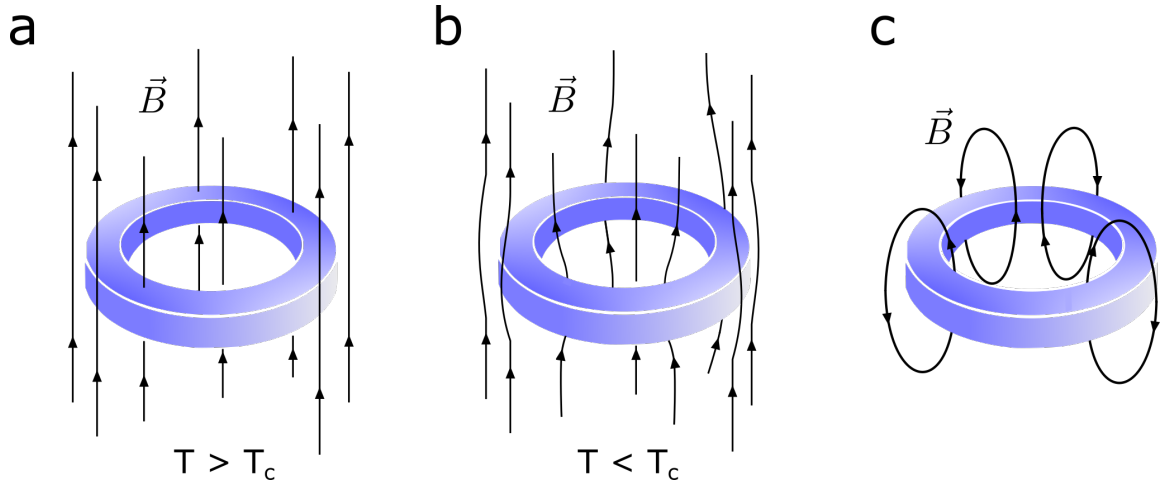

Figure 1.9: A ring in the magnetic field $\vec{B}$ ***a.*** *in the normal state* ***b.*** *in the superconducting state* ***c.*** *after the external field is removed. (adapted from [76])*

Using Stokes theorem, we can rewrite Eq. (1.33) as

$$\frac{2e}{\hbar}\oint_P \mathbf{A}\cdot dr = \frac{2e}{\hbar}\iint \boldsymbol{\nabla}\times\mathbf{A}\cdot\mathbf{ds} = \mathbf{2\pi n} \tag{1.34}$$

Noting that $\boldsymbol{\nabla}\times\mathbf{A}=\mathbf{B}$,

$$\frac{2e}{\hbar}\iint \mathbf{B}\cdot ds = 2\pi n \tag{1.35}$$

The surface integral on the LHS corresponds to the Φ threading the closed path we have taken inside superconductor. Therefore,

$$\frac{2e}{\hbar}\Phi = 2\pi n \tag{1.36}$$

Let us reformulate Eq. (1.36). In the final form,

$$\Phi = n\Phi_0, \quad \Phi_0 = \frac{\hbar}{2e} \approx 2.0678\times10^{-15}\ \text{Wb} \tag{1.37}$$

Eq. (1.37) reveals the striking nature of the Φ trapped inside the ring. Flux can only accept integer multiples (n) of Φ_0 and is therefore quantized. Consequently, Φ_0 is called the **magnetic flux quantum**.

1.4 Phase Slip

The quantized nature of the flux inside the ring is better appreciated within the Ginzburg-Landau model. In cylindrical coordinates $(\vec{r},\vec{\phi},\vec{z})$, assuming a vector potential $\vec{A}=\frac{\Phi}{2\pi r}\vec{\phi}$, the free energy of the system can be written as

$$F_s = F_s^0 + V\left(\frac{\hbar^2}{2m^*}\left|\frac{in}{r}-\frac{2ei\Phi}{2\pi\hbar r}\right|^2|\Phi|^2\right) + \frac{1}{2\mu_0}\int B^3 d^3r \tag{1.38}$$

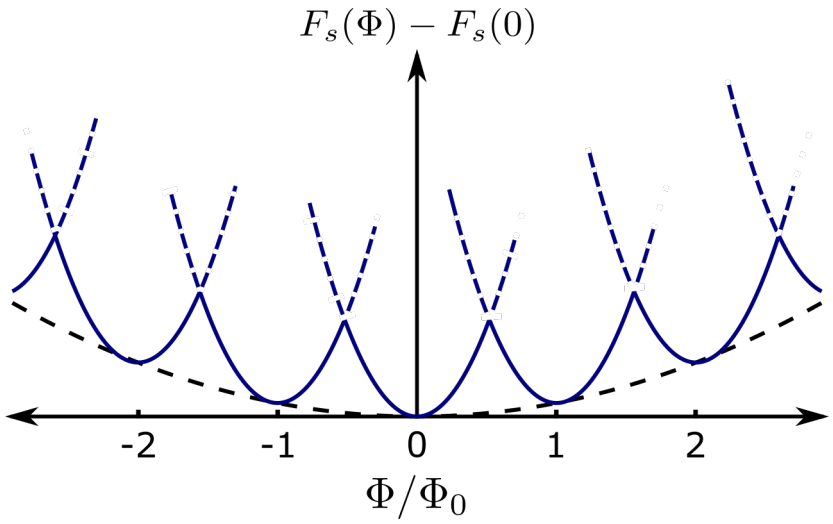

Figure 1.10: Flux quantization in a superconducting ring. Free energy is plotted as a function of the flux (Φ) in units of Φ_0. Metastable energy minima exist when $\Phi \approx n\Phi_0$. The overall background increase with Φ stems from the self-inductance of the ring, making the zero flux state ($\Phi = 0$) the global energy minimum. Φ_0 is the magnetic flux quantum. (adapted from [80])

where F_s^0 represents the system's energy in the absence of circulating current and external $\vec{B}$. V is the loop volume. The second and the third terms of the right hand side correspond to the energy associated with wavefunction (Ψ) and the loop inductance (L), respectively. Focusing on the Φ-dependent terms, we can rewrite Eq. (1.38) as

$$F_s(\Phi) = F_s(0) + const.(\Phi - n\Phi_0)^2 + const.\frac{\Phi^2}{2L} \tag{1.39}$$

The energy diagram of the system ($F_s(\Phi) - F_s(0)$) with respect to Φ/Φ_0 is traced in Fig. 1.10. It demonstrates that the free energy has local minima in where $\Phi \simeq \Phi_0$. Hence, as the transition $N \rightarrow S$ occurs, the system settles in one of those metastable points depending on the external $\vec{B}$. Turning off $\vec{B}$ then induces a persistent current circulating around the ring as the system must sustain the same Φ in the center. This phenomenon is known as the persistent current [81].

Under certain conditions, the energy barrier (U_0) which keeps the system in a given metastable point can be overcome. Such a scenario corresponds to a momentary suppression of the wavefunction in a localized region during which the phase goes through 2π cycle and the system falls into the next metastable minima, causing dissipation. Such event is called a **phase slip**. Phase slips are intimately related to the fluctuations in superconductors. They proliferate in reduced dimensions and alter significantly the superconductor properties with respect to the bulk [82–85]. Based on the nature of fluctuations, we can talk about two phase slip mechanisms:

1. Thermal activation ($k_bT \sim U_0$): At $T \neq 0$, thermal fluctuations raise the system's free energy by $\sim k_bT$, thus leading to a finite probability for thermal hopping over the energy barrier, U_0, whenever $k_bT \sim U_0$ (Fig. 1.11a). Thermally activated phase slips

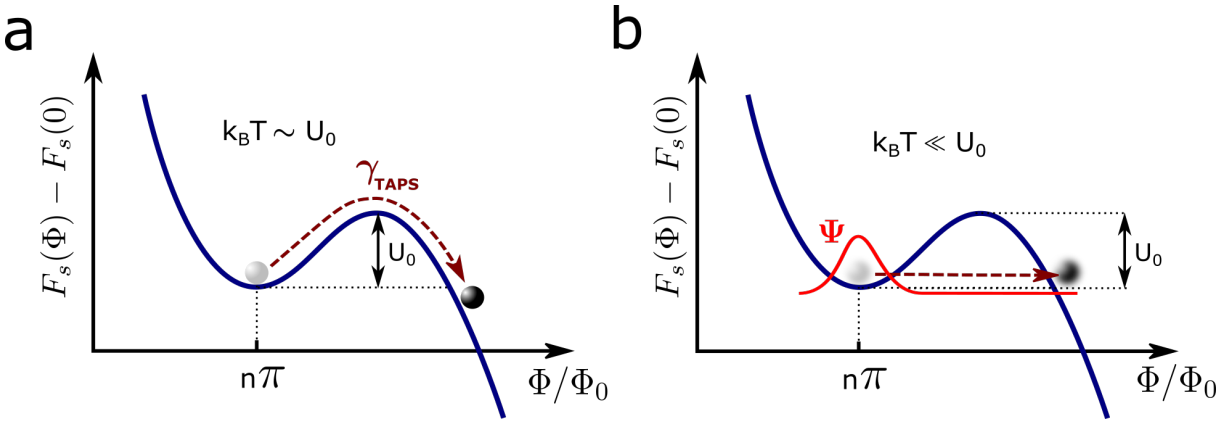

Figure 1.11: ***a.*** *Thermally activated phase slip. The phase particle surmounts U_0 with a rate γ_{TAPS} when $k_bT \sim U_0$* ***b.*** *Quantum phase slip. The wavefunction Ψ representing the flux tunnels through the potential barrier. U_0 is the barrier height.*

(TAPS), were shown to be the underlying mechanism of the finite resistivities observed in narrow superconducting channels near T_c [86, 87]. The theory of TAPS was developed by Langer &Ambegaokar [88] and McCumber & Halperin [39]. The so-called LAMH model associates the finite resistance below T_c with an escape rate given by the activation function:

$$\gamma_{\mathrm{TAPS}} = \Omega e^{-U_0/k_bT} \tag{1.40}$$

where U_0 represents the potential barrier and the prefactor Ω sets the timescale of thermal fluctuations.

2. Quantum tunneling ($k_bT \ll U_0$): Thermally activated phase slips are exponentially suppressed as T is lowered. Hence, below a crossover temperature T_{cr} [89], quantum fluctuations become the primary cause of phase slips. A quantum phase slip (QPS) corresponds to the tunneling of the wavefunction through the energy barrier of height U_0 (Fig.1.11b). In superconducting nanowires ($\varnothing < 10\,\mathrm{nm}$), the destruction of superconductivity due to QPS has been predicted theoretically [85]. A large body of experiments have been dedicated to the observation of incoherent [90–93] and coherent QPS [94–96] in superconducting nanowires as well as in Josephson junction chains [97–100].

1.5 RF-SQUID

In the previous section, we investigated the properties of a superconducting loop and elaborated on the resultant flux quantization. Next, we incorporate a single Josephson junction into the loop (Fig. 1.12). The family of devices including a superconducting loop interrupted by a single or more than one Josephson junctions is called Superconducting Quantum Interference Device (SQUID) [101, 102]. The particular configuration having a single Josephson junction is called Radio Frequency SQUID due to its operation mode and it was proposed for the first time in the early 1970s [103–106]. It is the core element

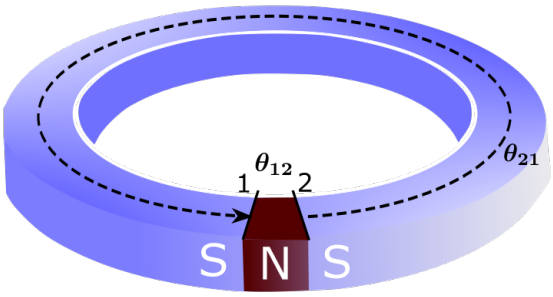

Figure 1.12: A representative sketch of an RF-SQUID. The superconducting ring (blue) is interrupted by a weak link.(dark red) θ_{21} is the phase drop of the wavefunction in the superconducting part (dashed). θ_{12} corresponds to the phase drop over the normal part.

of our experiments. For this reason, we are going to detail its working principles.

Fundamentals. As it was the case for the SC loop, the macroscopic wavefunction (Ψ) has 2π periodicity over a closed cycle which we represent as:

$$\oint_C \nabla\theta \cdot dl = \theta_{21} + \theta_{12} = 2\pi n \tag{1.41}$$

where θ_{21} corresponds to the phase drop over the weak link which we write in terms of gauge invariant phase difference (φ) as

$$\theta_{12} = \varphi + \frac{2\pi}{\Phi_0}\int_1^2 \vec{A}\cdot d\vec{l} \tag{1.42}$$

and θ_{12} is the accumulated phase throughout the SC part.

$$\theta_{21} = \frac{2\pi}{\Phi_0}\int_2^1 \lambda_L \vec{J}\cdot d\vec{l} + \frac{2\pi}{\Phi_0}\int_2^1 \vec{A}\cdot d\vec{l} \tag{1.43}$$

Summing Eq. (1.42) and Eq. (1.43) ($\theta_{21} + \theta_{12} = 0$),

$$\varphi + \frac{2\pi}{\Phi_0}\Bigg(\underbrace{\int_1^2 \vec{A}\cdot d\vec{l} + \int_2^1 \vec{A}\cdot d\vec{l}}_{\oint_C \vec{A}\cdot d\vec{l}}\Bigg) + \underbrace{\frac{2\pi}{\Phi_0}\int_2^1 \lambda_L \vec{J}\cdot d\vec{l}}_{0} = 0 \tag{1.44}$$

We take the integral contour inside the bulk such that $\vec{J} = 0$. Thus, Eq. (1.44) becomes

$$\varphi = \frac{2\pi}{\Phi_0}\oint_C \vec{A}\cdot d\vec{l} \tag{1.45}$$

Noting that the integral on RHS corresponds to Φ threading the loop we arrive at

$$\boxed{\varphi = \frac{2\pi}{\Phi_0}\Phi} \tag{1.46}$$

Eq. (1.46) shows the fundamental property of RF-SQUID. The Josephson phase (φ) is directly controlled by the external Φ. Hence, the circulating supercurrent $I_s = I_c \sin\varphi$ is a periodic function of Φ with the period Φ_0.

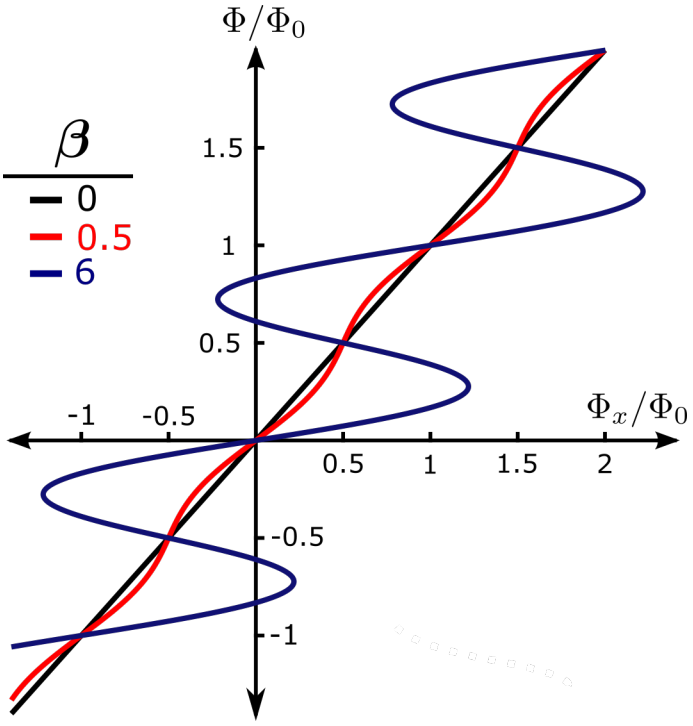

Figure 1.13: Total flux (Φ) threading RF-SQUID as a function of the external flux (Φ_x) in units of Φ_0 at three different values of β. $\Phi(\Phi_x)$ is multi-valued at $\beta = 6$ which is manifested as hysteretic behaviour in practice. β is the screening parameter. Φ_0 is the magnetic flux quantum.

Screening parameter. I_s induces a flux (LI_s) via the loop inductance (L) which partly screens the external flux, Φ_x. Therefore, it needs to be included in the total flux as:

$$\Phi = \Phi_x - LI_s \tag{1.47}$$

Inserting Eq. (1.47) in Eq. (1.46)

$$\varphi = -\frac{2\pi}{\Phi_0}(\Phi_x - LI_s) \tag{1.48}$$

and noting that $I_s = I_c \sin(\varphi)$, we reach

$$\boxed{\frac{\Phi}{\Phi_0} = \frac{\Phi_x}{\Phi_0} - \frac{\beta}{2\pi}\sin\left(2\pi\frac{\Phi}{\Phi_0}\right)} \tag{1.49}$$

where $\beta = \frac{2\pi LI_c}{\Phi_0}$ is called the screening parameter. Eq. (1.49) captures the non-trivial relation between Φ and Φ_e. We identify two distinct regimes depending on the value of β:

1. Weak Screening ($\beta < 1$): An equivalent interpretation of β becomes visible when we reformulate it as $\beta = \frac{L}{L_J}$ where $L_J = \frac{\Phi_0}{2\pi I_c}$ denotes the Josephson inductance. Therefore, $\beta < 1$ corresponds to the case where the phase drop occurs mostly on the Josephson junction. The flux induced by the loop (LI_s) is smaller than Φ_0, hence the screening is

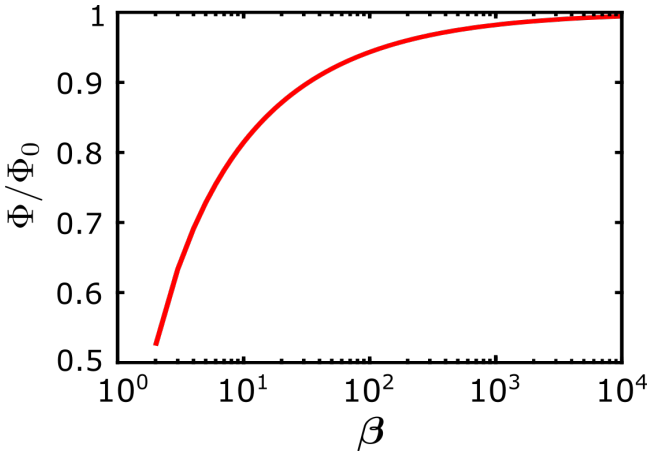

Figure 1.14: The ratio of the flux jump magnitude over Φ_0 in RF-SQUID as a function of the screening parameter β. Note that $\Phi \to \Phi_0$ as β grows.

negligible. This leads to a single-valued $\Phi(\Phi_x)$ and Φ follows Φ_x almost linearly (Fig. 1.13).

2. Hysteretic Mode ($\beta > 1$): SQUID screening of Φ_x is effective and (LI_s) becomes the dominant term in Eq. (1.49), to such an extent that $\Phi(\Phi_x)$ is no longer single-valued. In practice, the multi-valued nature of the $\Phi(\Phi_x)$ translates into hysteretic behaviour. As Φ_x is increased, Φ follows less rapidly but in a continuous manner up to $\Phi \sim \Phi_0/4$. At this point, Josephson junction has $\varphi \simeq \pi/2$ and $max(I_s)$ is reached. Therefore further screening is not possible. Increasing Φ_x further, SQUID momentarily switches to the voltage state and Φ_0 penetrates in the loop, increasing the winding number $n = n + 1$. Sweeping Φ_x in the negative direction this time, circulating I_s builds up in the opposite way and the transition $n + 1 \to n$ takes places when $\varphi \sim -\pi/2$ is reached.

Phase slip in SQUID. The mechanism for Φ_0 entering/leaving the SQUID bears a great resemblance to the phase slips in fully superconducting rings, however, with two distinctions: (1) 2π periodicity of flux quantization becomes fractional due to the presence of the weak link and converges to $\Phi \approx n\Phi_0$ only for $\beta \gg 1$ (Fig. 1.14). Thus, the hysteretic SQUID can be seen as a permeable superconducting loop with a limited screening capacity where some Φ already leaks into the loop prior to a slip. (2) Unlike the stochastic nature of TAPS and QPS, the above-mentioned phase slips in hysteretic SQUIDs are deterministic. They are generated experimentally by sweeping Φ_x. The unfolding of a such deterministic phase slip is better appreciated with the help of an energy landscape.

Potential landscape The potential energy, $U(\Phi)$, of a SQUID consists of the magnetic energy stored in the JJ $(E_j(1 - \cos\varphi))$ and in the loop inductance $\left(\frac{\Phi^2}{2L}\right)$:

$$U(\Phi) = E_j(1 - \cos\varphi) + \frac{\Phi^2}{2L} \tag{1.50}$$

Let us reformulate Eq. (1.50) so that the β and $(\varphi_x = \frac{2\pi\Phi_x}{\Phi_0})$ dependence becomes visible:

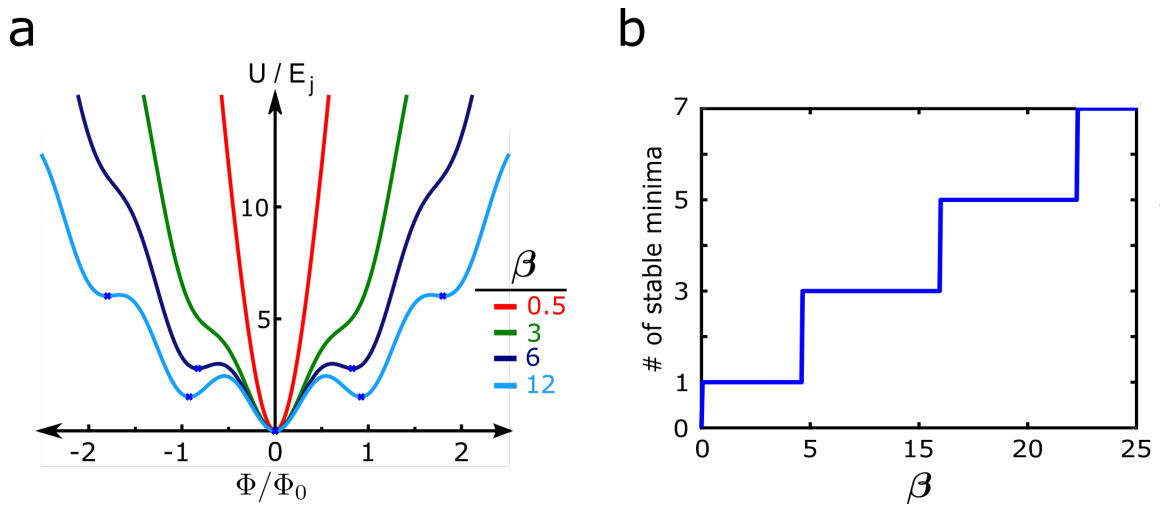

Figure 1.15: ***a.*** *The potential energy (U) landscape of RF-SQUID normalised to E_j as a function of the total flux (Φ) in units of Φ_0 at different values of β. Metastable points are marked in dark blue cross. $\Phi = 0$ corresponds to the global minimum. β is the screening parameter. E_j is the Josephson energy. Φ_0 is the magnetic flux quantum* ***b.*** *Number of stable points in a RF-SQUID as a function of β.*

$$U(\varphi) = E_j \left(1 - \cos\varphi + \frac{(\varphi - \varphi_x)^2}{2\beta}\right) \tag{1.51}$$

Fig. 1.15 displays $U(\Phi)$ at $\Phi_x = 0$ for various β. Note the increasing number of metastable equilibrium points as β grows, such that a potential landscape similar to that of fully SC ring is obtained for $\beta \gg 1$. Applying Φ_x modifies $U(\Phi)$ and a phase slip arises upon the removal of the metastable point in which the system was initially settled. The system evolves into the neighbouring local minimum, simultaneously admitting a fraction of Φ_0 into the loop. The difference in internal energy (δU) is dissipated (Fig. 1.16). The dissipation can also be justified from thermodynamics point of view. Until $\varphi \approx \pi/2$, the initial state can be restored without any thermodynamic change. Therefore, the evolution of $U(\Phi)$ is a reversible process up to this point. Beyond, the phase slip introduces irreversibility which is necessarily accompanied by dissipation.

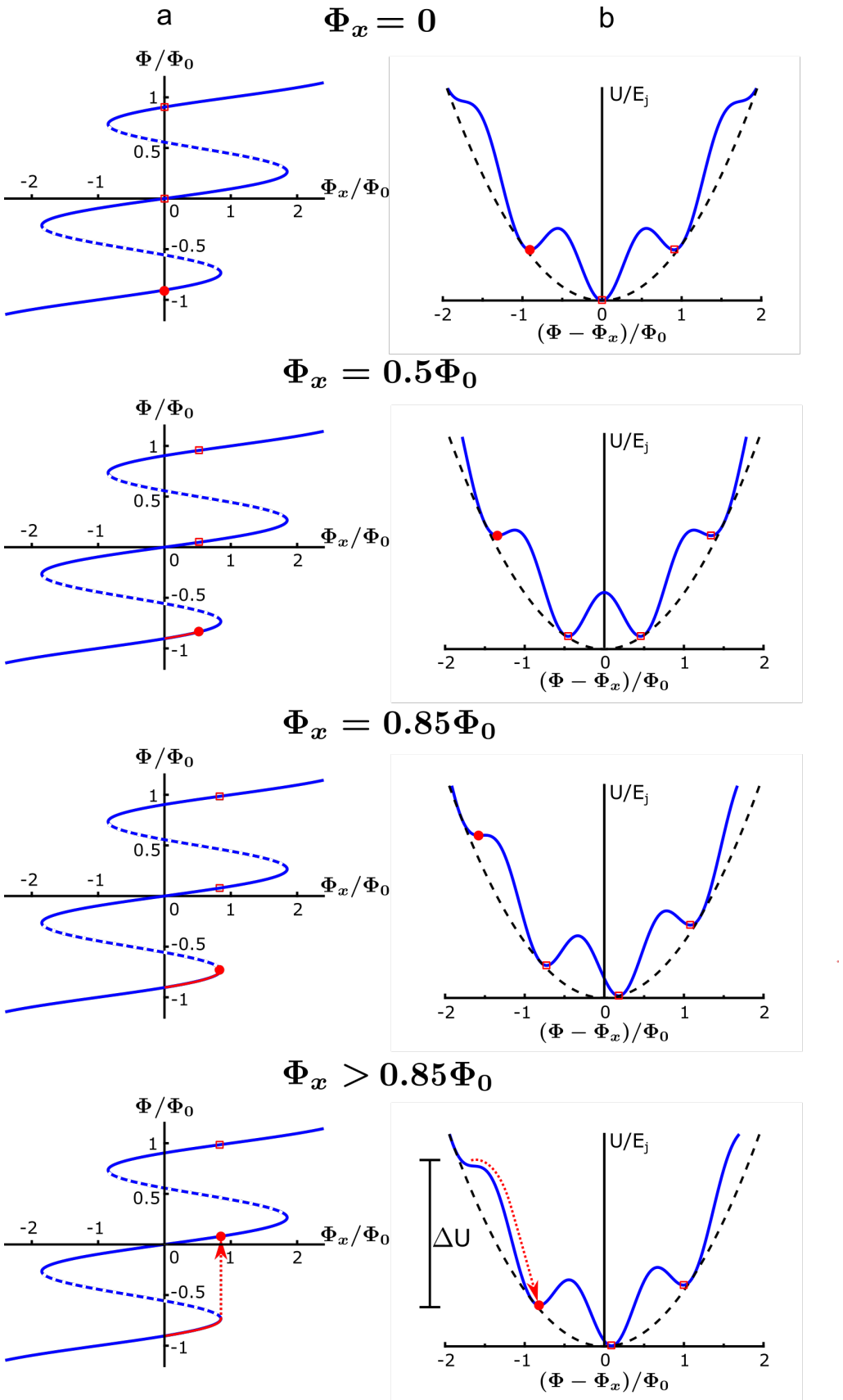

Figure 1.16: The evolution of the ***a.*** *stable* Φ *values as a function of the external flux* Φ_x *plotted in* $\Phi - \Phi_x$ *plane for* $\beta = 10$*. Both axes are normalised to* Φ_0*. The current state of the system is marked in red circle (filled). Other stable points are marked in red square. The unstable regions are dashed blue.* ***b.*** *Potential energy landscape (U) with respect to* Φ_x *in a moving frame of reference* $\Phi - \Phi_x/\Phi_0$*. At* $\Phi_x > 0.85\,\Phi_0$*, the current state becomes unstable and the system settles in the next stable point. The difference in the free energy* (ΔU) *is dissipated.* Φ_0 *is the magnetic flux quantum.*

Chapter 2

Thermometry, Bolometry, Calorimetry

2.1 Introduction

This chapter aims to serve as a brief reminder on the fundamental concepts of thermodynamics and explains the operating principles of the thermometers, bolometers and calorimeters. We begin by deriving the temperature from the entropy maximum postulate of thermodynamics. Next, the concept of thermometer is discussed and various thermometer types are given. Here, the emphasis is on the superconducting hybrid junctions including the normal metal - insulator - superconducting (NIS), superconducting - normal - superconducting (SNS) and proximity induced normal metal - insulator - superconducting (N′IS) types as the thermometer employed in this project is a member of this category. The following sections are dedicated to the bolometery and the calorimetry where we skim through the examples of both detection concepts at the micro/nano scale. As a side note, we briefly discuss the experimental work realized on the absorber layer of a microbolometer prototype in the context of a collaboration with CEA-LETI. Recently, bolometer and calorimeter devices at nano scale have witnessed an increasing interest thanks to the flourishing fields such as quantum thermodynamics and quantum computing. Within this scope, new devices for studying quantum thermodynamics have been proposed [107, 108].

2.2 Temperature

Let us consider a composite system which consists of two macroscopic bodies separated from each other by a fixed and adiabatic piston (Fig. 2.2). The subsystems are completely characterized by their extensive parameters (U, V, N) which correspond to the internal energy, volume and the mole number, respectively [109]. The system is closed with

respect to the outer world which we express as

$$U_1 + U_2 = constant \tag{2.1}$$

Next, let us remove one of the internal constraints, namely the adiabaticity of the piston such that the heat transfer between the subsystems is now allowed. "What is going to be the new equilibrium state ?" is the fundamental question answered by the entropy maximum postulate of thermodynamics.

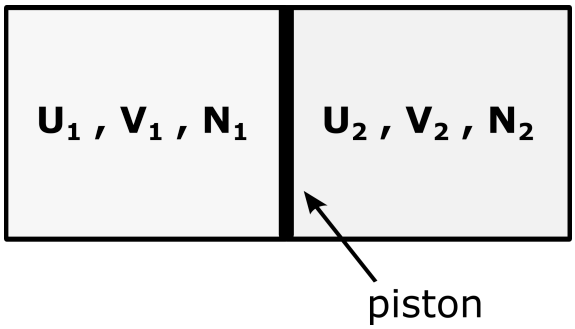

Figure 2.1: The closed, composite system. A fixed adiabatic piston separates the subsystems from each other.

Among a myriad of configurations, the system evolves into the final state which maximizes the entropy function [110]

$$S(U, V, N) = S_1(U_1, V_1, N_1) + S_2(U_2, V_2, N_2) \tag{2.2}$$

We can write the maximum entropy (equilibrium) condition as

$$\frac{dS}{dU} = \frac{dS_1}{dU_1} + \frac{dS_2}{dU_2}\frac{dU_2}{dU_1} = 0 \tag{2.3}$$

Given the fact that the total energy is conserved ($dU_1 = -dU_2$), Eq. 2.3 can be written as

$$\frac{dS_1}{dU_1} - \frac{dS_2}{dU_2} = 0 \quad \Rightarrow \quad \frac{dS_1}{dU_1} = \frac{dS_2}{dU_2} \tag{2.4}$$

Therefore, the bodies which are in the state of thermodynamic equilibrium share a constant dS/dU. The reciprocal of this thermodynamic handshaking point is defined as temperature

$$T = \frac{dU}{dS} \quad \Rightarrow \quad \frac{1}{T_1} = \frac{1}{T_2} \quad \Rightarrow \quad T_1 = T_2 \tag{2.5}$$

It should be noted that temperature is a statistical quantity which is only valid for entities with many degrees of freedom such as macroscopic objects made of very large number of particles.

2.3 Thermometer

The zeroth law of thermodynamics [111] states that *"if two systems are separately in thermal equilibrium with a third, then they are in thermal equilibrium with each other."* Such an equivalence relation makes sure that there exists a scale of temperature which is the same for systems in thermal equilibrium, therefore serves as the basis for measuring temperature. Thermometer describes all sorts of devices which serve to measure temperature. A typical thermometer consists of (1) a sensor which responds to the temperature (2) a means to convert the sensor response into a numerical value. Depending on the need for calibration, we can classify the thermometers into two categories:

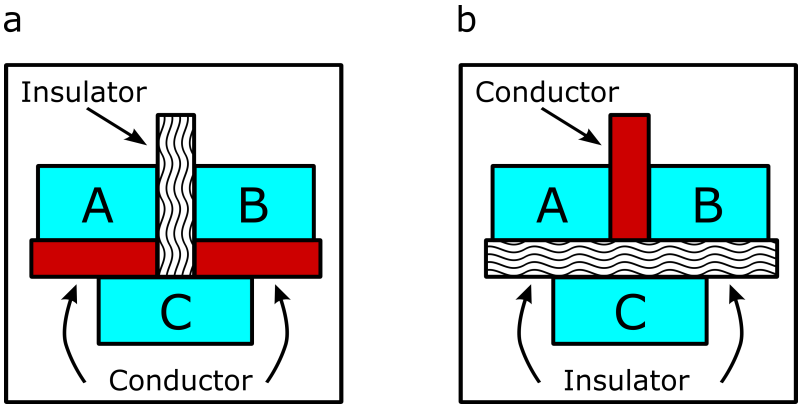

Figure 2.2: ***a.*** *The bodies A and B are each in thermal equilibrium with C.* ***b.*** *Exchanging the position of the insulator and the conductor slabs, no change is observed which proves that A and B are in thermal equilibrium with each other. The system C serves as the thermometer. (adapted from [112])*

1. Primary thermometer: The systems whose fundamental equation is well known such that the absolute temperature can be obtained directly from the measurements without calibration are called primary thermometers. To mention a few examples, the gas thermometer exploits the relation $PV = nRT$ of the ideal gas where $R \approx 8.314\ Jmol^{-1}K^{-1}$ is the universal gas constant and n is the number of moles. Temperature is obtained by measuring the pressure (P) in constant volume (V) configuration or vice versa [113]. The Coulomb blockade thermometry (CBT) uses the $I-V$ relation of an array of single electron tunneling (SET) devices in the partial Coulomb blockade regime [114–116]. The full width at half maximum of conductance dip has the value $V_{1/2} \approx 5.439\, Nk_BT$ which yields T without any calibration [117]. In noise thermometers, the noise voltage variance on a resistance R is measured which gives T via Johnson-Nyquist theorem $\langle v_n^2 \rangle = 4k_BT\Delta f R$ where Δf is the measurement bandwidth [118].

2. Secondary thermometer: The family of thermometers which require a calibration against a primary thermometer at least at one temperature is called secondary thermometers. Unlike the primary thermometers which are difficult to operate and thus mostly employed in metrology, the secondary thermometers are usually easy to operate

and therefore have a widespread use in various fields. In low temperature experiments, resistance thermometry is the most commonly used method which exploits the temperature dependence of the electrical resistance of a particular material (Fig. 2.3). The operating temperature range, sensitivity, response time, ease of calibration, self-heating and sensitivity to environmental changes are among the major criteria which determine the choice of material. Pure metals such as platinum are used as resistance thermometers (Pt100) from T_{room} down to $\sim 20\,\mathrm{K}$ thanks to their linear R(T) curve in this range [119]. Iron doped rhodium (RhFe) [120] provides approximately linear R(T) between $0.1\ \mathrm{K} < T < 1$ K. Among semiconductors, highly doped germanium is preferred for its stability over thermal cycles [113]. Other materials such as sintered carbon grains [121] and metal-ceramic composites including RuO_2 [122] are frequently used in millikelvin range.

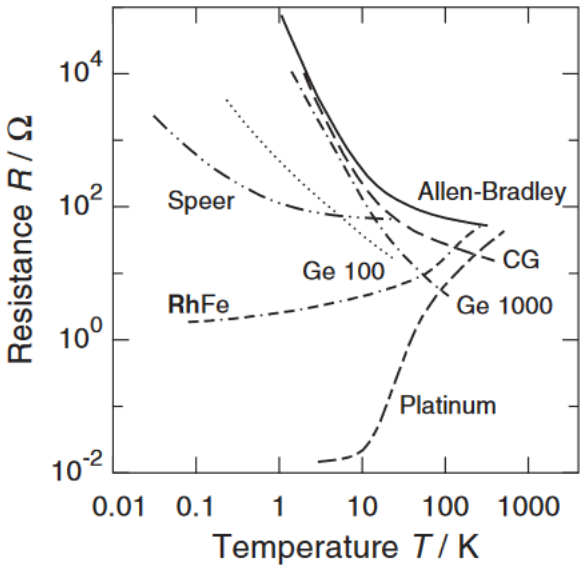

Figure 2.3: Temperature dependence of various materials used as a thermometer. RhFe stands for iron-doped rhodium. Speer and Allen-Bradley refer to the carbon resistors from two different manufacturers. Ge 100 and Ge 1000 are commerical germanium thermometers. CG stands for a carbon-glass thermometer. (Taken from [123])

2.3.1 Superconducting Hybrid Junctions

NIS Thermometer

The hybrid structure made of a normal metal (N) seperated from the superconductor (S) via an isolating layer (I) is called an NIS junction. For a typical NIS junction at thermal equilibrium (Fig. 2.4), the net tunneling current (I_{NIS}) of the quasiparticles writes [124]

$$I_{NIS} = -e \int_{-\infty}^{+\infty} dE(\Gamma_{N\to S} - \Gamma_{S\to N}) \tag{2.6}$$

where the tunneling rate of quasiparticles $\Gamma_{N\to S}$ is proportional to the tunneling probability: $P_{N\to S}(E)$, the number of available states in N: $N_N(E-eV)\times f_N(E-eV)$ and the number of unoccupied states in S: $N_S(E)\times(1-f_S(E))$ and vice versa. Note that $f_{N,S}$ represents the Fermi distribution of quasiparticles in N,S and $N_{N,S}$ represents the quasiparticle density of states. In a simplified version, Eq. (2.6) can be written as

$$I_{NIS}(V)=\frac{1}{2eR_T}\int_{-\infty}^{+\infty}N_S(E)[f_N(E-eV)-f_N(E+eV)]dE \tag{2.7}$$

where R_T is the tunnel resistance. I_{NIS} shows only an indirect dependence on T_s via

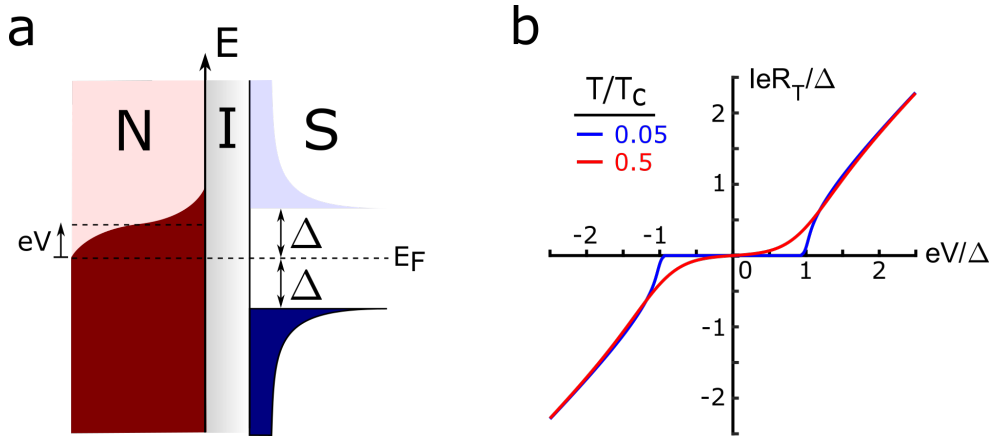

Figure 2.4: ***a.*** *Energy diagram of a NIS junction. An applied voltage V shifts the N-DOS by eV with respect to the Fermi level (E_F). Superconductor features a gap of 2Δ in the excitation spectrum. The occupied states are coloured with dark red (blue) in N (S).* ***b.*** *The calculcated I(V) curve of the NIS junction at two temperatures: $T/T_c=0.05$ (blue) and $T/T_c=0.5$ (red). The voltage axis is normalized to Δ and the current axis is expressed via eR_T/Δ where R_T is the tunneling resistance.*

$N_S(E)=N_N(E)\left(|E|/\sqrt{E^2-\Delta(T)^2}\right)$ where $\Delta(T_s)\approx 1.74\sqrt{1-T/T_c}$ and $\Delta(T)\sim\Delta(0)$ for $T<0.3\,T_c$. At $eV<\Delta$ and for $k_BT\ll\Delta$, the slope of the normalized conductance gives a direct access to the electronic temperature (T_e) of N:

$$\ln\frac{dI_{NS}(V)}{dV}\propto\frac{eV}{k_BT_e}+\frac{1}{2}\ln\left(\frac{\Delta\pi}{2R_T^2k_BT_e}\right)-\frac{\Delta}{k_BT_e} \tag{2.8}$$

Therefore, it can be used as a thermometer to probe the electronic temperature of N. In most of the practical cases, the NIS thermometer is rather employed as a secondary thermometer where the NIS junction is current biased and the voltage output is read. The V(T) curve is calibrated to the bath temperature.

SNS Thermometer

In Chapter 1, we elaborated on the physics of SNS junctions in the diffusive regime and showed the evolution of the critical current (I_c) with temperature. The temperature

dependence of I_c can be used as a secondary thermometer calibrated against the bath temperature. The operating temperature range is determined by the Thouless energy (E_{th}): at $k_BT \gg E_{Th}$, the voltage $V = R_N I_c$ becomes hard to detect against the noise voltage $\sqrt{\langle v_n^2 \rangle}$ whereas in the lower limit ($k_BT < E_{Th}$) the thermometer suffers from saturating $I_c(T)$ curve. A typical SNS thermometer is operational within the temperature window 30 mK $< T <$ 600 mK unless limited by self-heating or electronic noise at the lower limit. One straight-forward method to obtain $I_c(T)$ is to ramp the current bias through the SNS junction and measure the voltage across in a four-probe setup. While incrementing the temperature, the switching current I_{sw} vs temperature curve then provides the thermometer (Fig. 2.5). The stochastic nature of the switching $N \rightarrow S$ calls for a statistics treatment. Therefore, a rigorous approach is to extract the transition statistics and designate the most frequent I_{sw} as the critical current. This method has been demonstrated in [125] where a triangular AC signal at $f = 300$ Hz is applied on the current bias and the switching current counts are recorded with the oscilloscope trigger (Fig. 2.6).

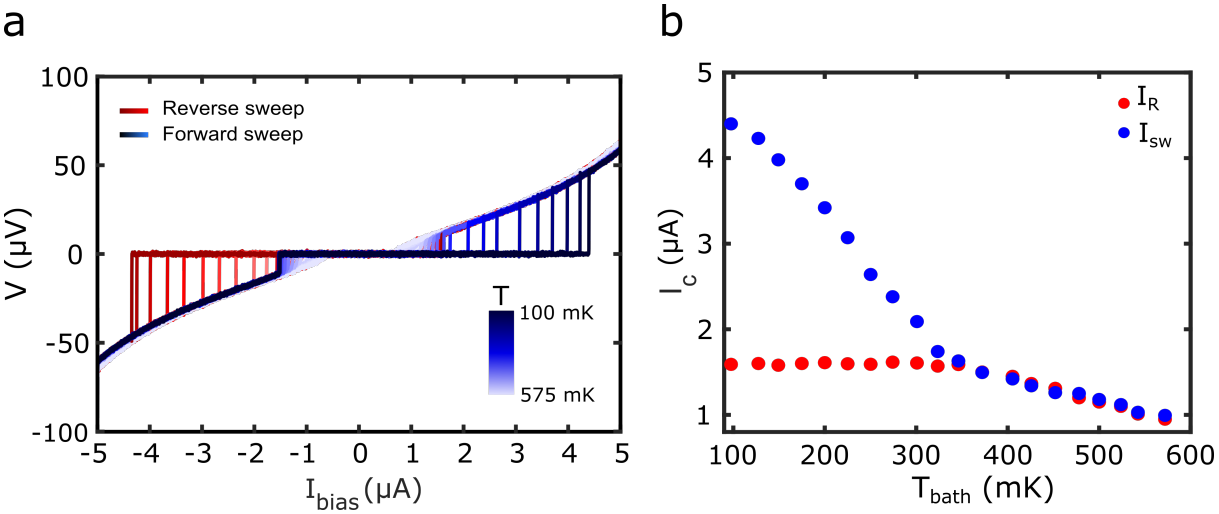

Figure 2.5: ***a.*** *V(I) curve of an SNS Junction. The forward (reverse) sweep is marked in blue (red).* ***b.*** *I_{sw} and I_R as a function of the bath temperature obtained from* ***a.*** *The hysteresis visible in both subfigures is of thermal origin. Namely, whenever the system switches to the resistive state, Normal island sees an increase in temperature due to the steady-state ohmic heating. As a consequence, the critical current (I_c) of the junction decreases to $I_c^{steady-state}$ such that sweeping I_{bias} in the negative direction, the transition $N \rightarrow S$ now occurs when at $I_{bias} = I_R = I_c^{steady-state}$*

Proximity Thermometer

So far, we covered the NIS and SNS junction thermometers. As explained above, NIS thermometer exploits the temperature dependence of the sub-gap conductance which is proportional to the quasiparticle density of states whereas a SNS thermometer uses

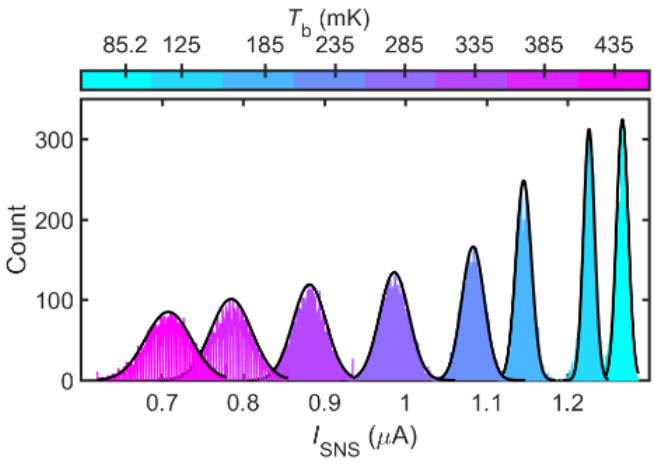

Figure 2.6: Switching current histograms at various bath temperature (T_{bath}). Each histogram is fitted with a Gaussian function. The broadening of the histograms at higher T_{bath} originates from the increased thermal noise (taken from [125]).

the switching threshold of the coherent supercurrent. Despite having different working principles, both concepts require biasing. NIS thermometer is voltage biased below the gap edge and the SNS thermometer is current biased both in DC and AC configurations. Overheating introduced by the finite bias, reported for both NIS [126, 127] and SNS junctions [128], makes their use difficult below 100 mK. An alternative method is to use the finite density of Cooper pairs inside a proximitised normal metal (N') which constitutes a tunneling supercurrent when a hybrid $N'IS$ junction is formed (Fig. 2.7). This phenomenon is known as the zero bias anomaly effect [2, 129, 130] owing to the fact that the Cooper pairs reside at E_F. The temperature dependence of the tunneling supercurrent across a $N'IS$ junction can be exploited as a sensitive thermometer [1]. Compared to the previous thermometers, the above-mentioned method has the advantage of being less invasive in terms of deposited heat thanks to the absence of finite bias and having an increased sensitivity.

The critical supercurrent across the $N'IS$ is given by [2]

$$I_c = \frac{2\pi k_B T}{eR_T} \sum_{n\geq 0} F_S(\omega_n) F_N(\omega_n) \tag{2.9}$$

where F_S and F_N represent the respective Cooper pair amplitudes inside the superconductor and the normal metal. The sum goes over the Matsubara frequencies $\omega_n = (2n+1)\pi k_B T$. With the assumption of a linearized Usadel equation [62], I_c^0 takes the form

$$I_c^0(\varphi) = \frac{2\pi k_B T}{eR_T} \alpha_B \cos(\varphi/2) \sum_{n\geq 0} \frac{\Delta^2 q_n}{(\omega_n^2 + \Delta^2)\left[\alpha_B \alpha \sqrt{\frac{\omega_n}{\Omega_n}} \sinh(q_n/2) + \cosh(q_n/2)\right]} \tag{2.10}$$

Here, $q_n = \sqrt{2\omega_n/E_{\mathrm{Th}}}$ and $\alpha_B \in [0,1]$ is the transparency parameter related to the quality of the SN interfaces. $\alpha = \sigma_N/\sigma_S$ represents the ratio of the normal state conductances be-

tween the normal and the superconducting electrodes. Finally, the tunneling supercurrent (I_s) across the $N'IS$ junction is expressed as

$$I_s(V) = \frac{\pi e \hbar I_c^{0\,2}}{(2e)^2} [P(2eV) - P(-2eV)] \tag{2.11}$$

where $P(E)$ is the probability for an electron to emit a photon of energy E into the electromagnetic environment during the inelastic tunneling process. The latter function depends on the impedance $Z(\omega)$ seen by the junction whose details can be found in [2]. In an $I(V)$ measurement across the $N'IS$ junction, the proximity effect manifests itself as the anti-symmetric peaks around the origin (Fig. 2.7c). Probing the temperature dependence of the differential conductance at $V_{bias} = 0\,\mathrm{V}$ therefore provides a secondary thermometer calibrated against the bath temperature.

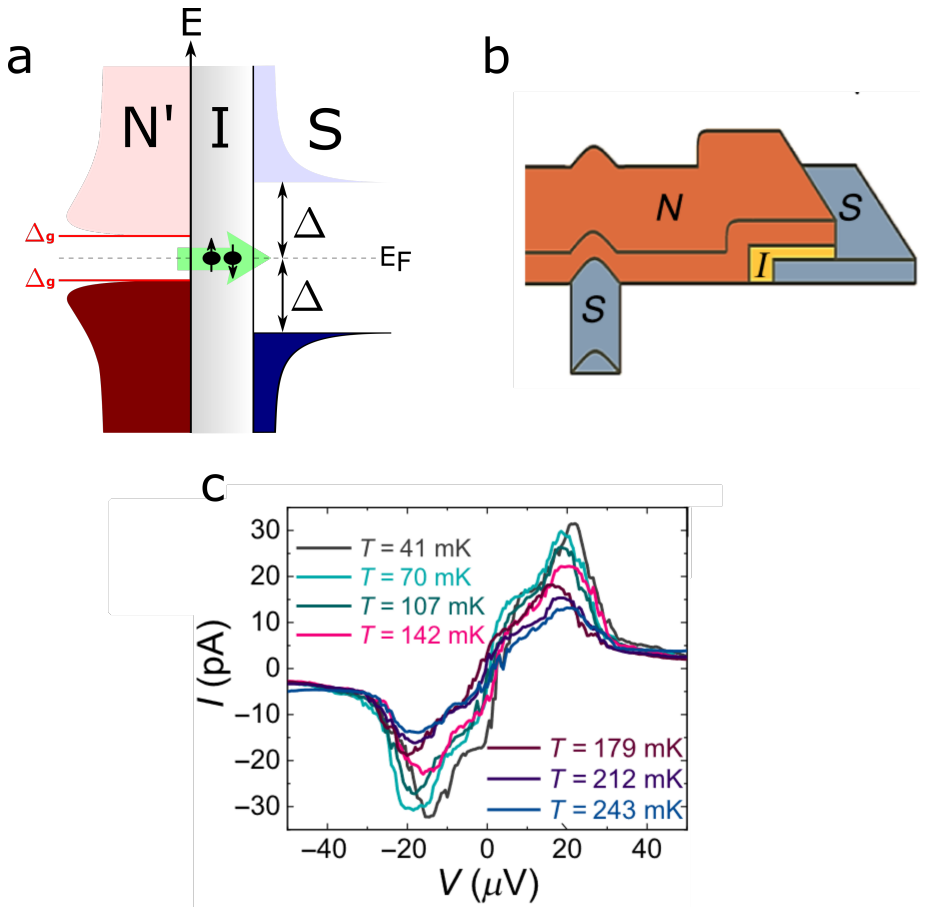

Figure 2.7: ***a.*** *Energy diagram of a $N'IS$ junction. Note the minigap Δ_g present in the N'-DOS. The so-called Andreev pairs tunneling between N' and S are depicted with a green arrow.* ***b.*** *Drawing illustrates the typical $SN'IS$ configuration. The clean SN contact induces the proxmity in N whereas NIS junction serves as the thermometer (taken from [2]).* ***c.*** *$I(V)$ measurements taken at various temperatures between $T = 41$ mK and $T = 243$ mK (taken from [2])*

2.4 Bolometer

A bolometer is a radiation detector. In the strict sense, the term designates the family of sensors which detects the EM waves in the infrared and millimeter wavelength (f = 100 GHz−10 THz) via absorption of radiation. Given the spectrum of interest, bolometers have a wide range of applications, for example in astrophysics [131–134], terahertz imaging [135], military [136] and cQED [137]. A typical bolometer consists of an absorbing layer thermally isolated from the heat bath via suspending structures. The absorbing layer is in thermal contact with a temperature dependant resistor (thermistor) whose calibration curve is known to the user (Fig. 2.8). Often, a reflector layer is placed at the bottom of the membrane to enhance the absorption. In the presence of incident radiation, the absorbing layer converts the radiation into heat which increases the temperature of the bolometer body. As a consequence, the thermistor resistance is modifed. A read-out circuit then converts the resistance value into temperature.

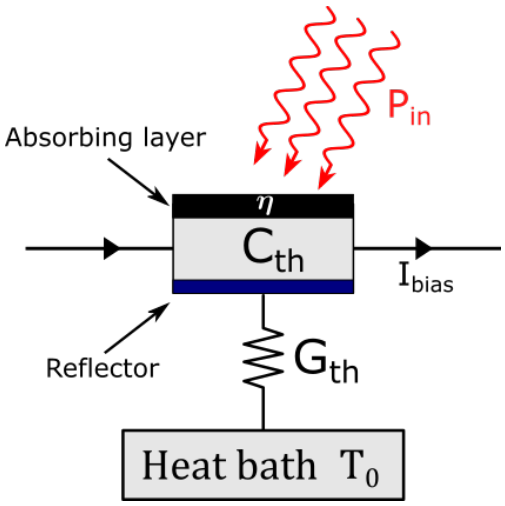

Figure 2.8: Thermal model of a resistive bolometer. η represents the absorption efficiency of the cap layer. C_{th} is the heat capacity of the bolometer body. G_{th} corresponds to the thermal conductance between the bolometer and the heat bath.

2.4.1 Heat Balance

The temperature excursion (ΔT) from the equilibrium state (T_0), once the incident radiation (P_{in}) is turned on, is given by the heat balance equation:

$$C_{th}\frac{dT}{dt} = \eta P_{in} - G_{th}(T - T_0) \tag{2.12}$$

where C_{th} is the heat capacity of the bolometer, G_{th} corresponds to the thermal conductance between the bolometer and the heat bath and η is the absorption rate. The solution of Eq. (2.12) is given by

$$T(t) = T_0 + \frac{\eta P_{in}}{G_{th}}(1 - e^{-t/\tau_{th}}) \tag{2.13}$$

Here $\tau_{th} = C_{th}/G_{th}$ is the thermal time constant. The steady-state solution ($t \gg \tau_{th}$) is then

$$T(t \gg \tau_{th}) - T_0 = \Delta T = \frac{\eta P_{in}}{G_{th}} \tag{2.14}$$

Note that for a given P_{in}, the thermal conductance (G_{th}) has to be minimized and the absorption rate η maximized in order the increase the temperature excursion (ΔT).

2.4.2 Responsivity

The responsivity of a current-biased bolometer is given as the change on the output voltage V_{out} with respect to the variation on the incident power (P_{in}). Writing the output voltage (V_{out}) as

$$V_s = I_{bias} R_{cell} \alpha \Delta T \tag{2.15}$$

I_{bias} is the bias current, R_{cell} corresponds to the bolometer resistance and α is the temperature coefficient of resistance (TCR). Inserting Eq. (2.14) in Eq. (2.15) and ignoring the self-heating due to biasing, the responsivity writes

$$\mathcal{R} = \frac{\eta I_{bias} \alpha R_{cell}}{G_{th}} \tag{2.16}$$

2.4.3 Noise Equivalent Power

Noise performance is one of the important characteristics used for comparing different bolometer designs. The corresponding figure of merit is called the noise equivalent power (NEP) which is defined as the incident signal power (P_{in}) required to obtain a signal equal to the total noise (P_N) in a one Hz bandwidth ($SNR = 1$) [138]. It is given by

$$NEP^2 = \frac{P_N^2}{\mathcal{R}^2} \qquad [\mathrm{W}^2/\mathrm{Hz}] \tag{2.17}$$

where $\mathcal{R}$ is the bolometer responsivity. Generally, NEP can be broken down to

$$NEP^2 = (NEP)^2_{photon} + (4k_B TR + 4k_B T^2 G_{th}/\eta^2)/\mathcal{R}^2 \tag{2.18}$$

where the terms on the right hand side stem from the photon noise, the Johnson-Nyquist noise and the fundamental temperature fluctuations, respectively [138].

2.4.4 Micro - nano bolometers

Microbolometers form a subgroup of bolometers designed for the field of infrared imaging. A typical microbolometer consists of an array of thermal detector cells (pixels) which are patterned to form air bridges on a single wafer (Fig. 2.9). On the material aspect, the detecting material is selected based on the main parameters such as $1/f$ noise and the temperature coefficient of resistance (TCR) which determines the bolometer responsivity. The state of the art of uncooled microbolometers feature $NEP \sim 100\,\mathrm{pW}/\sqrt{\mathrm{Hz}}$. The

most commonly used materials are amorphous/polycryistalline silicon [139] and vanadium oxide (VOx) [140]. Despite having moderate TCR ($2\% - 4\%$) [141], both materials have the advantage of being CMOS-compatible which allows the integration of the bolometers with the read-out circuit, often via flip chip bonding. On the application side, a great majority of microbolometers finds use in the civil/defense applications and operate at ambient temperature whereas astronomy and space projects require cooling down to sub-K temperature for an increased sensitivity.

Over the past decades, the desire for increased sensitivity in the fields such as microwave photon detection [142] and the dark matter experiments [143] brought the bolometers down to the nanoscale. Nanobolometers combine hybrid junctions and the cryogenic temperatures to reach impressive noise levels as low as $NEP \sim 50$ zW / $\sqrt{\text{Hz}}$. The state-of-the-art nanobolometers reported in [137, 144], uses S-graphene-S and SNS junctions as the absorber (Fig. 2.10). In a similar manner to the microbolometers where the absorbing layer is thermally isolated from the heat sink by suspending legs, here the nanobolometers use the weak thermal coupling between the electrons and phonons of a bulk metal and graphene layer at sub-K temperatures for thermal isolation. The electrons absorb the incident radiation whereas the phonons play the role of the heat sink.

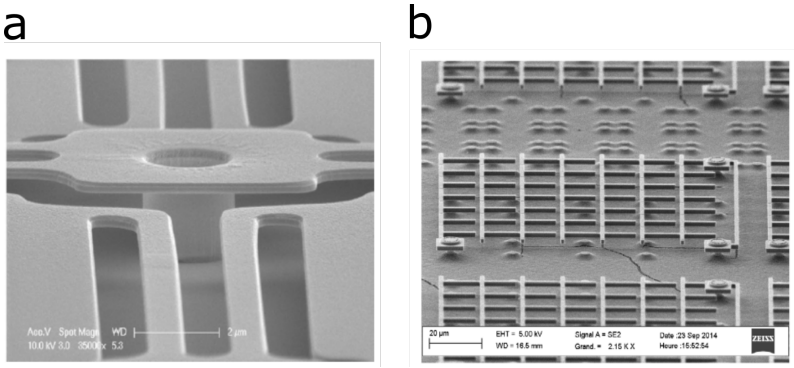

Figure 2.9: SEM image of ***a.*** *the Si-based microbolometer pixel operating at T_{room} [145]* ***b.*** *The cooled Si-based microbolometer for sub-mm detection [146].*

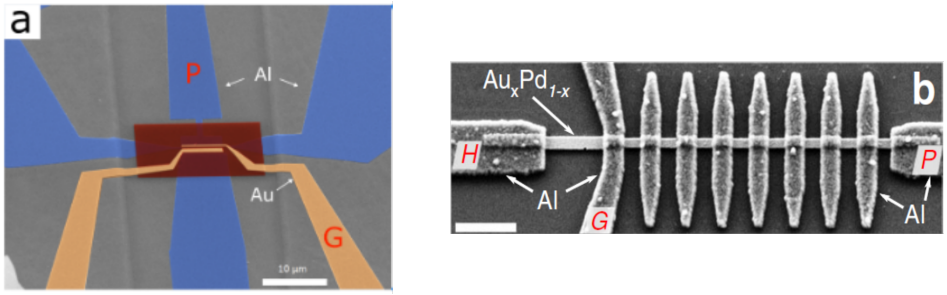

Figure 2.10: ***a.*** *False-colour SEM image of the superconductor-graphene-superconductor bolometer.The graphene patch is located below the gate insulator layer marked in red. [137]* ***b.*** *Micrograph of the SNS boloeter. P,G and H stand for probe, gate and the heater electrodes, respectively [144].*

2.4.5 Characterization of Ti/TiN absorber samples for a sub-millimeter wave bolometer

Within the framework of a collaboration with Thermal and Terahertz Imagery Laboratory (LI2T) of CEA-LETI, we realised the characterization of Ti/TiN absorber layers [147] to be used in the pixels of a cooled Si microbolometer array designed to operate at the 350 µm wavelength [146, 148]. Here, the advantage of using a superconducting material as the absorber is its reduced heat capacity. The work consisted of investigating the key parameters of the absorbing layer samples for the absorption optimization. Namely, these are 1) the critical temperature (T_c) of the deposited Ti/TiN layer (2) the effect of the perpendicular magnetic field on T_c and (3) the residual resistivity ratio (RRR) which is the ratio between the resistances at T_{room} and $T \gtrapprox T_c$. A batch of samples varying in the relative thicknesses of Ti/TiN and the thermal treatment are connected in four-wire scheme and measured between $1.8\,\mathrm{K} < T < 300\,\mathrm{K}$. The results are shown in (Fig. 2.11)

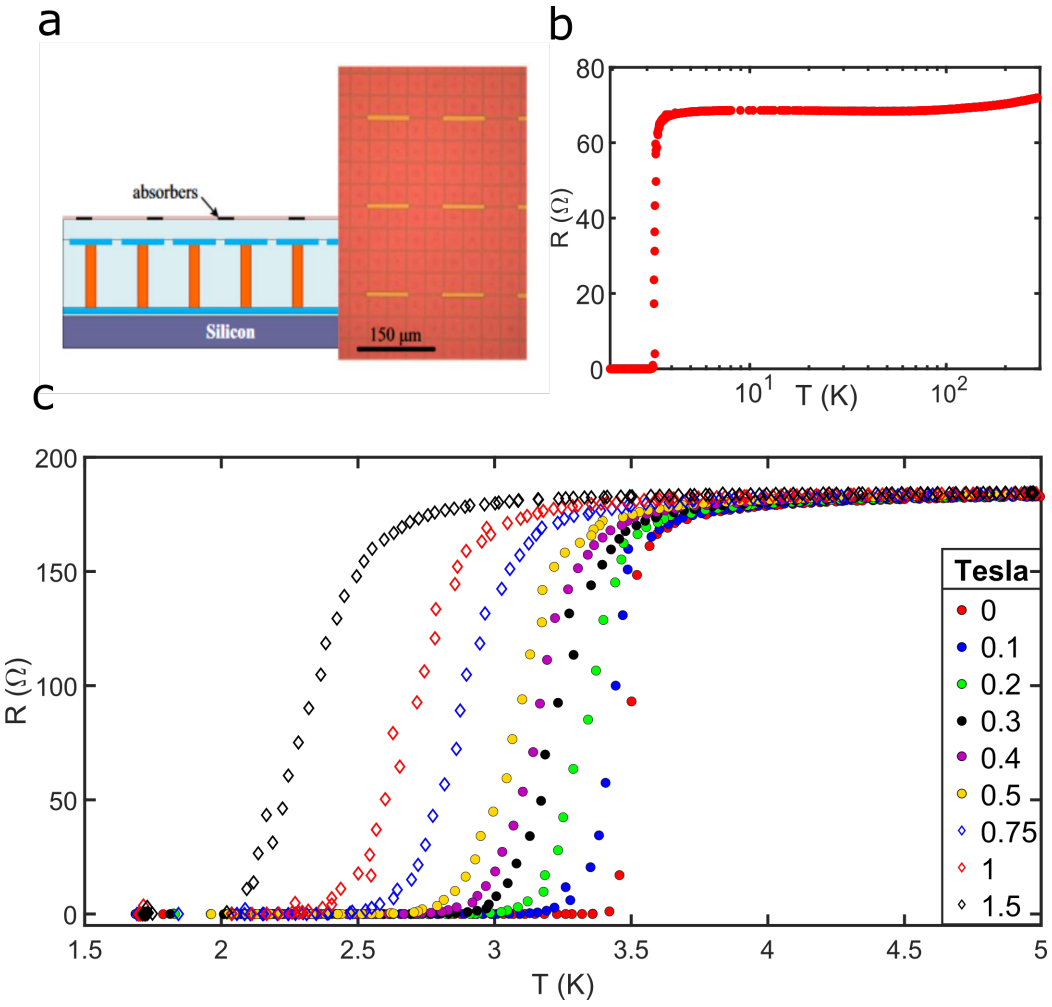

Figure 2.11: ***a.*** *The schematic and the top view photograph of the sensor prototype* ***b.*** *R(T) measurement of the first sample between* $1.8\,\mathrm{K} < T < 292\,\mathrm{K}$. *RRR is found* $\sim$ *1.06* ***c.*** *Determination of* T_c *under increasing perpendicular magnetic field for the second sample. At* $B = 0$ *Tesla,* $T_c \approx 3.5$ K

2.5 Calorimeter

Calorimeters are very similar to the bolometers in terms of operating principle. An incident signal is absorbed by the detector and converted to a change in temperature. The difference is that instead of continuous radiation, a calorimeter captures a quantum of energy in a time-resolved manner (Fig. 2.12). Recently, nanocalorimeter designs for studying quantum thermodynamics have been proposed [107, 108]. Moreover, promising devices for detecting single tunneling quasiparticles, [149] and microwave photons [3, 6, 150–152] have been proposed and demonstrated. Here, the ultimate goal is to use nanocalorimeters for the single microwave photon detection of the qubit states where 1 GHz $<$ f $<$ 10 GHz corresponds to the typical frequency of readout transmons. A 10 GHz photon has $E \approx 41$ μeV. Reaching μeV level sensitivity stays as the next major milestone for the field.

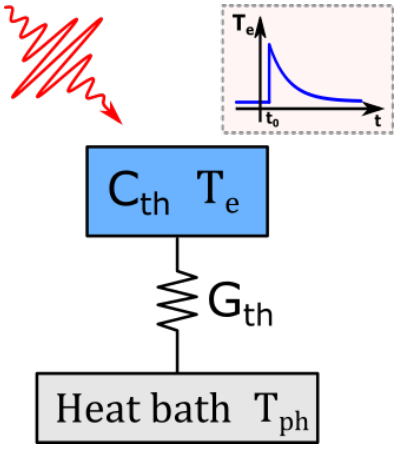

Figure 2.12: Thermal model of a calorimeter. The incident quantum of energy is absorbed at time t_0 by the electrons. T_e sees a sudden rise, then relaxes back to the equilibrium state.

2.5.1 Thermal model of SNS calorimeters

In our experiments, we are going to make use of hybrid structures including SNS Josephson junction and N′IS proximity thermometer. In the case of fast real time measurements, the normal part (N) of these devices will serve as the calorimeter absorber. Here, we detail the underlying thermal model of the SNS Junction which enables the absorber role for the normal metal.

Specific heat: The electron gas and the lattice vibrations are the two degrees of freedom to which energy can be transferred in an ordinary metal [153]. Therefore, the specific heat ($c = \partial E/\partial T$) consists of a lattice (c_L) and an electronic (c_e) term. The lattice contribution is given by the Debye model which associates a critical temperature ($T_\mathcal{D} \approx \hbar\omega_D/k_B$) with the highest-energy phonon ($\hbar\omega_D$) in the lattice. For $T \ll T_\mathcal{D}$, the lattice specific heat takes the approximate form $c_L \approx 2.4\pi^4 N k_B (T/T_\mathcal{D})^3$ where N is the number of states per unit volume. The electronic specific heat stems from the partially filled states of

conduction electrons in the energy window $\sim k_B T$ around the Fermi level (E_F). It is given as $c_e = \gamma T$ where $\gamma = \pi^2 N(E_F) k_B^2/3$ is a material-dependent constant. Due to the T^3 dependence, c_l is greatly suppressed at $T \ll T_{\mathcal{D}}/10$ and c_e becomes the dominant term. In our experiments, we use copper as the normal metal. The fact that $T_{\mathcal{D}}^{Cu} = 343$ K and our devices are thermalised at $T_{bath} = 50$ mK, therefore allows us to ignore c_l in our calculations.

Electron - phonon coupling: An important characteristic of metals at sub-Kelvin temperatures is the weak electron-phonon scattering rates. Due to this low interaction, the normal metal can be considered as an ensemble of the electronic gas and the phonon system coupled to each other, both having a well defined temperature ($T_{e,ph}$) in the steady state. The electron-phonon energy exchange rate in ordinary metals is given by [154]

$$\dot{Q}_{e-ph} = \Sigma \mathcal{V}(T_e^n - T_{ph}^n) \quad [W] \tag{2.19}$$

where Σ is the material dependent constant ($\Sigma_{Cu} \approx 2 \times 10^8$ W/m^{3}K$^{n=5}$) [116, 155] and $\mathcal{V}$ is the metal volume. In Eq. (2.19), $n = 5$ is frequently used for ordinary metals whereas in disordered systems, a weaker coupling ($\dot{Q}_{e-ph} \propto T^6$) was predicted [156] and observed in materials such as heavily doped Si [157] and thin films of Ti and Hf [158].

The role of proximity effect on the electron-phonon coupling In Chapter-1, we discussed the role of the proximity effect on the transport properties of a normal metal in clean contact with a superconductor. It turns out that the electron-phonon interaction is also affected by the same phennomenon and become phase tunable. [44, 159]. In the long regime with zero phase bias ($\varphi = 0$), the thermal power is given as

$$\dot{Q}_{e-ph} = \dot{Q}_{e-ph}^N e^{-T^*/T} \tag{2.20}$$

where $T^* = cE_{Th}K_B$ and c is the scaling factor corresponding to the proximity variations (c $\approx$ 3.5) [44]. This effect becomes important at $E_{Th} \gg k_B T$ which in our case corresponds to T $\ll T_{bath} = 50$ mK. We therefore neglect the impact of the proximity effect on the thermal properties of the N absorber in our experiments.

Thermal boundary resistance: Phonons obey Bose-Einstein statistics. At a given T, the average phonon number $\langle n \rangle$ in the bulk features a thermal cutoff frequency ($\omega_T = \frac{k_B T}{\hbar}$) beyond which $\langle n \rangle$ becomes negligible. At very low temperatures ($T \ll T_{\mathcal{D}}$), it suffices to consider only the acoustic phonon branch and assume a linear dispersion relation ($\omega = kv$) where v is the material-dependent sound velocity. Reformulating the thermal cutoff condition in terms of wavelength ($\lambda_T = \frac{hv}{k_B T}$), it is seen that only the phonons with $\lambda > \lambda_T$ are present in the bulk. For copper ($v = 4.7 \times 10^3$ m/s) at 100 mK, λ_T amounts to $\sim$ 2.25 µm which is much larger than the normal metal thickness ($t \sim 35$ nm). The fact that phonons are not confined to N therefore allows us to assume N in perfect thermal contact with the substrate ($T_{ph} = T_{subs}$). Under certain configurations such as suspending nanowires [160, 161] and thin dielectric membranes [162, 163], the above mentioned assumption does not hold. A thermal bottleneck emerges between the

different phonon groups such that T_{ph} can be driven to $T_{ph} > T_{subs}$ or cooled down to $T_{ph} < T_{subs}$ via electrons [164, 165]. In such cases, the energy exchange between the two phonon groups has to be taken into account. It is given by the Kapitza coupling [166] as

$$P_K(T_{ph}, T_{subs}) = KA(T_{ph}^4 - T_{subs}^4) \quad [W] \tag{2.21}$$

where K is the material specific Kapitza constant and A is the interface area.
Thermal leakage via S-N interface Due to the gap (2Δ) in the quasiparticle density of states, superconductors are known to display poor thermal conductivity. For a given metal, the ratio r between the superconducting and normal state thermal conductivities ($G_{S,N}$) writes [128]

$$r(T) = \frac{3}{2\pi^2} \int_{\Delta/k_BT}^{+\infty} \Big(\frac{x}{\cosh(x/2)}\Big)^2 dx \tag{2.22}$$

At very low temperatures ($k_BT \ll 2\Delta$), $\cosh\big(\frac{1}{2}x\big) \approx \frac{1}{2}e^{\frac{1}{2}x}$ and Eq. (2.22) can be shown to have the approximate form [167]

$$r(T) \approx \frac{6}{\pi^2}\Big(\frac{\Delta(T=0)}{k_BT}\Big)^2 e^{-\frac{\Delta(T=0)}{k_BT}} \tag{2.23}$$

As shown in Ref. [128], we can therefore calculate the power flow through one superconducting leads as

$$P(T_e) = L_0 G_N^{sc} \int_{T_{bath}}^{T_e} r(T) T dT \qquad [W] \tag{2.24}$$

where $L_0 = 2.45 \times 10^{-8}\, W\Omega/K^2$ is the Lorentz number and G_N^{sc} is the normal state conductance of the superconducting lead under consideration. Given the $\sim exp(-\Delta/k_BT)$ dependence of r(T), at $k_bT \ll \Delta$ the superconductor becomes a very poor thermal conductor which allows us to consider N island as thermally isolated from its environment.

2.5.2 Fundamental fluctuations

A body which is in thermal contact with a heat reservoir keeps exchanging energy with the reservoir even at equilibrium. The entire thermodynamic system undergoes continual random transitions among its microstates which causes its properties to deviate momentarily from their mean values [109]. We can therefore attribute statistical properties to the observables of the system. Likewise, the electron gas of the absorber permanently exchanges energy with the phonons of the calorimeter absorber. Hence, the electronic temperature (T_e) are subject to fluctuations which is given by the fluctuation-dissipation theorem as [149]

$$\langle \delta T_e(t) \delta T_e(t') \rangle = \frac{k_B T_{bath}^2}{C} e^{-|t-t'|/\tau} \tag{2.25}$$

which sets the ultimate limit for sensitivity. A calorimeter has to fulfill the condition $\delta T_e \gg \sqrt{\delta T_e(t)}$ in order to have a meaningful readout (Fig. 2.13).

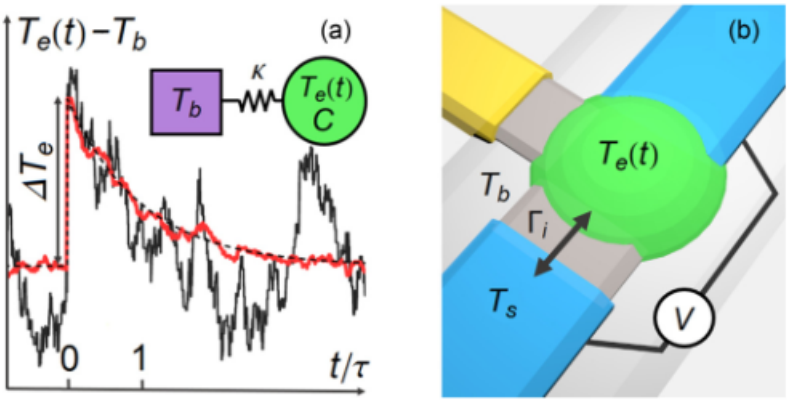

Figure 2.13: ***a.*** *Monte Carlo simulated time traces of a calorimeter response for a* $200\mu eV$ *impinging energy with* $T_b = 5$ *mK (red) and* $T_b = 30$ *mK (black). [149]* ***b.*** *Schematic of the proposed nanoscale injector-calorimeter setup: A normal metallic island (green) contains a thermalized electron gas, with fluctuating temperature* $T_e(t)$*, constituting the absorber. The island is well coupled to an electrically grounded superconductor (upper, blue) acting as a heat mirror. It is further tunnel coupled to another superconductor (lower, blue), kept at a temperature* T_s *and biased at a voltage* V*, serving as a particle source with tunable injection rate* $\Gamma_i(Ts, V)$*. A thermometer, coupled to the island, is also shown (yellow). (taken from [149])*

Chapter 3

Radio-frequency Thermometry

3.1 Introduction

This chapter is built around the concept of resonant electric circuits and how we exploit the resonance for the purposes of fast thermometry. We begin our discussion by visiting the fundamental LC tank circuit, the internal losses of an oscillator and how an oscillation is sustained in the presence of an external drive. Then, we overview the key concepts of quality factor and bandwidth. In section 4, we discuss the use of scattering parameters for analyzing the circuits in the microwave domain, the readout schemes based on S_{21} and S_{11} parameters and the in-phase/quadrature mixing for power measurements. The last two sections are dedicated to the details of our on-chip superconducting microwave resonator and the related fast readout experiment where we measured the instability in an SNS junction biased near I_c.

3.2 LC Oscillator

Let us begin our discussion with the circuit shown in Fig. 3.1a. We consider that at a time $t < t_0$, the switch S_1 has been on for a long time such that the capacitor (C_1) is fully charged by the DC voltage source (V_1). The switch S_2 is off and therefore the inductor (L_1) is disconnected from the circuit. At time $t = t_0$, we simultaneously reverse the switches state (S_1: off and S_2: on) such that C_1 and L_1 now form a closed circuit and V_1 supply is cut off (Fig. 3.1b). What happens next is that C_1 starts to discharge over L_1 which develops a counter electromotive force according to its fundamental relation ($V = L_1 dI/dt$). Once the C_1 is fully discharged, the voltage with the opposite sign develops and leads to a reverse current which recharges the capacitor. Hence, the total energy of the system constantly oscillates between the capacitor and the inductor. The equation which governs the oscillatory behaviour of the system can be easily obtained by applying Kirchoff's law on the voltage loops or the current nodes. In the differential form,

it is given by

$$\frac{d^2I(t)}{dt^2} + \frac{1}{L_1C_1}I(t) = 0 \tag{3.1}$$

proposing a complex exponential ($I(t) = Ae^{-i\omega_0 t} + Be^{+i\omega_0 t}$) as a solution. The system oscillates with the frequency

$$f_0 = \frac{1}{2\pi\sqrt{L_1C_1}} = \frac{\omega}{2\pi} \tag{3.2}$$

where f_0 is called the natural frequency of the system.

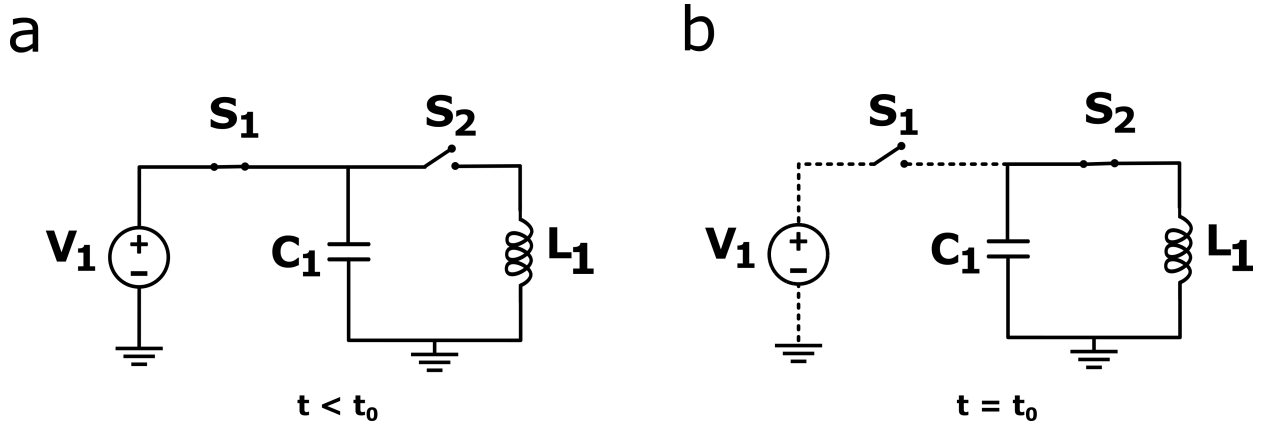

Figure 3.1: The circuit diagram of the LC oscillator tank circuit corresponding to ***a.*** *the initial state where S_1 is on and S_2 is off. C_1 is fully charged by V_1* ***b.*** *the final state where S_1 is off and S_2 is on. V_1 is disconnected from the LC tank.*

3.2.1 Internal losses and damping

In the previous section, we saw that once the initial conditions are set, an ideal LC tank circuit oscillates incessantly. However, in real world, even the most stringent circuit elements feature some finite resistance which eventually brings the oscillation amplitude down to zero (Fig. 3.2a). The losses in an oscillating system are taken into account by the dimensionless parameter called the damping ratio (ζ). The damping ratio plays an important role in the transient response of the system. Writing the characteristic equation of an RLC oscillator

$$\frac{d^2I(t)}{dt^2} + 2\omega_0\zeta\frac{dI(t)}{dt} + \omega_0^2 I(t) = 0 \tag{3.3}$$

it can be shown that the system has three distinct transient response types based on the value of ζ (Fig. 3.2b):

$$I(t) = \begin{cases} A_1 e^{-\omega_0\zeta t}\cos\left(\omega_0\sqrt{1-\zeta^2}t\right) & \zeta < 1 \ \ (\text{under}-\text{damped}) \\ B_1 t e^{-\zeta\omega_0 t} & \zeta = 1 \ \ (\text{critically damped}) \\ C_1 e^{-\omega_0(\zeta+\sqrt{\zeta^2-1})t} & \zeta > 1 \ \ (\text{over}-\text{damped}) \end{cases} \tag{3.4}$$

The damping factor ζ is related to the circuit parameters as $\zeta = R/2\sqrt{C/L}$ and $\zeta = 1/2R\sqrt{L/C}$ in the series and parallel RLC circuits, respectively.

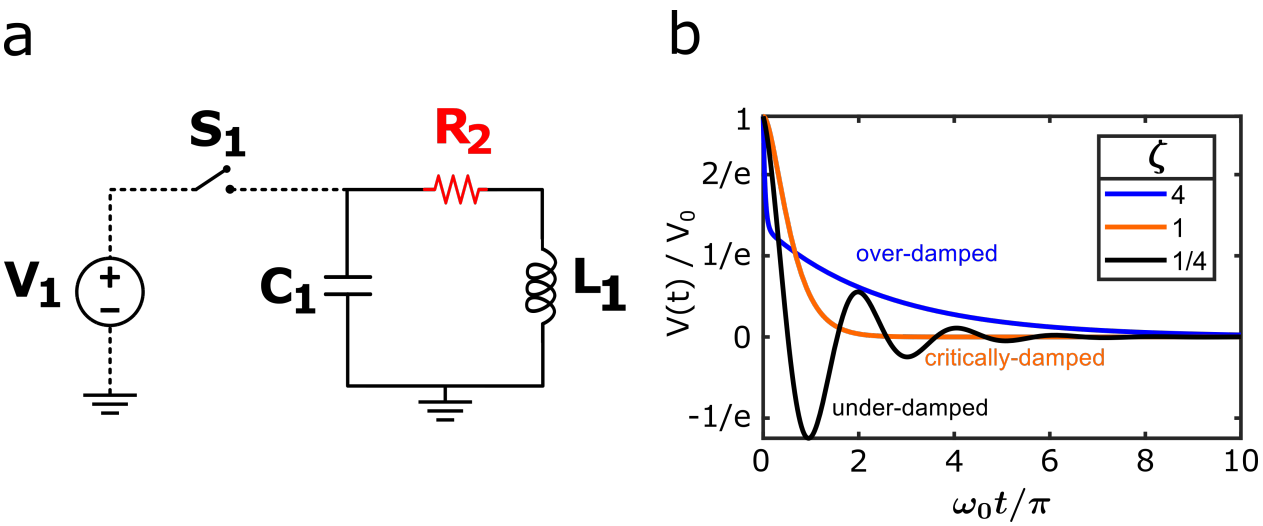

Figure 3.2: ***a.*** *The circuit diagram of the LC oscillator tank circuit with the switch S_2 represented by its internal resistance R_2* ***b.*** *The calculated transient responses corresponding to the over-damped (blue), critically damped (orange) and the under-damped (black) cases.*

3.3 Driven damped harmonic oscillator

When a sustained oscillation is desired in a lossy oscillator, an external drive has to feed the system continuously to compensate for the losses. For an RLC circuit, this is achieved by connecting an AC source to the circuit. The equation of motion for a a second order system with a sinusoidal source ($I_0 \sin \omega_s t$) is given by

$$\frac{d^2I(t)}{dt^2} + 2\omega_0\zeta\frac{dI(t)}{dt} + \omega_0^2 I(t) = \omega_0^2 I_0 \sin(\omega_s t) \tag{3.5}$$

Taking the Laplace transform of Eq. (3.5), it can be shown that the frequency response of the system writes

$$H(jw) = \frac{\omega_0^2}{(j\omega)^2 + 2\zeta\omega_0(j\omega) + \omega_0^2} \tag{3.6}$$

In Fig. 3.3, we trace $|H(jw)|$ for various damping ratios. It is seen from the figure that the underdamped systems ($\zeta < 1$), are in resonance when the system is driven at $\omega \approx \omega_0$. The resonating frequency ω_r is slightly detuned from the system's natural frequency ω_0 and obeys $\omega_r = \omega_0\sqrt{1-\zeta^2}$. Hence, at $\zeta \ll 1$, ω_r converges to ω_0.

The most commonly used arrangements among numerous RLC topologies are when the three circuit elements are connected in 1) series and 2) parallel (Fig. 3.4). At resonance, the series and the parallel RLC circuits behave in a conjugate manner. The fact that RLC circuits contain reactive circuit elements gives frequency dependence to the total impedance $\mathrm{Z}(\omega) = \mathrm{R} + \mathrm{iX}(\omega)$. In the series RLC configuration, the reactances $X_L(\omega)$ and $X_C(\omega)$ cancel out at $\omega = \omega_0$ and $Z(\omega)$ is reduced to $\min(Z(w)) = R$. Hence, the circuit is in phase with source and draws maximum power from it. The parallel RLC is very similar to the series configuration in terms of resonant frequency. However, this time, the imaginary part of the admittances ($B_{C,L}$) cancel each other out such that only

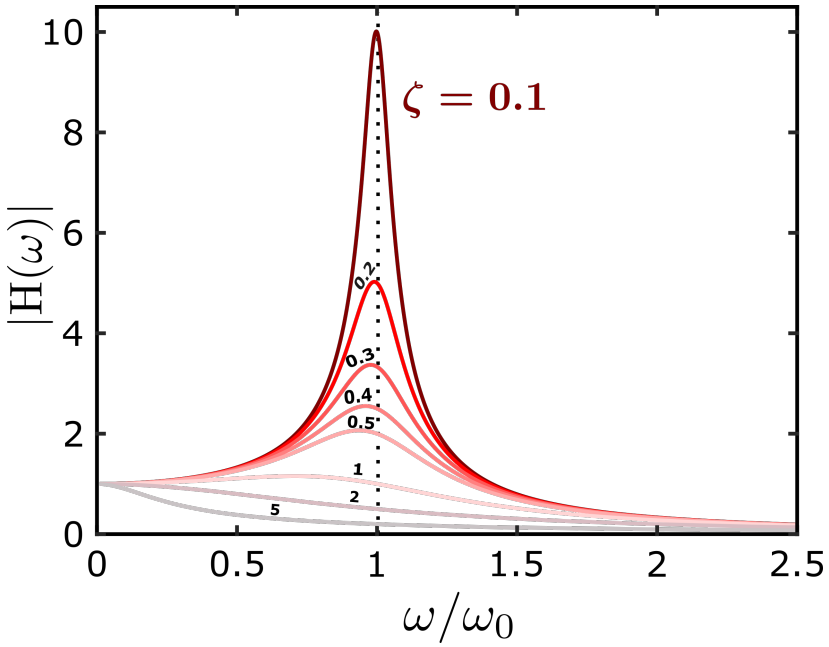

Figure 3.3: The calculated frequency response of a driven damped harmonic oscillator as a function the damping ratio ζ

$Y(w) = G$ is seen by the source. Therefore, LC branches act as an open circuit and the total impedance is maximized. As a consequence, the parallel RLC circuit draws minimum current from the source at resonance. In the following sections, we are going to discuss how the parallel RLC configuration is used for a fast readout scheme of the electronic temperature of the proximised normal metal (N').

3.3.1 Quality factor and bandwidth

An important system parameter which measures the level of damping in a driven oscillator is the quality factor (Q). Basically, it is the ratio of the energy stored by the resonator over the dissipation per cycle

$$Q = 2\pi \frac{\text{energy stored}}{\text{dissipation per cycle}} \tag{3.7}$$

Another interpretation is the ratio of the exponential decay constant τ over the oscillation period T. The above-mentioned parameters and the system's natural frequency are related to each other as

$$Q = \frac{1}{2\zeta} = \frac{\tau\omega_0}{2} \tag{3.8}$$

Therefore, high quality factor means longer sustain of the oscillatory behaviour in a transient regime. An alternative definition of the quality factor relates the resonance frequency (f_r) to the bandwidth. Hence, the quality factor is defined as

$$Q = \frac{f_r}{\Delta f} \tag{3.9}$$

where Δf corresponds to the full width at half maximum.

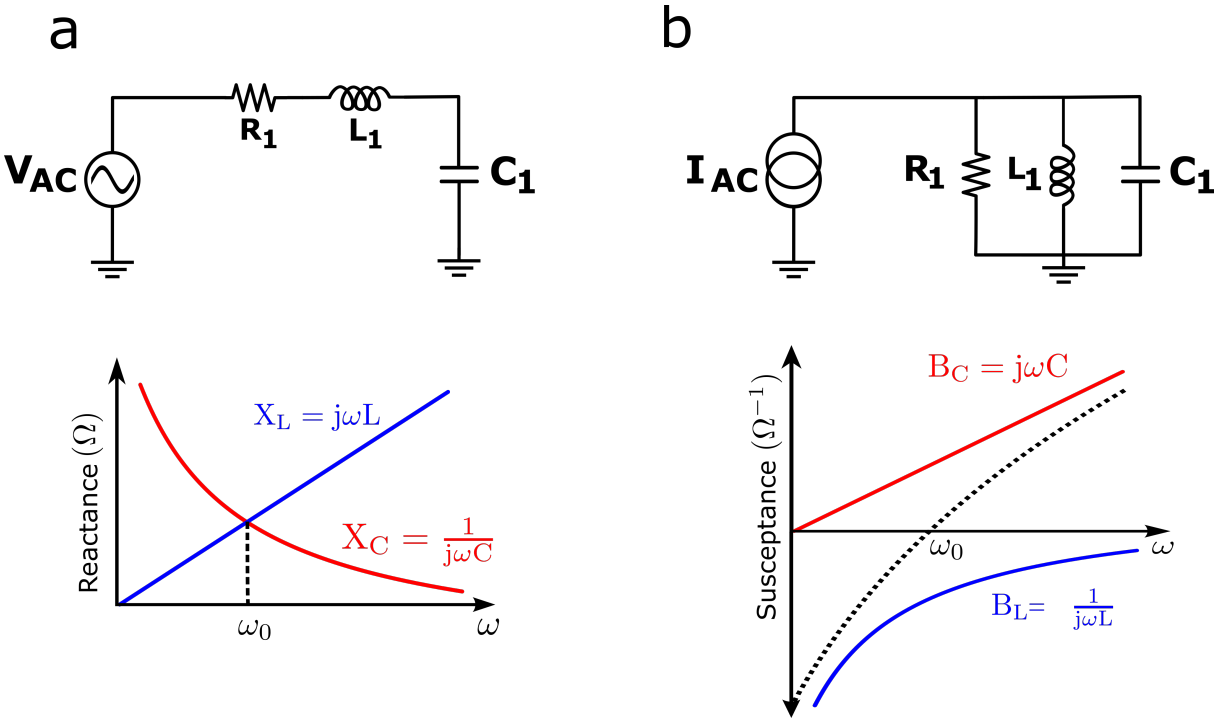

Figure 3.4: The most commonly used RLC circuit topologies ***a.*** *series RLC* ***b.*** *parallel RLC. The graphs below each circuit diagram demonstrates when the resonance condition is met.*

3.4 Microwave concepts

The analysis of circuits operating at microwave frequencies (1 GHz - 1 THz) cannot be done with the classical methods based on the mesh analysis. This stems from the fact that in the microwave range, the signal wavelengths become comparable to the physical dimensions of the circuit such that significant phase shifts may occur between nodes. As the lumped element approach is no more valid, a set of analysis tools based on the incident/reflected waves from an N-port network is used. In what follows, we present a quick review of the scattering parameters and the main readout schemes used in the mesoscopic experiments including microwave signals.

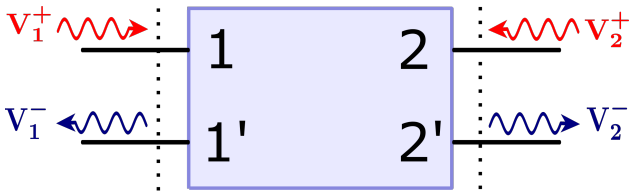

Figure 3.5: A two-port network depicted as a black box. The incident (reflected) voltage waves are denoted as V_i^+ (V_i^-) where the subscript corresponds to the port number. The dashed lines represent the reference planes.

3.4.1 S parameters

For an N-port network, we can define an impedance (admittance) matrix relating the voltages and the currents seen at the terminal planes which in principle suffices to completely describe the network's behaviour. However, from the experimental point of view, it is more practical to work with the incident/reflected voltage waves from the network rather than the voltages defined at the terminal planes (Fig. 3.5). This way, the experimentalist can connect a vector network analyzer to the system and characterize it in terms of scattering parameters. The scattering matrix for a 2-port system is defined as

$$\begin{bmatrix} V_1^- \\ V_2^- \end{bmatrix} = \begin{bmatrix} S_{11} & S_{12} \\ S_{21} & S_{22} \end{bmatrix} \begin{bmatrix} V_1^+ \\ V_2^+ \end{bmatrix} \tag{3.10}$$

To find the S-parameters at a specific port, the other ports have to terminated with a matched load to prevent reflection. Hence, the reflection at port-1 can be found as

$$S_{11} = \left. \frac{V_1^-}{V_1^+} \right|_{V_2^+=0} \tag{3.11}$$

Similarly, the transmission from the port-1 to port-2 is written as

$$S_{21} = \left. \frac{V_2^-}{V_1^+} \right|_{V_2^+=0} \tag{3.12}$$

3.4.2 Readout schemes with S_{11} and S_{21}

S_{11} and S_{21} parameters are frequently used in mesoscopic experiments to probe the properties of a given sample. A generic setup consists of a wave generator sending a sine tone at the resonant frequency of the system, a low noise amplifier to amplify the reflected/transmitted signal, a network analyzer which receives the output signal (Fig. 3.6). Depending on the configuration, a circulator (or a directional coupler) either redirects the reflected power to the VNA port or in the transmitted case serves as an isolator to prevent reflections from the output. Both configurations make use of the coupling capacitors as a means to filter the low filter noise and to block DC.

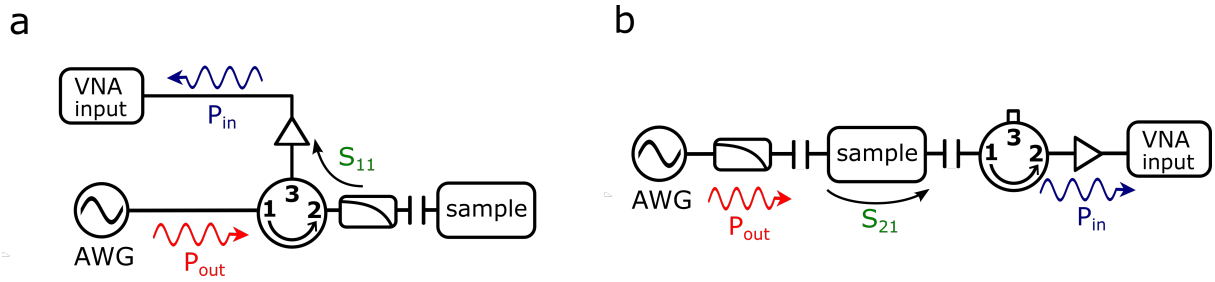

Figure 3.6: The diagrams of typical measurement setups configured for ***a.*** *reflectometry* ***b.*** *transmittance measurements*

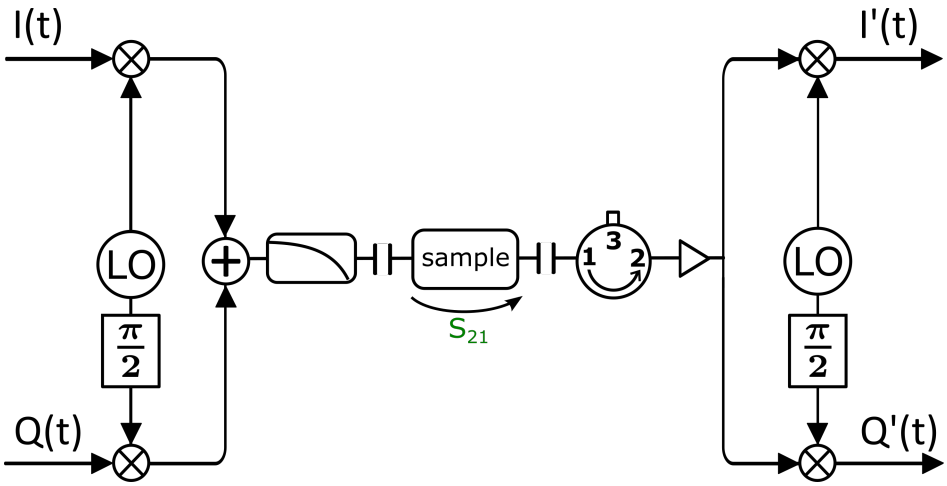

Figure 3.7: I-Q modulation and demodulation diagram used in a setup configured for measuring S_{21}

3.4.3 I-Q mixing and power measurement

The term I-Q stands for 'in-phase' and 'quadrature' signals which are out of phase by $\Phi = \pi/2$. The idea behind the I-Q modulation is simple. The sum of any pair of quadrature signals of type $I(t)\cos(\omega t)$ and $Q(t)\sin(\omega t)$ allows both the amplitude and the phase modulation. In case $I(t)$ and $Q(t)$ are fixed to the same amplitude ($I(t) = Q(t)$), it can be shown via trigonometric identities that the sum yields

$$\begin{aligned} I(t)\cos(\omega t) + Q(t)\sin(\omega t) &= I(t)(\cos(\omega t) + \sin(\omega t)) \\ &= \sqrt{2}I(t)\cos(\omega t - \pi/4) \end{aligned} \tag{3.13}$$

Therefore, I(t) can be used to modulate the amplitude of the signal generated by the local oscillator (LO). Similarly, it is possible to modulate the phase of the output signal by setting different values on $I(t)$ and $Q(t)$. For example, a binary set of $(I, Q) = \{-1, 1\}$ results in an output signal with four possible phase bias $\Phi = \{\pi/2, -\pi/2, 3\pi/4, -3\pi/4\}$ which is commonly used digital modulation technique [168].

Power measurement

So far, we explained the basic principles of I-Q signals and how amplitude and phase modulation can be realized with them. In our experiments, we drive our system at the resonant frequency and read the transmitted power (Fig. 3.7). Therefore, rather than the modulation, we are interested in the generation and the detection of a sinusoidal tone via I-Q signals. In a typical I-Q modulation and demodulation scheme, when the user specifies a sine tone with a given amplitude and frequency ($\mathrm{V_{out}}\sin(\omega_0 \mathrm{t})$), the hardware does two things: 1) it sets the LO frequency accordingly 2) selects I - Q values such that $\mathrm{V_{out}} = \sqrt{\mathrm{I}^2 + \mathrm{Q}^2}$ corresponds to the specified signal amplitude (Fig. 3.8). The generated signal then goes through various operations along the transmission line. A portion of it gets transmitted ($S_{21}V_{out}\cos(\omega_0 t + \phi)$) from the sample and reaches the receiver input.

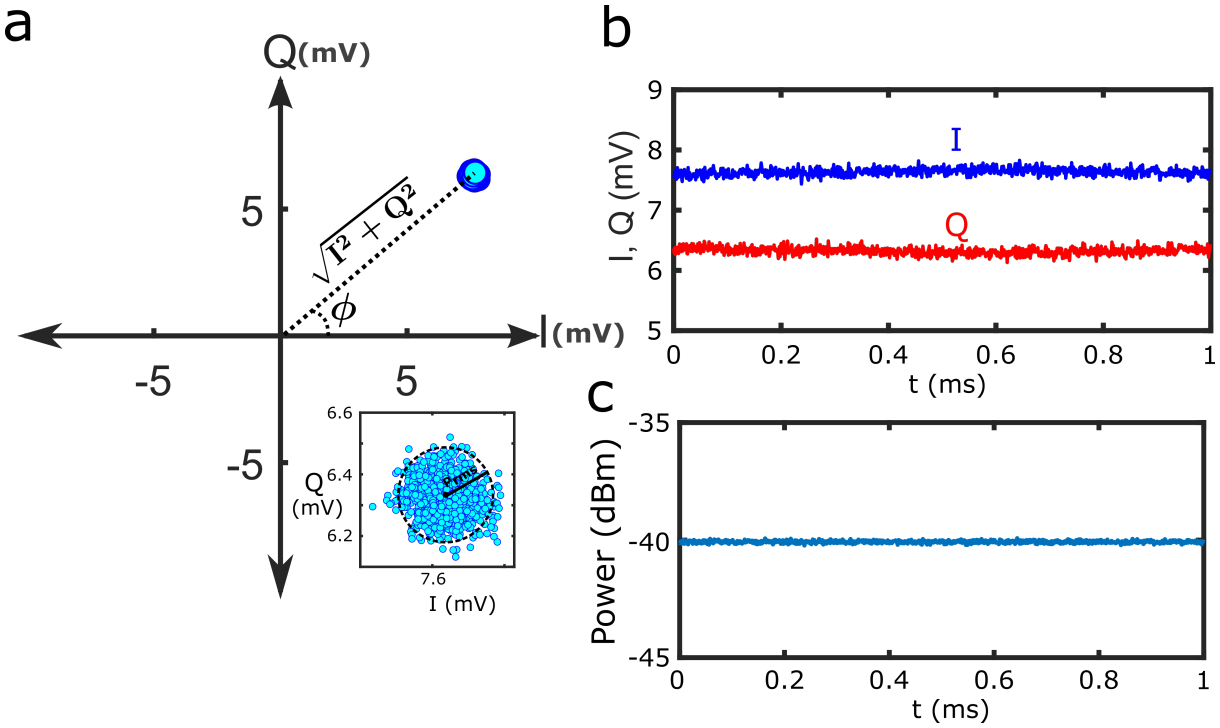

Figure 3.8: A test measurement where the AWG output is directly connected to the VNA input. A sine tone with $\mathrm{P} = -40\,\mathrm{dBm}$ *is played for 1 ms. In* ***a.*** *the measured signal is represented in I-Q plane. The inset shows the spread of the datapoints.* ***b.*** *The I-Q components of the same signal as a function of time* ***c.*** *The total power as a function of time*

A typical demodulation sequence takes place as the following: 1) the input signal is split into two and fed to the multiplication circuits on both branches. The multiplication of $V'_{out}\cos(\omega_0 t + \phi)$ with $\cos(\omega_0 t)$ yields

$$V'_{out}\cos(\omega_0 t + \phi)\cos(\omega_0 t) = \frac{1}{2}V'_{out}\big(\cos(2\omega_0 + \phi) + \cos(\phi)\big) \tag{3.14}$$

Next, filtering the high frequency term, the in-phase component $I'(t)$ of the output signal is obtained as

$$I'(t) = \frac{1}{2}V'_{out}\cos(\phi) \tag{3.15}$$

Similarly, via multiplication with the quadrature term $sin(\omega_0 t)$, $Q'(t)$ is obtained as

$$Q'(t) = \frac{1}{2}V'_{out}\sin(\phi) \tag{3.16}$$

Once the in-phase ($I'(t)$) and the quadrature ($Q'(t)$) terms are obtained, the signal amplitude is simply obtained via $V'(t) = \sqrt{I'(t)^2 + Q'(t)^2}$. In the microwave domain, the signals are often represented in power unit with respect to 1 mW which is given as

$$\mathrm{P}\ (\mathrm{dBm}) = 10\log_{10}\left(\frac{I^2+Q^2}{50\,\Omega}\Big/1\ \mathrm{mW}\right) \tag{3.17}$$

3.5 On-chip superconducting microwave resonator

In our experiment, we embed an SINS junction in an RLC resonant circuit operating at the microwave domain. In this configuration, the tunnel resistance of the SINS junction serves as the resistor of the parallel RLC resonator and we read its temperature dependence via S_{21} parameter of the microwave circuit (Fig. 3.9). This way, the bandwidth problem of the ordinary dc lines which limits the fast temperature readout is overcome. The samples hosting the SINS junction and the resonator are conceived as two stand-alone chips. The resonator operates at $f_r = 575$ MHz and has a large bandwidth (BW = 10 MHz) to allow for a rapid detection of the transmitted amplitude (Fig. 3.11). The initial design is based on the previous works demonstrated in Ref. [6, 169]. As mentioned previously, our microwave setup is configured for transmittance (S_{21}) measurements. Therefore, the resonator is a two-port parallel RLC network hosting two coupling capacitors, C_1 (~ 0.03 pF) and C_2 (~ 0.185 pF), that we implement as interdigited microstrips. In this readout scheme, the resonant frequency is fixed by the inductance, L_1 ($\sim$88 nH) and the total capacitance (C_{tot}) to the ground (Fig. 3.9a). C_{tot} includes a parasitic term C_p ($\sim$0.67 pF) as well as the impact of the coupling capacitors $C_{1,2}$ (Fig. 3.10). The contribution of the coupling capacitors can be obtained from the Norton equivalent of the circuit. Following the development in [170] :

$$C^*_{1,2} = \frac{C_{1,2}}{1 + C^2_{1,2} Z_0^2 w_0^2} \tag{3.18}$$

For $f_0 = 575$ MHz and $Z_0 = 50\ \Omega$, we get $C^*_i \approx C_i$. Therefore, the total capacitance amounts to $C_{tot} = C_1 + C_2 + C_p \approx 0.86$ pF. In Table 3.1, we present the reported values of the circuit elements for the same readout topology. The total quality factor (Q_{tot}) of the resonator is determined by the internal and the external quality factor as

$$\frac{1}{Q_{tot}} = \frac{1}{Q_{int}} + \frac{1}{Q_{ext}} \tag{3.19}$$

where the internal quality factor (Q_{int}) is given by

$$Q_{int} = \frac{R_s}{\omega_0 L} \tag{3.20}$$

Here R_s corresponds to the resistance of the sample. In a similar fashion, the coupling to the transmission line determines the external losses, hence the external quality factor (Q_{ext}):

$$Q_{ext} = \frac{R_{ext}}{\omega_0 L} \tag{3.21}$$

Here, R_{ext} is the transformed impedance of the transmission line seen by the resonator which is given as

$$R_{ext} = \frac{1}{(C_1^2 + C_2^2) Z_0 \omega^2} \tag{3.22}$$

The comparison between the internal and external losses of a resonator, in other words, the comparison between Q_{int} and Q_{ext} places the resonator in one of the three coupling regimes. These are

Ref.	C_1 (fF)	C_2 (fF)	L_1 (nH)	f_0 (MHz)
Bayan et al. [1, 3, 171]	10.3	59.3	100	620
Gasparinetti et al. [6]	100	200	80	625
Viisanen et al. [169]	20	400	-	479
Current experiment	30	185	88	575

Table 3.1: The comparison of the coupling capacitors $C_{1,2}$, the spiral inductor L_1 and the resonant frequency f_0 of the readout circuit with the previous reports.

1. under-coupled ($Q_{int} < Q_{ext}$) ($R_s < R_{ext}$)
2. critically coupled ($Q_{int} = Q_{ext}$) ($R_s = R_{ext}$)
3. over-coupled ($Q_{int} > Q_{ext}$) ($R_s > R_{ext}$)

In the under-coupled case, the internal losses of the resonator are dominant over the losses to the environment. Typically, this regime is preferred whenever long photon lifetimes in the cavity are desired [172]. On the other hand, the Q-factor tunability with the coupling capacitors saturates in this regime [173] and for fast readout measurements, the over-coupled regime is preferred [174, 175]. For the given $C_{1,2}$ and ω_0, we have $R_{ext} \approx 40$ kΩ whereas the N′IS junctions of proximity thermometer often presents a differential resistance $R \approx 100$ kΩ. Therefore, our resonator operates in the overcoupled regime. The transmittance (S_{21}) at resonance is given by [170]

$$S_{21} = -\frac{2C_1C_2R_sZ_0}{LC_{tot} + (C_1^2 + C_2^2)R_sZ_0} = -\frac{\alpha R_s/R_{ext}}{1 + R_s/R_{ext}} \tag{3.23}$$

where $\alpha = \frac{2C_1C_2}{C_1^2+C_2^2}$ is the parameter on the capacitor symmetry.
We use a second inductance with $L_2 \sim$149 nH and a ceramic capacitor on the sampleholder $C_3 \approx 100$ pF to form a bias tee. The resistor $R_1 = 22\,\Omega$ together with an $R_2 = 100$ kΩ at T_{room} form a voltage divider for dc biasing the tunnel junction. As the lumped-element approach is valid at the operating frequency, the inductances are simply implemented as on-chip spirals. We use Al wire micro-bondings between pads to complete the circuit. In the experimental RF frequency range, their contribution to the resonator inductance is not negligible but under control. The transmission spectrum

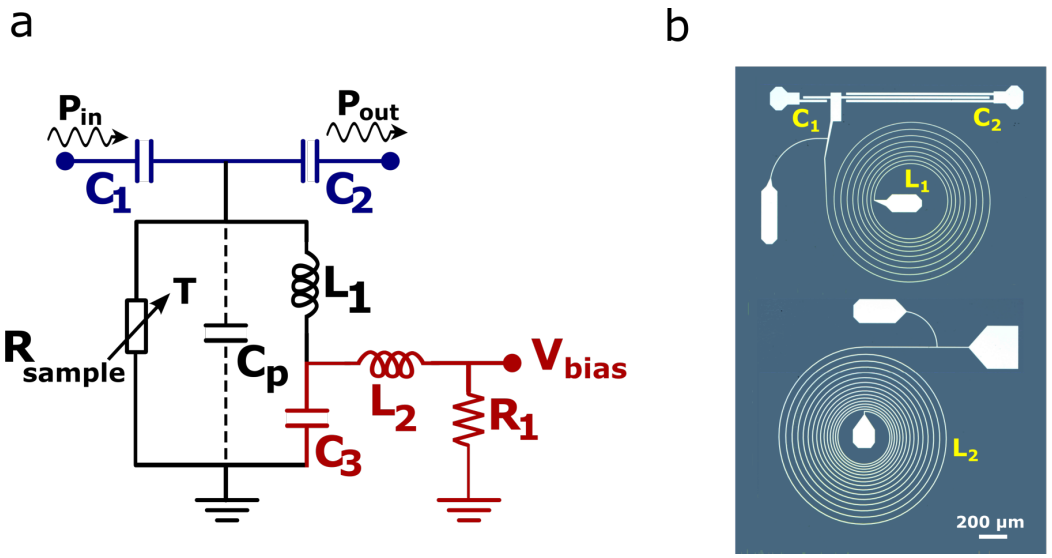

Figure 3.9: ***a.*** *Optical image of the resonator chip. We use a single step laser lithography and 100 nm* ***Al*** *deposition to fabricate the sample. The microstrip coupling capacitors and the spiral inductors are labeled in yellow.* ***b.*** *The circuit diagram of the parallel RLC resonator. The coupling capacitors $C_{1,2}$ are marked in blue, the bias tee in red.*

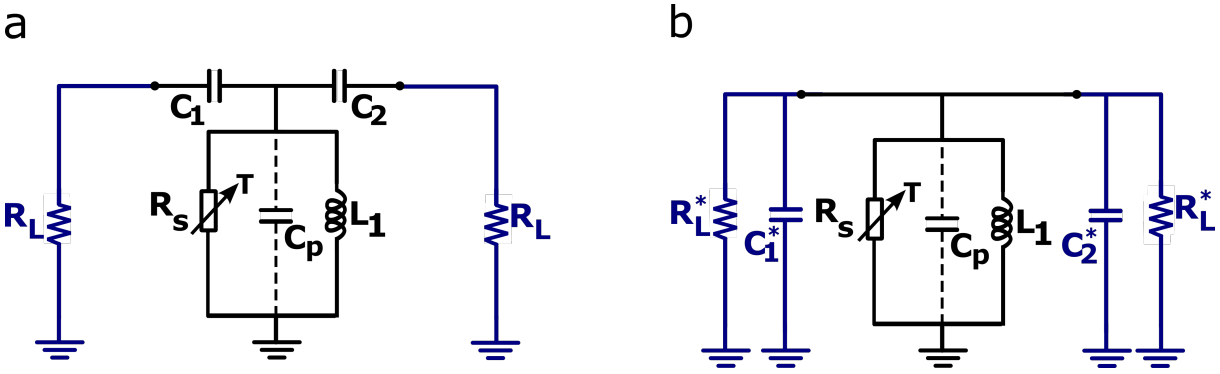

Figure 3.10: ***a.*** *The readout circuit loaded with the characteristic impedance of the transmission line* ***b.*** *The Norton equivalent of the same circuit which highlights the impedance transformation. (adapted from [173])*

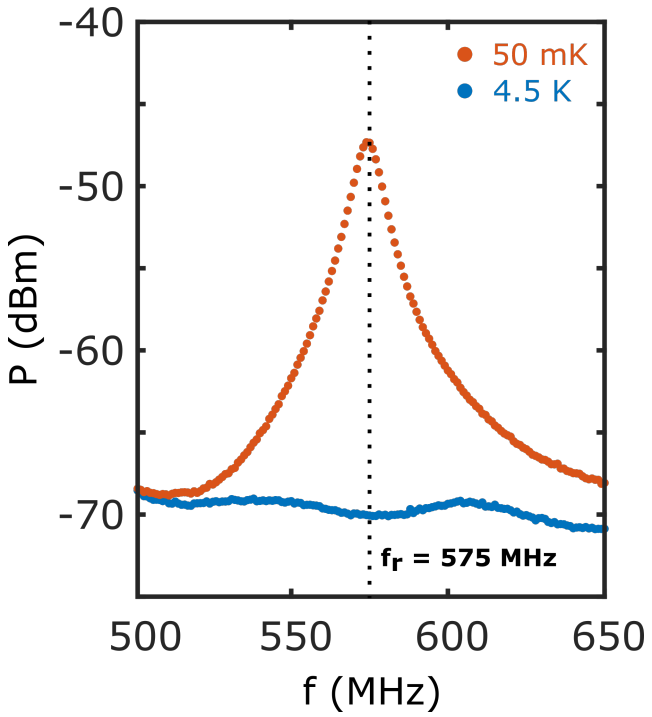

Figure 3.11: Transmission spectrum of the superconducting resonator chip taken at $T = 50$ mK (orange) and $T = 4.5$ K (blue) The resonance centered at $f_0 \approx 575$ MHz with a bandwidth ~ 10 MHz emerges below T_c of aluminium.

3.6 Probing the switching between dissipative and coherent states in an SNS junction current biased near I_c

In Chapter 2, we saw that the switching current of an SNS Josephson junction obeys a statistical distribution due to the noise present in the system. When biased at a fixed current in the vicinity of I_c, the Josephson junction alternates between the coherent and the resistive states, producing a timetrace similar to the random telegraph noise [176]. To observe this instability near I_c, we come up with a composite device shown in Fig. 3.12. On the right side, the nanofabricated normal island (Cu) is in clean contact with two superconducting leads (Al), thus forming an SNS junction. The contact pads are positioned at $\sim$ 500 nm from each other. On the left end, N extends further and forms a SIN junction with the third superconducting electrode (Al) via grown oxide layer. The sample is fabricated via physical vapor deposition with three angles where we first deposit the angle ($-20°$) corresponding the third electrode (25 nm Al). Next, a brief oxidation step is introduced to form the insulating layer of the SINS thermometer. Oxygen is introduced to the loadlock until the chamber pressure reaches 0.25 mbar. Next, the sample is let to oxidize during 5 seconds and then the loadlock is repumped. Note that, given the short oxidation time and the time it takes to repump the loadlock, the given recipe is rather nominal. However, reproducible results were obtained in PLASSYS HV Evaporator. The subsequent steps deposit Cu (45 nm) at 0° angle and finally the Al layer (65 nm at +20°) which constitutes the clean contacts of the SNS junction. The logic behind such a configuration is that it allows the simultaneous current biasing of the SNS junction and the monitoring of the temperature in N via SINS junction used as a proximity thermometer.

As a preliminary step, we first conduct tunneling spectroscopy measurements of the SINS junction between 100 mK and 600 mK. The results shown in Fig. 3.13 clearly demonstrate the temperature dependence of the conductance peak at $V_{bias} = 0$, thereby validating the use of SINS junction as the proximity thermometer.

Next, in a four wire setup, we characterize the temperature dependence of the switching current (I_{sw}) of the SNS junction (Fig. 3.14). The junction features $I_{sw} \approx 4.6$ µA and $I_{sw}/I_R \approx 2.94$ at T = 100 mK where I_R stands for the retrapping current. The I_{sw}/I_R ratio gradually decreases as the temperature is increased and the hysteresis vanishes around T $\approx$ 350 mK. Despite being intrinsically overdamped, SNS junctions were shown to present thermal hysteresis which stems from the heating of N as the system switches to the resistive state [128]. To probe the instability near I_c, the hysteretic regime must be avoided. For the fast readout, we couple the sample with the superconducting microwave resonator with a wirebond. In Fig. 3.15, we show several frequency spectra of our system taken between 100 mK and 500 mK with three different input powers. Overall, we observe

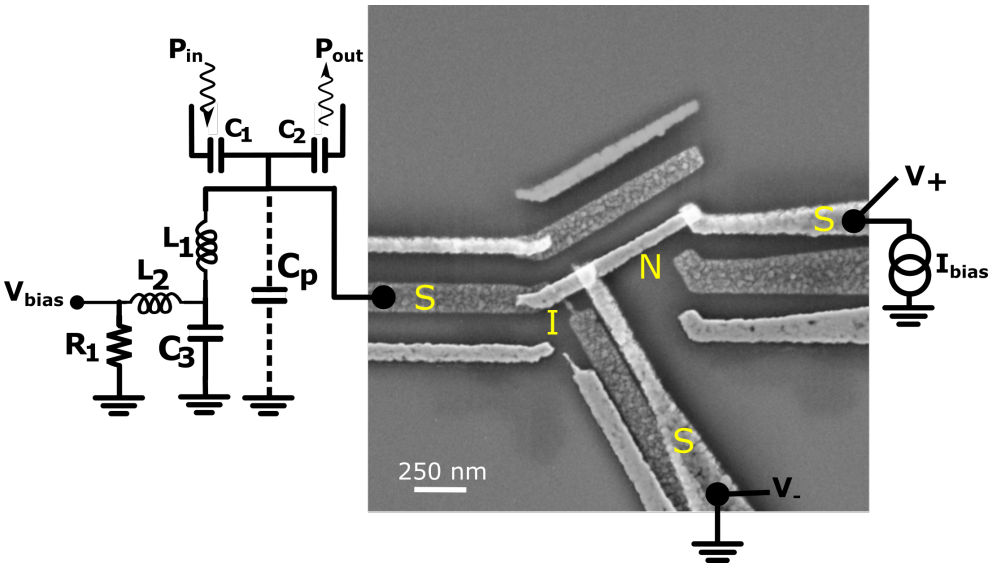

Figure 3.12: SEM image of the device augmented with the measurement setup schematics. The superconducting (S) and the normal (N) electrodes are labeled in yellow

the resonance around $f_0 \approx 560\,\mathrm{MHz}$ with a bandwidth $\mathrm{BW} \approx 17\,\mathrm{MHz}$. The frequency response of the system follows the properties of a parallel RLC resonator, yielding a higher quality factor at higher temperatures due to increasing tunneling resistance. Among the tested input powers, $P_{in} = -110\,\mathrm{dBm}$ provides the best responsivity $\mathcal{R} \approx 0.057$ dB/mK between 100 mK and 200 mK whereas the thermometer response is limited by the noise floor for $P_{in} = -120$ dBm and by the too coarse differential signal which goes beyond the zero bias conductance for $P_{in} = -100$ dBm.

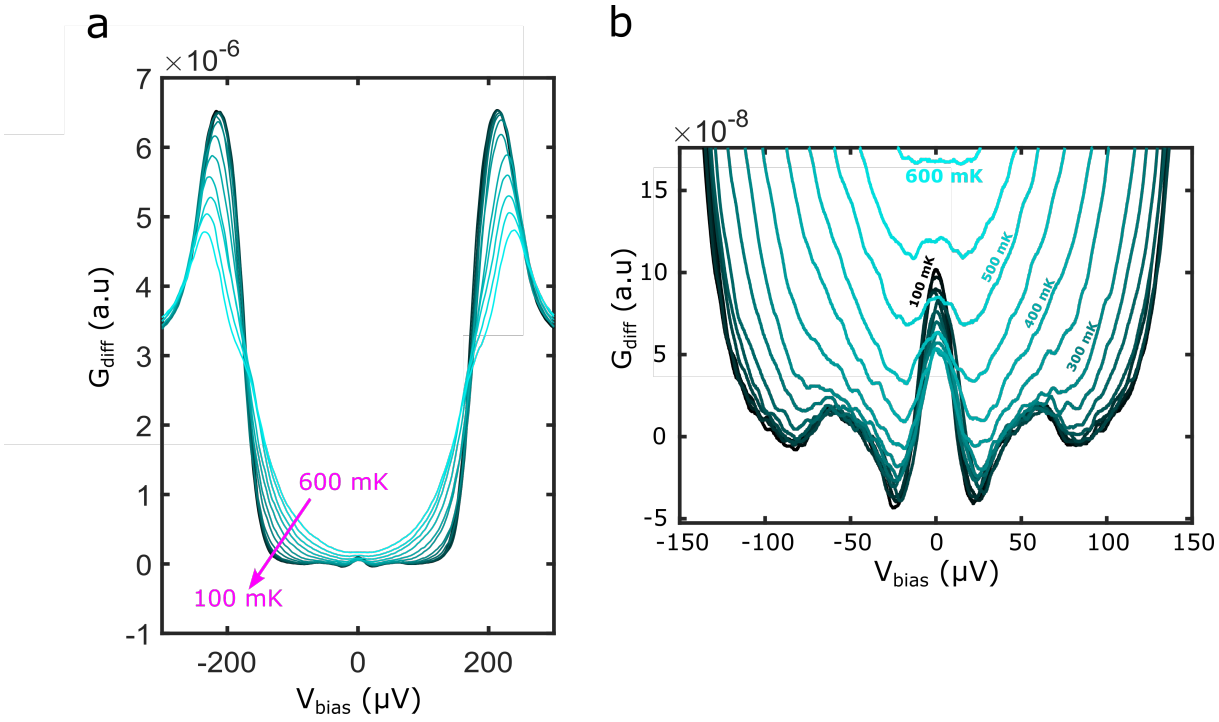

Figure 3.13: ***a.*** *Tunneling spectroscopy of the SINS Junction between T= 100 mK and T = 600 mK obtained via lock-in amplification.* ***b.*** *Zoom around $V_{bias} = 0$ of the same data. The temperature dependence of the zero-bias conductance peak is visible.*

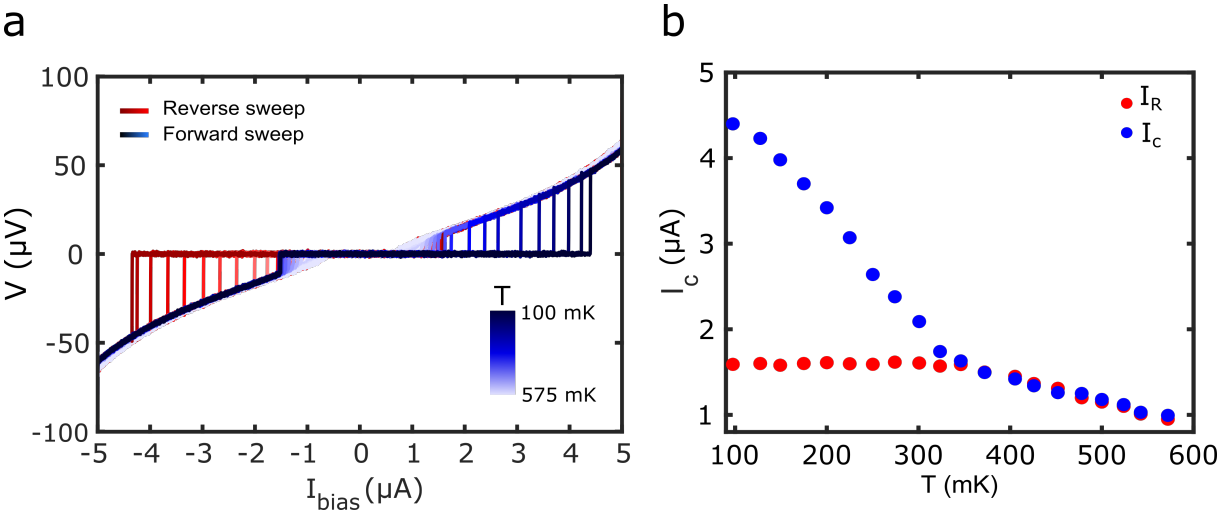

Figure 3.14: ***a.*** *V - I_{bias} curves of the SNS junction taken between T = 100 mK and T = 575 mK. The forward (reverse) sweeps are marked in the shades of blue (red).* ***b.*** *I_c (T) curve extracted from the data shown in* ***a.***

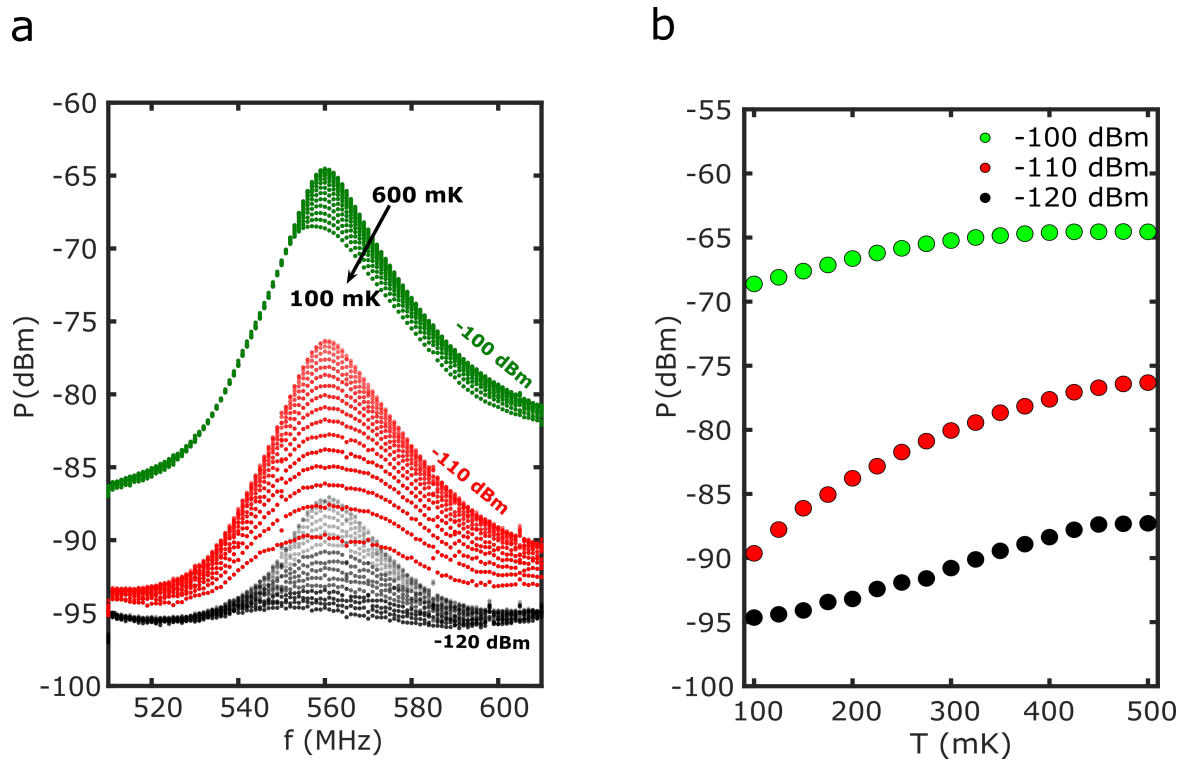

Figure 3.15: ***a.*** *The transmission spectra of the system between $T = 100$ mK and $T = 600$ mK for three different input powers: $P_{in} = -100\,dBm$ (green), -110 dBm (red) and -120 dBm (black) sampled at $f_s = 10$ kHz during 1 s.* ***b.*** *The calibration curves extracted from the transmission spectra at the resonant frequency*

3.6.1 Real time measurement

Having obtained the fundamental properties of our system, we proceed to the experiment where we seek to resolve in real time the switching instabilities. For this purpose, we first set the temperature to T = 400 mK where the hysteretic behaviour has completely vanished. At this temperature, the SNS junction features $I_{sw} \approx 1.4$ µA. Next, we fix the sampling frequency to $f_s = 200$ kHz and the input power to $P_{in} = -100$ dBm for an improved SNR. In Fig. 3.16, we show the histograms of the coherent and the resistive states recast from the time traces taken at $I_{bias} \ll I_{sw}$ and $I_{bias} \gg I_{sw}$ during 1 s, respectively. Both histograms are fitted with Gaussian distributions whose centers are positioned ~ 2.1 dB apart which is greater than $3(\sigma_C + \sigma_R)$ where $\sigma_C = 0.22$ dB and $\sigma_N = 0.18$ dB correspond to the standard deviation of the coherent and normal state, respectively. Therefore, under given measurement conditions we have a clear distinction between two states.[1]

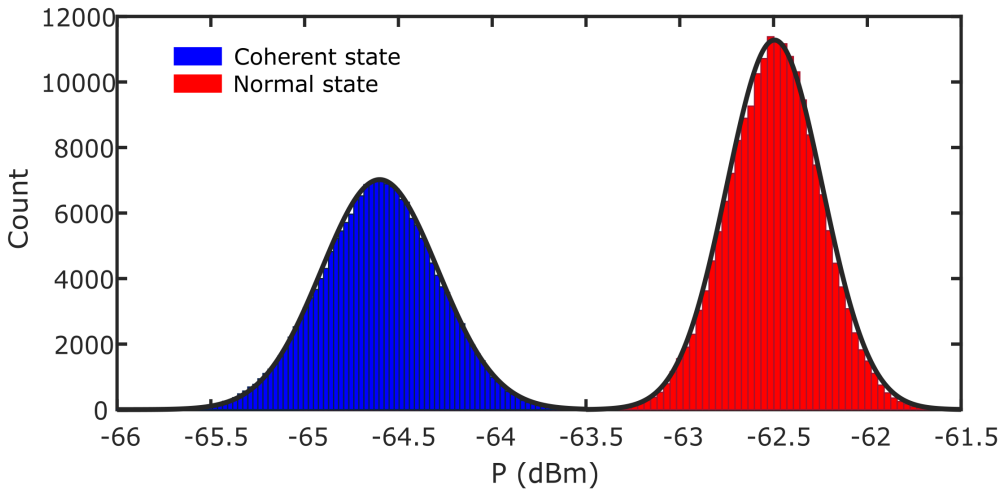

Figure 3.16: The histograms of the real time traces taken at $I_{bias} \ll I_{sw}$ (blue) and $I_{bias} \gg I_{sw}$ (red). The mean values are ~ 2.1 dB apart.

Fig. 3.17a shows the results of a series of real time measurements where I_{bias} is incremented from 1.35 µA to 1.45 µA. The gradual transition to the resistive state as I_{bias} increases is clearly visible. At $I_{bias} = 1.39$ µA, the system resides in the resistive state during 20% of the total measurement time. This percentage goes up to 66.5% already at $I_{bias} = 1.40$ µA. At $I_{bias} = 1.45$ µA, the transition is pretty much complete with 99.99% of relative time spent in the resistive state. Similar results were obtained in numerical

[1]The narrower spread of the data in the normal state ($\sigma_N < \sigma_C$) shown in Fig. 3.16 is the result of a mathematical artifact. Namely, representing the signal amplitudes in dBm unit gives a geometric nature to the mean and the standard deviation of the shown distributions. Keeping the arithmetic standard deviation same, it can be shown that the geometric standard deviation scales inversely with the increasing arithmetic mean which explains the narrower spread of the data corresponding to the normal state. We verify this fact by replotting the figures in Watt unit where we observed $\sigma_N = \sigma_C$. The same phenomenon explains the difference between the mean counts of the histograms . For the same bin size, the histogram of the normal state becomes more densely populated around the mean and yields an increased count.

simulations within the framework of phase diffusion in moderately damped ($\beta_c < 5$) Josephson junctions [177]. In the overdamped case, the premature switching due to thermal noise is known to be the cause of the finite $\langle V \rangle$ at $I < I_c$, and is taken into account in the Ambegaokar-Halperin model [178]. Next, we extract the switching frequencies as a function of the I_{bias} from the time traces taken between $\mathrm{I_{bias}} = 1.35$ µA to $\mathrm{I_{bias}} = 1.45$ µA. The statistical properties of the switching distributions are considered as the indicators of the activation regime in which the Josephson junction operates. In the thermal activation regime, the width of the switching distribution $\Delta I = \langle \sqrt{(I - \langle I \rangle)^2} \rangle$ were shown to scale as $\Delta I \propto T^{\frac{2}{3}}$ [179] whereas at $k_B T \ll E_j$, where the macroscopic quantum tunneling is the dominant switching mechanism, distribution width saturates [180]. In both regimes, the escape rates scale with the Josephson plasma frequency ω_p and the distributions feature negative skew ($\tilde{\mu_3} = \mu/\sigma^3$). However, increasing the temperature causes the switching and the retrapping dynamics to overlap which symmetrizes the distributions. In Fig. 3.17b, we show the histogram of the switching rate distribution. The instability is maximized around $\mathrm{I_{bias}} \approx 1.396$ µA with a switching rate of f ≈ 620 Hz and $\sigma = 11.3$ nA. The difficulty of the analysis for SNS junctions comes from the fact that ω_p is not a well defined quantity. Nevertheless, the detrimental role of the damping on the escape rates were elucidated in Caldeira-Leggett model [181], where an attempt frequency (ω_A) defined as $\omega_A/2\pi = \sqrt{B_c}\omega_p$ determines the escape rates. Therefore, we fit the data by assuming $\omega_A = 620$ Hz and using the generalized form of the thermal activation function [182]

$$\Gamma(I,T) = \frac{\omega_A}{2\pi} e^{-gdU/k_B T} \tag{3.24}$$

where g=7 is a scaling factor which controls the spread and dU is the barrier height of the potential energy given as [183]

$$dU(I) = \frac{4\sqrt{2}}{3} E_J^{T=400\,\mathrm{mK}} \left(1 - \frac{I}{I_c^{T=400\,\mathrm{mK}}}\right)^{\frac{3}{2}} \tag{3.25}$$

Note that the fit is not capable of capturing the slightly positive skew $\tilde{\mu_3} = 0.66$ which data presents. The origin of this positive skew is not understood and requires further investigation at various temperatures. The combined exponent g/T in Eq. (3.25) can be seen as the inverse of the modified temperature. In Ref. [0], $g < 1$ is used to take into account the difference between the junction and the bath temperatures. In our case, $g > 1$ therefore corresponds to a reduced experimental temperature which results in a narrower distribution. The discrepancy encountered here might in fact point to an experimental limitation of our measurements. The fact that we sample the time traces at $f_s = 200$ kHz might introduce a cut-off effect. Basically, we are not able to capture the switches occurring at $f > f_s$ which narrows the spread of the switching distributions as the escapes far from I_c present typically shorter lifetimes. It should also be noted that the temperature dependence of the system parameters E_j and I_c as the system switches to running state is ignored.

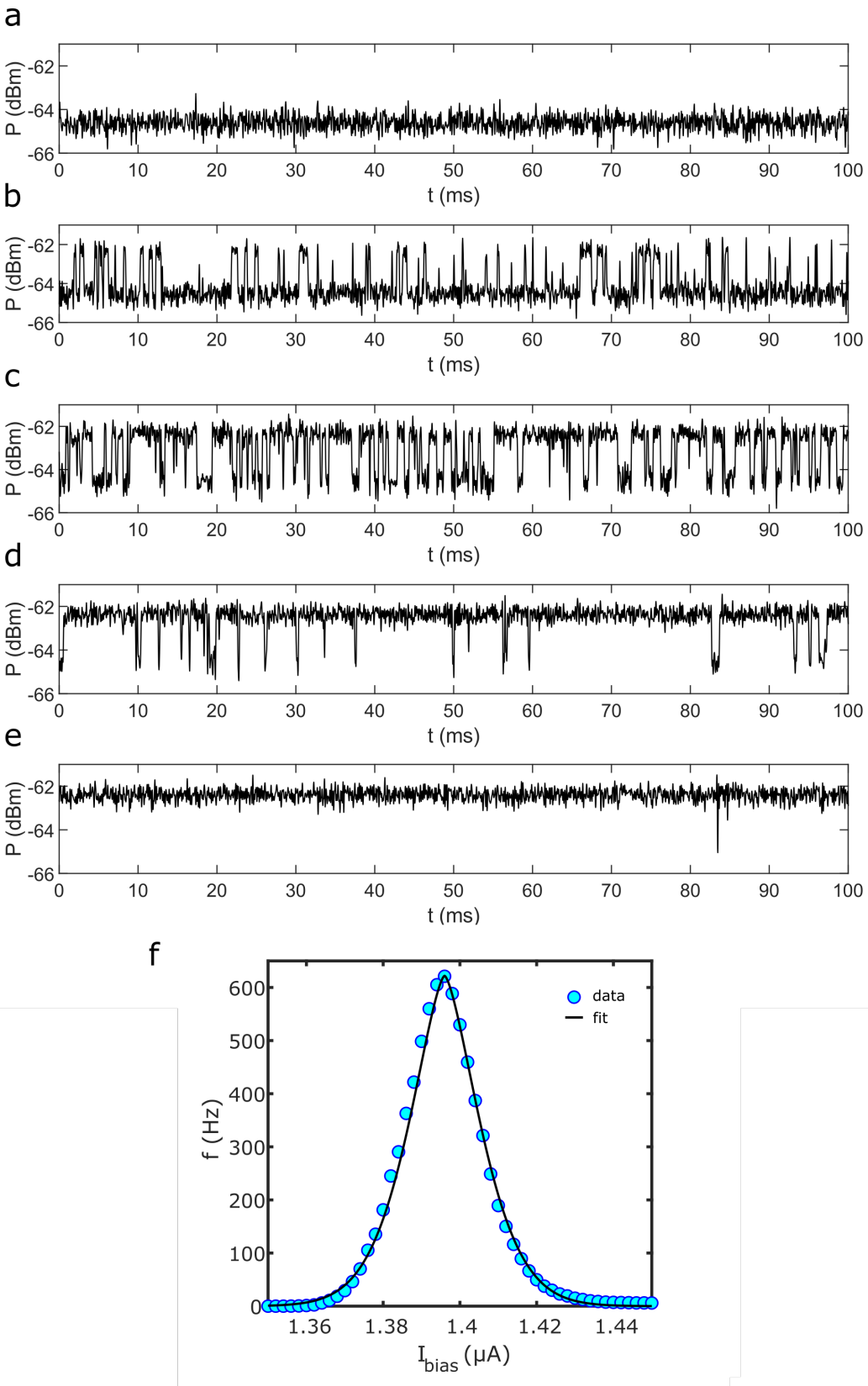

Figure 3.17: The real time measurements taken with f_s = 200 kHz and P_{in} = -100 dBm at ***a.*** *I_{bias} = 1.35 μA* ***b.*** *I_{bias} = 1.39 μA* ***c.*** *I_{bias} = 1.40 μA* ***d.*** *I_{bias} = 1.41 μA* ***e.*** *I_{bias} = 1.45 μA* ***f.*** *The extracted switching rates from the real time measurements and the fit with the scaling factor g = 7.*

Chapter 4

Detecting Individual Phase Slips

4.1 Introduction

In this chapter, we introduce our device: the superconductor quantum interference proximity transistor (SQUIPT) [4] and elaborate on the design requirements for detecting in real time the thermal signature of the individual phase slips. Next, we present the fabricated samples and the experiments we conducted on them. The engineering aspect of the device design was a true challenge. We had to iterate over several designs based on the measurement results. Therefore, we find it useful to explain the evolution of our sample rather than jumping to the final design. The modifications comprise mainly the device geometry, the material choice and the type of external $\vec{B}$ source and the coupling to it. Hence, our journey begins with a hexagonal SQUIPT with a macroscopic coil as a $\vec{B}$ source and ends with a seven times bigger device with an on-chip rapid flux line which in the end allowed us to detect the phase slips.

4.2 Main Idea

We seek to demonstrate the real time detection of the thermal signature of a phase slip in a SQUIPT. This event can be seen as the equivalent picture of a magnetic flux quantum Φ_0 tunneling to/from the loop (Fig. 4.1.a). The experiment consists in ramping the the phase (φ) of a hysteretic SQUIPT operating in the overdamped regime via an external flux source, up to the point where a phase slip occurs. The difference in the internal energy of the system following this event is then absorbed by the electron population of the normal metal (N) which acts as the weak link. Therefore, after a phase slip, the electronic temperature (T_e) of N undergoes a rapid increase and then relaxes back to its equilibrium value mainly thanks to the electron-phonon coupling which evacuates the excess of energy towards the subsequent phonon systems. At sub-K temperatures, the weakened electron-phonon interaction sets this relaxation in the μs scale which is within the experimental reach. Apart from the clean superconducting (S) contacts on N which

forms a SNS Josephson junction, we add a third S contact separated from N via an oxide layer and exploit the SIN junction as the proximity thermometer. Finally, the fast readout is achieved by embedding the whole system in an resonant readout circuit with a large bandwidth ($\sim$ 10 MHz) as discussed in Chapter 3.

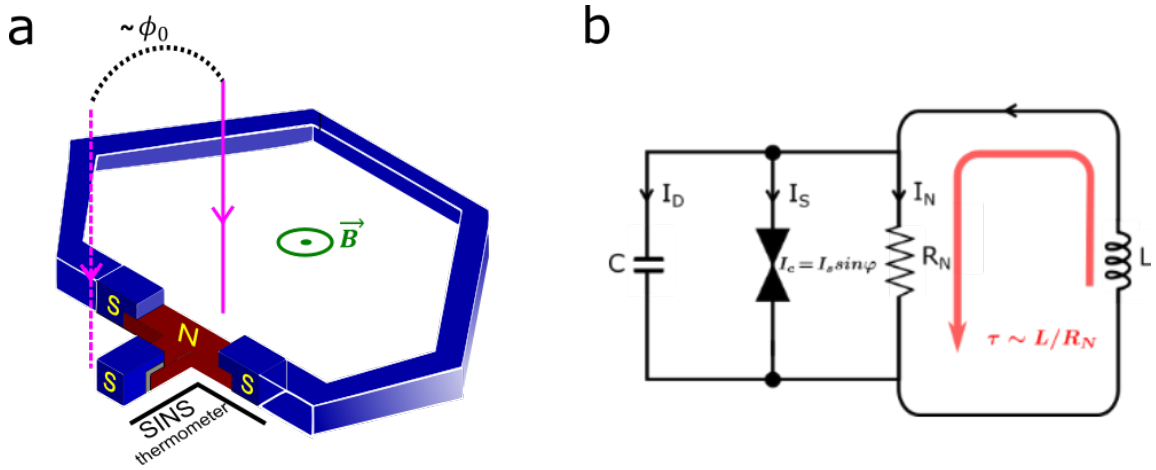

Figure 4.1: ***a.*** *A sketch of the SQUIPT. The superconducting loop (blue) is interrupted by a normal metal (red). SINS thermometer is formed by the addition of a third superconducting electrode, the oxide layer and the NS lead (black line). A magnetic flux quantum penetrating the loop during a phase slip is depicted with the pink arrows.* ***b*** *The equivalent circuit model of the device. The superconducting loop is represented by its total inductance L. Whenever a phase slips occurs, the difference in internal energy (ΔU) is dissipated on the normal metal (red arrow).*

4.3 Device Configuration

In simple words, the SQUIPT is a variant of RF-SQUID where the weak link of the superconducting loop is formed by a normal metal in clean contact on both ends with the superconducting electrodes of the loop, thereby forming an SNS type Josephson junction (Fig. 4.1.a). The mesoscopic scale ($\sim$ 500 nm) of the N which is typically in the diffusive transport regime allows the incorporation of a third superconducting electrode in tunnel contact with N via an oxide layer. With such a configuration, it becomes possible to exploit the phase dependence of the proximity effect via an external $\vec{B}$ source and simultaneously probe the DOS of the proximitized N via tunnel spectroscopy, which yields a transistor-like behaviour [4]. Having already explored the fundamentals of Josephson junctions, SQUID and the phase slips in a hysteretic SQUID, here we will focus on the role of normal metal, the thermal model of our device and the engineering of a hysteretic device.

4.3.1 The role of the Normal metal

The normal metal inserted in the superconducting loop has three main roles:
1. Weak link: As discussed in Chapter 1, the normal metal allows the coherent transport of Cooper pairs under the proximity effect hence forming the SNS junction of the loop. This way, our device is governed by the operating principles of an RF-SQUID. The design parameters and the suitable regime for observing individual phase slips are detailed in the following section.
2. Absorber: Fig. 4.1b shows the circuit equivalent of our device. The difference in the internal energy (ΔU) which accompanies the phase slip is dissipated in the form of Joule heating of the quasiparticles of the normal metal. The energy transfer takes place on the sub-nanosecond timescale - dictated by $\tau \sim L/R_N$ where L (~ 0.5 nH) is the total loop inductance and the R_N ($\sim 1.3\,\Omega$) is the normal state resistance of the weak link - and raises the electronic temperature (T_e) of the normal island. From a detection perspective, the normal part therefore acts as the calorimeter absorber and allows us to capture the thermal signature of the individual phase slips.
3. Phase dynamics: In Chapter 1, we discussed the dynamic behaviour of the Josephson phase and showed that the transitions between the coherent and the resistive states depend on the device parameters. Unlike current-biased Josephson juctions, there is no running finite voltage state in an RF-SQUID.Nevertheless, the system switches to the finite voltage state during a phase slip between two metastable S states. The device characteristics, hence the operating mode, determines the transient phase response and the number of slips ($\Delta n = |n_1 - n_2|$) prior to the retrapping of the phase particle (Fig. 4.2).
3.1 Underdamped ($\beta_c > 1$, $\Delta n > 1$): In the underdamped regime, the so-called phase particle may have enough kinetic energy to overcome several local minima before getting retrapped. Two critical thresholds of the Stewart-McCumber parameter ($\beta_{1,2}$) control the transient behaviour; they are given as $\beta_1 \approx 4(\pi/\beta)^{0.5}$ and $\beta_2 \approx 0.25\beta$. Note that $\beta = 2\pi L I_c/\Phi_0$ is the screening parameter [185] whereas $\beta_{1,2}$ represent the threshold values of the Stewart-McCumber parameter. In the case where the damping regime of the system meets the condition $\beta_1 < \beta_c < \beta_2$, the phase oscillations are attenuated in $\tau_s \approx L/R_N$ and $(\Delta n)_{max} = N \approx \beta/2\pi$ whereas $\beta_c > \beta_2$ corresponds to the very low damping case: the transient response is highly oscillatory, the oscillation period $\tau > \tau_s$ and Δn becomes arbitrary within 2N.
3.2 Overdamped ($\beta_c < 1$, $\Delta n = 1$): The overdamped regime is the suitable operation mode for the detection of individual phase slips as explained in Chapter 1. In a SQUID, whenever a phase slip is triggered, the phase particle is retrapped in the next metastable point, admitting a single magnetic flux quantum in the loop. The time constant governing the phase evolution is given by $\tau_S \approx 3\omega_c^{-1}$ where $\omega_c = R_N/L_J$ represents the Josephson characteristic frequency [185] related to the time $\tau = L_J/R_N$. Note that $L_J = \frac{\hbar}{2eI_c}$ is the Josephson inductance. Additionally, the initial motion near $\Phi = n\Phi_0$ is determined by the turn-on delay $\tau_d \approx \frac{\pi}{\mu}\omega_c^{-1}$ where $\mu = (I - I_c)/I_c$ is the relative current overdrive beyond

I_c. SNS junctions are intrinsically overdamped as they feature negligible capacitance and very low normal resistance ($R_N \sim \Omega$) in contrast to SIS junctions where $R_N \sim k\Omega$. Therefore, interrupting the superconducting loop with N naturally places the RF-SQUID in the suitable regime for observing individual phase slips.

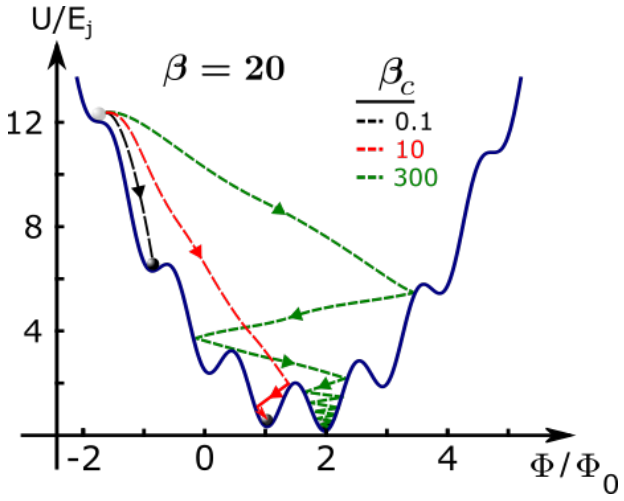

Figure 4.2: The transient dynamics of the phase slips in a largely hysteretic SQUIPT ($\beta = 20$) for three different regimes: overdamped (black), underdamped (red) and strongly underdamped (green) (adapted from [185])

4.3.2 The role of the EM environment on the thermal model

In Chapter 2, we discussed the thermal model of the normal metal in an SNS Junction for the calorimetric detection of an energy quanta. Given the fact that our system is embedded in a resonant microwave circuit and is driven by a sine tone with $f_s \sim 575$ MHz, in what follows, we discuss the impact of the EM environment on the thermal model.

Radiative loss: The electron gas of the N island is coupled to the electromagnetic environment (Fig. 4.3) via superconducting leads and exchanges energy with it according to the fluctuation-dissipation theorem [149]. It is therefore necessary to take into account the electromagnetic channel, through which N emits thermal photons ($\nu_{th} = k_B T/h$) once the instantaneous heat from a phase slip is absorbed. The net power flow from the N to the environment can be written as [186]

$$P = r \int_0^{+\infty} h\nu[n_e(h\nu) - n_{env}(h\nu)]d\nu \qquad [W] \tag{4.1}$$

where $r = 4R_N R_{env}/(R_N + R_{env})^2$ is the coupling coefficient between the N and the environment, $n(\epsilon) = [\exp(\epsilon/k_B T) - 1]^{-1}$ is the Bose-Einstein distribution of photons. Considering a lossless coupling ($Z(\omega) = 0$) and evaluating the integral, Eq. (4.1) can be shown to have the form [187]

$$P_\nu = r\frac{\pi k_B^2}{12\hbar}(T_{e_N}^2 - T_{e_{env}}^2) \tag{4.2}$$

where T_{e_N} and $T_{e_{env}}$ represent the electronic temperature of the N island and the environment respectively. $P_\nu \propto T^2$ suggests that below a crossover temperature (T_{cr}), the photonic cooling becomes the dominant relaxation mechanism over the electron-phonon coupling ($\propto T^5$). For mesoscopic devices ($\Sigma \sim 1 \times 10^9$ W/m^{3}K^5 and $\mathcal{V} \sim 10^{-20}$m^3), T_{cr} could reach up to $\sim 150 - 200$ mK, which is well within the experimental reach. Indeed, several demonstrations of quantum limited heat transport ($G_Q = \pi k_B^2 T/6\hbar$)) can be found in thr literature [187–189]. It should be noted that the impedance matching between the device and the environment plays a crucial role in such experiments. In our case, the contact fingers (Cu) deposited on the same run with N island forms the environment (R_{env}) seen by the device through a superconducting lead (Fig. 4.3b). No special attention was given to the impedance matching. As a consequence, calculating the sheet resistances, we find that R_{env} and R_N are in the weakly coupled regime ($r \sim 0.03$). Moreover, the non-zero impedance ($Z(\omega) \neq 0$) of the superconducting lead should be taken into account which further suppresses $r < 0.03$. Overall, we obtain $P_\nu < 0.1$ fW and $T_{cr} < 55$ mK. In Ref. [3], the possible observation of a $T_{cr} \approx 30$ mK was reported for a copper absorber with a volume $\mathcal{V} = 1.0 \times 10^{-21}$ m^3.

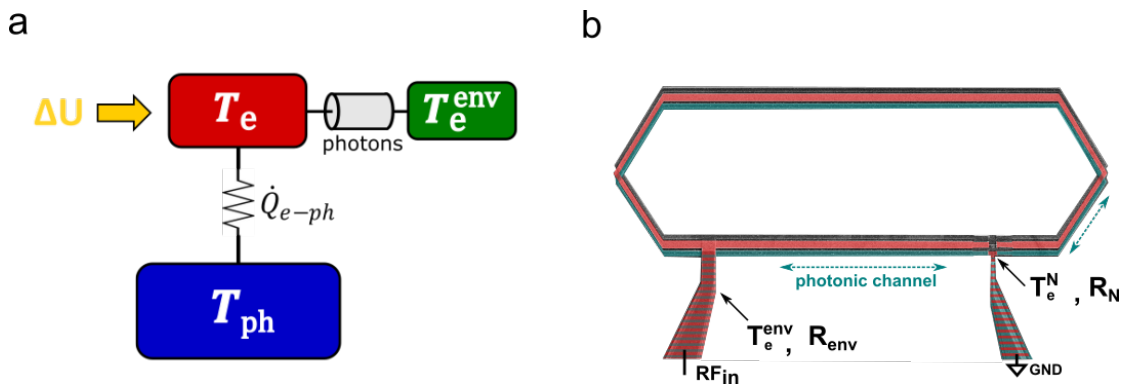

Figure 4.3: ***a.*** *Thermal model of the normal absorber. The weakly coupled systems of electrons and phonons are shown in red and blue, respectively. The absorber electrons also exchange energy with the EM environment via spontaneous emission of photons. The dissipation caused by the phase slip is absorbed by the electron population (yellow).* ***b.*** *The schematic view of the sample. The superconducting loop (cyan) has an overlap with the normal part (red) due to the angle deposition method employed. The overlapping electrodes are dashed. The left electrode is in clean contact with the superconducting loop and is therefore considered as the environment. The right electrode is seperated from the N island via an oxide layer and is excluded from the calculations.*

AC heat load: We probe our system with a sinusoidal tone at $f_r = 575$ MHz and $P_{in} = -110$ dBm. The incident power (P_{in}) is mostly transferred to the output (P_{out}) and read at T_{room}. However, a fraction of P_{in} is lost to the system. Due to the presence of a

tunneling resistance ($R_T \sim 10$ kΩ), the dissipation (P_{AC}) corresponds to a steady-state heating of N the island which drives $T_e > T_{ph}$. At low temperatures ($T < 200$ mK), this overdrive can be significant and therefore needs to be taken into account in thermal calculations. Considering that $\dot{Q}_{e-ph}$ is the dominant relaxation mechanism, we can write the thermal balance as

$$P_{AC} = \dot{Q}_{e-ph} = \Sigma\mathcal{V}(T_e^5 - T_{ph}^5) \tag{4.3}$$

Isolating T_e, we obtain

$$T_e = \left(\frac{P_{AC}}{\Sigma\mathcal{V}} + T_{ph}^5\right)^{\frac{1}{5}} \tag{4.4}$$

Fig. 4.4 shows $T_e(T_{ph})$ for various P_{in}. We have taken $\Sigma_{Cu} = 2.10^9$ W/m^{3}K^5 which is a standard value in literature and the N volume is $\mathcal{V} \sim 0.008$ μm^3. It can be seen that $\min(T_e) \sim 76$ mK at $P_{in} = -110$ dBm which sets the lower temperature limit in our experiments. One is tempted to further decrease P_{in}. However, we will see that $P_{in} < -110$ dBm presents other challenges in terms of phase slip detection.

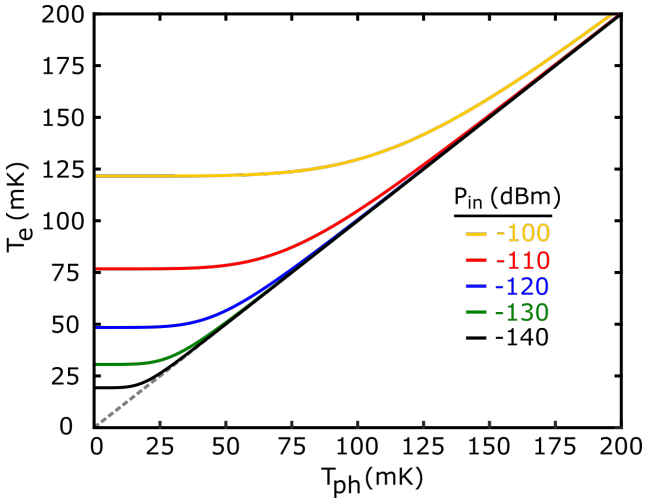

Figure 4.4: The heat load on the absorber caused by the input signal. The calculated electronic temperature (T_e) is plotted versus the phonon temperature T_{ph} for various P_{in}. We consider T_{ph} thermalized with the setup (T_{bath}). $\Sigma_{Cu} = 2.10^9$ W/m^3K^5 is used calculations which is a standard value from the literature. The volume of the normal island is $\mathcal{V} \sim 0.008$ μm^3.

4.3.3 Hysteretic SQUIPT

As discussed in Chapter 1, the RF-SQUID has two distinct regimes based on the screening parameter: weak screening ($\beta < 1$), and the hysteretic regime ($\beta > 1$) . The phase slips occur solely in the latter where the $\Phi(\Phi_x)$ function is multi-valued. Therefore, designing a device in the hysteretic regime is the first condition for observing phase slips. Considering the expression of $\beta = LI_c/\Phi_0$, we see that the LI_c product has to be made greater than $\frac{\Phi_0}{2\pi}$ which provides two experimental parameters to adjust in this perspective:

1. Self-inductance (L_{tot}): The total self-inductance of the device consists of a geometric, and a kinetic term.

$$L_{tot} = L_{geo} + L_k \tag{4.5}$$

The geometric inductance stems from the loop shape. Several analytical expressions for simple geometries can be found in the literature [190]. For the μm-scale mesoscopic devices with a single turn, $L_{geo} < 200$ pH is expected. In our design, we refer to the electromagnetic simulations ("Sonnet Suites") for a rigorous determination of L_{geo}.
Kinetic inductance is related to the inertia of the charge carriers in superconductors. In the dirty limit, where the mean free path l is smaller than the BCS coherence length ξ_0, the kinetic sheet inductance can be calculated as $L_{k\square} = (\hbar\rho_n)/(\pi\Delta t)$, where ρ_n, Δ, and t are the normal state resistivity, the superconducting gap, and the layer thickness, respectively [191]. Note that ρ_n/t corresponds to the sheet resistance $R_\square$. Therefore, $L_{k\square}$ can be deduced from resistance measurements.
Kinetic inductance is inversely proportional to the thickness and becomes important in thin superconducting films. Depending on the application, this can be a desired or an unwanted feature. To name a few applications where high kinetic inductance is sought; thin films of highly disordered superconductors such as TiN [192], Nb_xSi_{1-x} [193], and granular Al [194] were shown to have $L_{k\square} \sim 1$ nH, and have potential uses in flux qubits [195, 196]. Josephson junction arrays form superinductors [197] which provide a high impedance environment with $Z_{env} = \sqrt{\frac{L_{array}}{C}}$ such that $Z_{env} \sim Z_Q$ where $Z_Q = \frac{h}{2e} \approx 6.5$ kΩ and are used in parametric amplification [198]. In our case, the SQUID loop made of Al which we deposit simply by physical vapor deposition yields $L_{k\square} \sim 1.1$ pH which corresponds to a typical value found in the literature.
2. SNS Josephson junction critical current (I_c): In the long diffusive limit ($E_{Th} \ll \Delta$), $I_c(T = 0)$ scales with E_{Th}/R_N. Therefore, making the N lead as short and wide as possible is the good design direction for obtaining hysteretic behaviour. However, two limiting factors arise: (1) some finite length must be allocated to the tunneling contact ($\sim$ 250 nm) and the clean NS overlaps ($\sim$ 100 nm) which sets $L_{min} > 450$ nm, and (2) given the 3-step angle deposition method we employ to fabricate the device, the N island width is limited by a possible overlap with the shadow deposited Al contacts which should be avoided. Opting for the dimensions $(L, W, t) = (700\text{ nm}, 250\text{ nm}, 35\text{ nm})$ and considering the typically reported [42, 63, 199, 200] diffusion coefficients of copper, $D_{Cu} \in [70, 250]$ cm^2/s, we expect $2 \lesssim I_c \lesssim 10$ μA. It should be noted that it is not possible to measure I_c with our device. Figure 4.5 shows the dependence of β and the ΔU on the loop inductance (L) and the critical current (I_c). Within the shown I_c range, any device with $L_{tot} \geq 100$ pH fulfills the hysteresis condition.

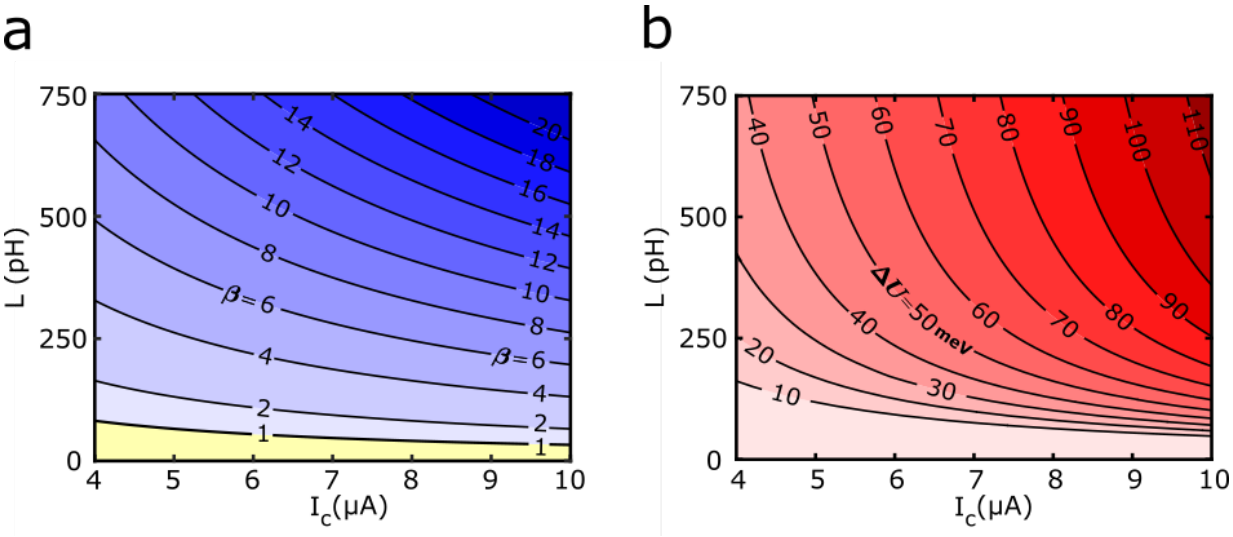

Figure 4.5: ***a.*** *The 2D contour plot of the screening parameter β as a function of the inductance (L) and the critical current $I_c(T = 0)$. The hysteretic regime is shown in gradient blue. The weak screening regime is marked in yellow.* ***b.*** *The 2D contour plot of the change in internal energy ΔU dissipated on N following a single phase slip with respect to $I_c(T = 0)$ and inductance(L) .*

4.4 Device Designs

4.4.1 A Preliminary Device

Geometry. Our first device is a hexagonal SQUIPT with $\sim 46\,\mu\text{m}^2$ of surface area (Fig. 4.6). It is mostly inspired by the design in [4]. The superconducting loop (Al), the normal island (Cu) and the superconducting probe contact (Al) are all deposited in the same run with the three angle shadow evaporation technique, having respective thicknesses of 60 nm, 35 nm, and 25 nm. The entire device sits on an intrinsic Si wafer. The T-shaped N island is 500 nm long and has a volume of $\sim 0.006\,\mu\text{m}^3$. The N island is in clean contact on both ends with Al leads where the overlap area is 125 nm x 210 nm (95 x 210 nm) due to the slight misalignment. The oxide layer (AlOx) of the tunnel barrier, which separates the N island from the probe contact was grown by the controlled oxidization (P = 0.25 mbar, t = 5 s). The overlapping area with the probe contact is 250 nm x 200 nm.

Measurement. We conduct transport measurements at $T_{base} = 50$ mK. In a 2-wire configuration, the NIS junction is voltage biased and the output current is read via a trans-impedance amplifier at T_{room}. The I(V) curve is presented in Fig. 4.7b. The onset of the quasiparticle current corresponds to a bias $eV \approx \Delta - \Delta_g \approx 200\,\mu$eV. The slope yields $R_T \approx 12.5$ kΩ. The anti-symmetric bumps within $\pm 40\,\mu$eV around the origin (Fig. 4.7c) stem from the tunneling supercurrent which confirms that N is under proximity effect. The peak current (~ 110 pA) occurs at $V \sim \pm 12\,\mu$eV.

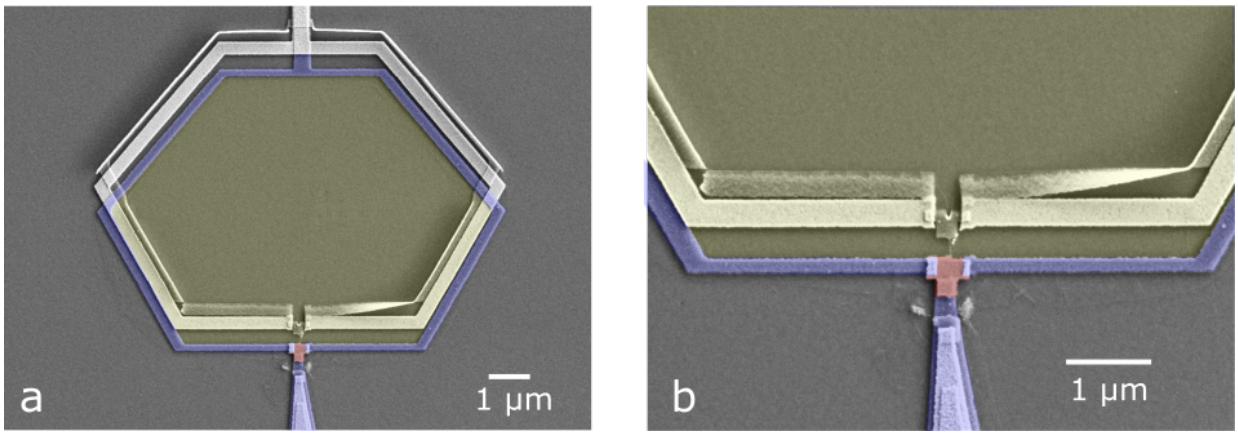

Figure 4.6: SEM view of the first-generation SQUIPT. ***a.*** *The angle evaporation method generates three replicates of the same pattern. The superconducting electrodes used to form the device are marked in blue. The surface area is highlighted in yellow and the absorber normal metal is in red.* ***b.*** *The zoomed view of the same device. The slight asymmetry of the clean contacts on the T-shaped N island is visible.*

I($\vec{B}$) characterization

Next, we focus on the $\vec{B}$ dependence of the tunneling supercurrent. The sample is placed at the center of a cylindrical coil (1 mA $\rightarrow$ 100 μT) thermalized at 4 K (Fig. 4.8a). First, we repeat the I(V) measurements at various fixed $\vec{B}$.

Hypothesis. *The external $\vec{B}$ imposes a phase bias (φ) between S_1 and S_2 and the critical supercurrent across $N'IS$ presents a* $\cos(\varphi/2)$ *dependence. Therefore, we expect a gradual attenuation of the I(V) peak due to the proximity effect as φ is swept from* $0 \rightarrow \pi$ *via external $\vec{B}$.*

Fig. 4.8b presents the I(V) traces taken at various external $\vec{B}$. The decrease in the current amplitude is in line with our expectation. Therefore, we conclude that the loop is intact and our device responds to the $\vec{B}$ as expected. To further investigate the question, we fix the V_{bias} at the positive current peak ($V_{bias} = 12$ μeV) and sweep $\vec{B}$ continuously from 0 μT to 300 μT and then we do the reverse sweep. The periodic modulation of the current with respect to $\vec{B}$ is seen in Fig. 4.8c. Note that the attenuation of the supercurrent is limited to min(I)/I(0) $\approx$ 0.6 and I(0) is restored with abrupt jumps. We interpret this behaviour as the signature of the hysteretic regime where the phase jumps occur whenever $\varphi \geq \pi/2$. The product of the modulation period ($\sim 40\,\mu$T) and the surface area ($\sim 46\,\mu$m) yields a flux threading the loop, $\Phi = 1.84 \times 10^{-15}$ Wb which corresponds to $\sim 0.9\,\Phi_0$. The systematic 10% error encountered here might stem from the lack of precision on the current to magnetic field strength conversion of the coil used in the experiment as well as the marginal error on the surface area calculation.

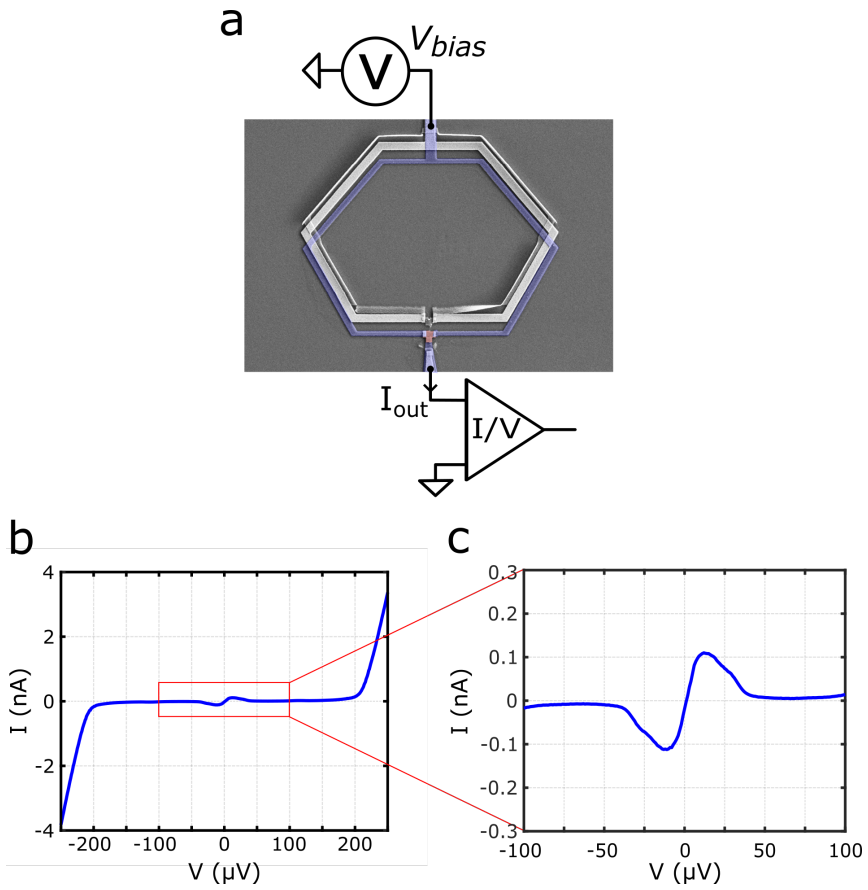

Figure 4.7: ***a.*** *Schematics of the I(V) measurement.* ***b.*** *I(V) curve at T = 50 mK.* ***c.*** *Zoomed in I(V= ±100 μV).*

RF measurements

Having obtained the basic characteristics of our device via DC measurements, we move on to the RF experiments where the device and the resonator chip are bonded together. The system is excited with a sinusoidal tone ($P_{in} = -110$ dBm) at the resonant frequency ($f_r = 575$ MHz). The output power is measured at a predefined sampling frequency and duration.

***$P_{out}(V)$* characterization** The bias tee extension of our resonator circuit enables us to apply V_{bias} on the $N'IS$ junction while measuring the tunneling resistance across it. We therefore have the experimental capability to conduct tunneling spectroscopy measurements on our sample.

Results: Figure 4.9 shows two $P_{out}(V_{bias})$ measurements at T = 50 mK and T = 300 mK. The curves feature typical characteristics of a tunneling spectroscopy as well as some important nuances specific to our device configuration. The coherence peak which occurs at $\pm\Delta$ for ordinary superconductors is now visible at $\pm(\Delta \pm \Delta_g)$ due to the convolution with Δ_g of N'. We find $\Delta \approx 220\,\mu$eV and $\Delta_g \approx 20\,\mu$eV. The flat plateau at low T $\pm(\Delta - \Delta_g)$ at $T = 50$ mK, corresponds to the forbidden states for quasiparticles. More importantly, ZBA peaks are clearly visible at $V_{bias} = 0$ V. Increasing T from 50 mK to 300 mK causes the rounding of the sub-gap conductance due to the thermally populated

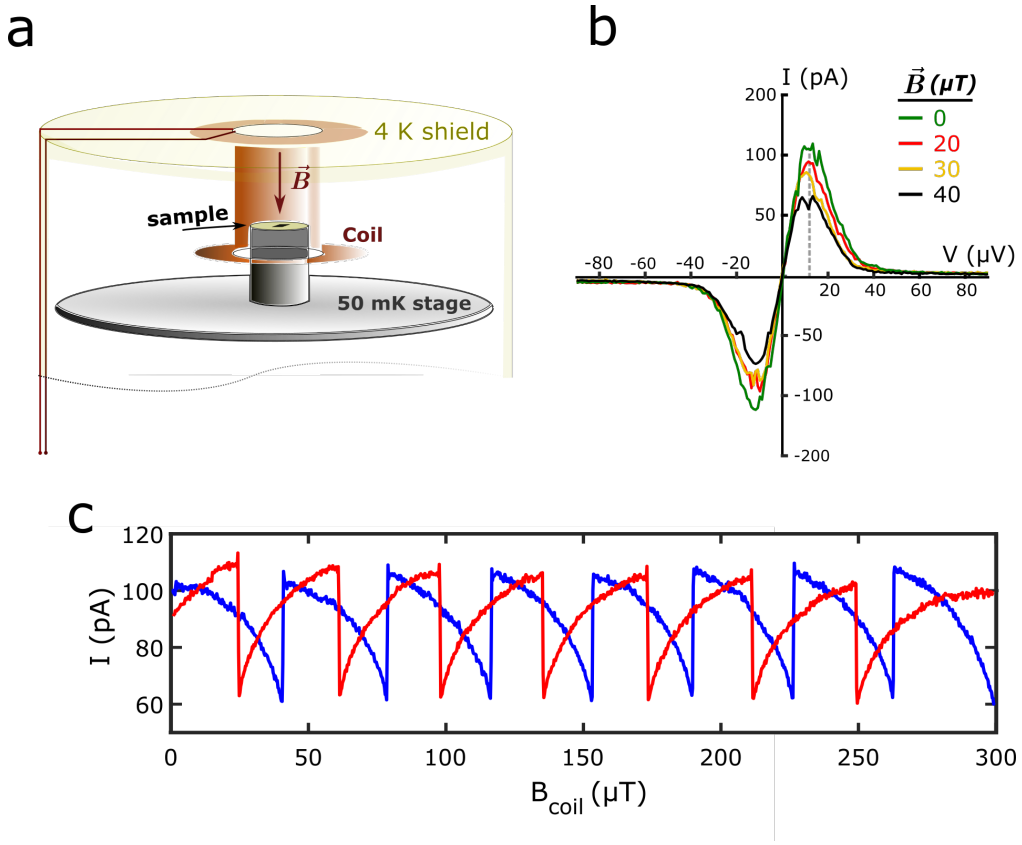

Figure 4.8: ***a.*** *The artistic sketch illustrating the experimental setup used for $I(\vec{B})$ measurement.* ***b.*** *$I(V = \pm 80\,\mu V)$ curves taken at the coherent current peaks at various fixed $\vec{B}$. Incrementing the phase bias $\varphi \to \frac{\pi}{2}$ gradually decreases the proximity effect.* ***c.*** *The periodic modulation ($\sim 40\,\mu T$) of the coherent current peak at $V = 12\,\mu V$. The abrupt phase jumps in the forward (blue) and the backward (red) sweeps are the clear indication of the hysteretic behaviour.*

states above the minigap and the supression of the ZBA conductance ($\sim 14\ dB$) due to the decreasing pair density in N'. In the following sections, we will investigate in detail the temperature dependence of the ZBA peak for thermometry purposes.

$P_{out}(\vec{B})$ characterization Similar to the $I(\vec{B})$ measurement, we expect the modulation of the zero bias conductance with $\vec{B}$. However, this time we need to take into account the transfer function (S_{21}) of the resonator circuit in order to make sense of $P_{out}(\vec{B})$ measurements. Tracking the role of the phase bias (φ):

$$\varphi \to I_c(\varphi) \to E_J(\varphi) \to G(\varphi) \to S_{21}(\varphi) \tag{4.6}$$

we see that φ modulates the Josephson energy, $E_J(\varphi)$ which in return alters the tunneling conductance ($G(\varphi)$). We read the change in $G(\varphi)$ with our resonant circuit via $S_{21}(\varphi)$. The function $S_{21}(G(\varphi))$ at resonance is given as [1]

$$S_{21}(\varphi)\Big|_{\omega=\omega_0} = S_0 - 20\log_{10}(1 + R_0 G(\varphi, T)) \tag{4.7}$$

where S_0 is the constant offset brought by the circuit elements [1] and $R_0 = (\omega_0 R_L C_2^2)^{-1}$.

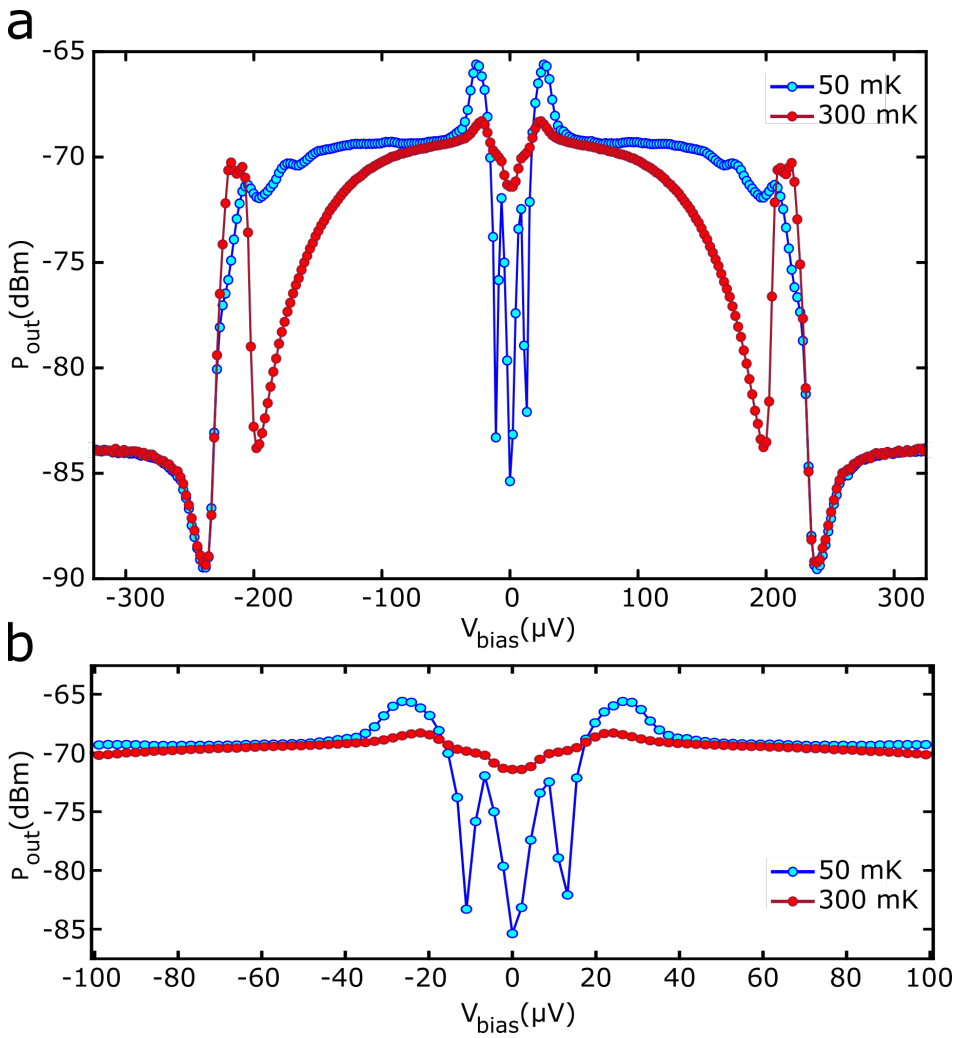

Figure 4.9: ***a.*** *The tunneling spectroscopy of the SQUIPT taken at $T = 50$ mK (blue) and $T = 300$ mK (red). V_{bias} is swept between $\pm 330\ \mu V$ with the increments of $2.2\ \mu V$. At every V_{bias}, P_{out} is sampled at $f_s = 50$ kHz for $t = 200$ ms. Therefore, the data points represent the average of 10^4 samples.* ***b.*** *Zoomed view of the tunneling spectroscopy at $V_{bias} = \pm 100\,\mu V$.*

We see that $S_{21}(\varphi)$ is inversely proportional to $\log_{10} G(\varphi, T)$. The tunneling supercurrent (hence $G(\varphi)$) is maximum at $\varphi = 0$ which marks the lowest value of $S_{21}(\varphi)$. Conversely, $\max(S_{21})$ is reached in principle when $\varphi = \pi(\varphi)$ where the proximity effect is cancelled. Figure 4.10a shows the calculated P_{out} at $V_{bias} = 0$ with respect to Φ with $\beta = 10$. Note the repeating spike pattern as Φ is swept. The phase jumps occur whenever $\varphi \geq \pi/2$.
Results: Fig. 4.10b shows the $P_{out}(\vec{B})$ measurement at T = 50 mK. We probe the device with a sine wave at $f = 575$ MHz and $P_{in} = -110$ dBm. $\vec{B}$ is swept $0\ \mu\text{T} \rightarrow 300\ \mu\text{T}$. P_{out} is sampled at $f_s = 1$ MHz and t = 50 ms (see Sec. 4.5). Therefore, each data point represents the average over 50×10^3 samples. Overall, the data present good agreement with the theoretical curve. We obtain the phase jump period $\sim 40\,\mu$T as the DC measurements.
Determination of β: With respect to $\Phi_x = 0$, the first phase jump always occurs at $\Phi/\Phi_0 \approx 1/4$ in the ideal case. Inserting this in Eq. (4.8), it is seen that the ratio of Φ_x

causing the first jump (called Φ_{in} in Fig. 4.10a) over Φ_0 defines uniquely β as

$$\beta = 2\pi\left(\frac{\Phi_{in}}{\Phi_0} - \frac{1}{4}\right) \tag{4.8}$$

which allows us to extract β from $P_{out}(\vec{B})$ measurements. Hence, we find $\beta \approx 6.3$ for this last sample.

Final remarks: With the first series of measurements, we could obtain the DC and RF properties of our device. The major results are

1. The presence of the proximity effect on N' was confirmed via both I(V) and $P_{out}(V)$ measurements.

2. Δ and Δ_g were obtained via tunneling spectroscopy and the ZBA peak at $V_{bias} = 0$ and its temperature dependence were observed.

3. The $\vec{B}$ dependence of the ZBA peak was obtained in both DC and RF configurations. The RF response to $\vec{B}$ is well understood.

4. The hysteretic behaviour was confirmed via abrupt phase jumps present in both DC and RF measurements of $\vec{B}$ sweep.

5. Overall, the sample looks promising for thermometry measurements.

At this stage, the logical step towards fast thermometry is to conduct real-time relaxation measurements which necessitates a fast $\vec{B}$ source and a synchronous data acquisition. However, given the high inductance of the coil we used, it was impossible to drive $\vec{B}$ faster than 10 Hz. Our fast thermometry trials with averaged measurements using the coil failed (not shown). We concluded that our setup was insufficient for the type of fast experiments we wanted to realize. To circumvent this issue, we converged towards an on-chip flux-biasing solution where we can drive the flux-line with faster pulses in $< \mu$s rise/fall time.

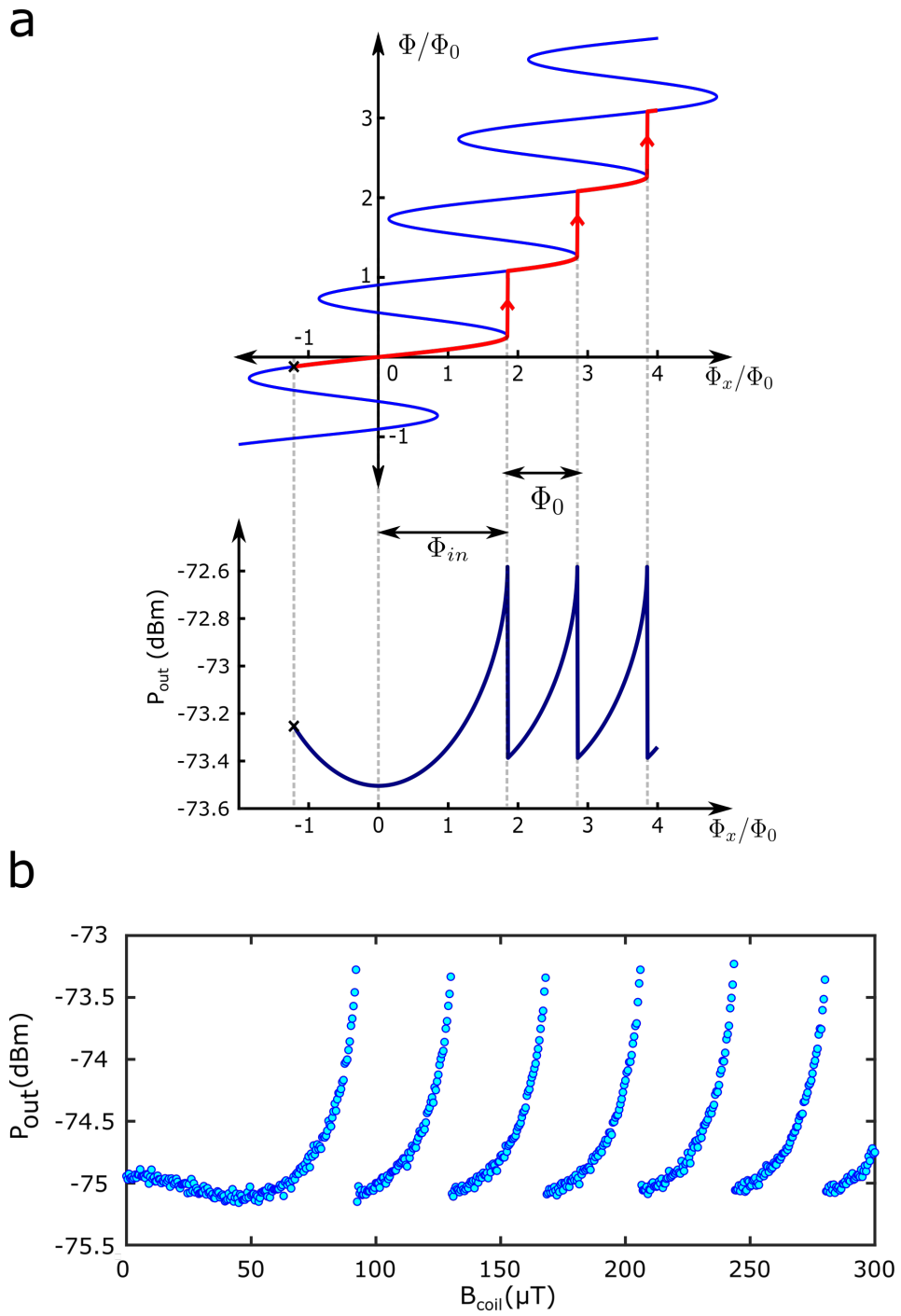

Figure 4.10: ***a.*** *The calculated $\Phi(\Phi_x)$ curve for $\beta = 10$ combined with the expected thermometer response: $P_{out}(\Phi_x)$. The red curve corresponds to a typical trajectory followed by Φ when Φ_x is swept across several phase jumps. The corresponding behaviour is observed as the repeated spikes at the thermometer output which allows the extraction of the screening parameter.* ***b.*** *$P_{out}(\vec{B})$ measurement at T= 50 mK. We extract $\beta \approx 6.3$ from Φ_{in}/Φ_0.*

4.4.2 Device-2: On-chip Inductive Coupling

The inductive coupling is a specific type of coupling where two or more devices interact with each other via shared magnetic flux. The on-chip coupling solutions are ubiquitous and they serve for several purposes, especially in the quantum electrodynamics domain. To name a few applications; inductive coupling provides the frequency tunability of transmons as well as the coupling between them for two-qubit operations [201, 202]. In three wave mixing process, the pump signal and the DC offset to adjust the ω_{pump} are inductively coupled to the SQUID [203].

Our motivation for employing an on-chip flux line is to replace the macroscopic coil with a faster Φ_x source. When connected to a transmission line, the on-chip flux line can carry nano-second range flux pulses to the SQUIPT, a step which is crucial for our fast thermometry experiment. The condition for the correct operation of the rapid flux line is that it must stay in the superconducting regime at all times. This means that the rapid flux line current (I_{RFL}) with sufficient amplitude to generate a phase slip must be smaller than the critical current (I_c) of the flux line. To meet this condition experimentally, we need two pieces of information (1) what is the I_c of the rapid flux line (2) What is $\min(I_{RFL})$ that provokes a phase slip? In other words, what is the mutual coupling (M) between the flux line and the SQUIPT? In the following sections, we present the new device and address the above-mentioned questions.

Geometry. In our next device, we keep the SQUIPT design the same and include a flux line which is positioned at ~ 3 μm from the loop (Fig. 4.11). The flux line is made of Al and has a thickness (width) of 100 nm (2 μm). It is fabricated prior to the SQUIPT via laser lithography and physical vapor deposition.

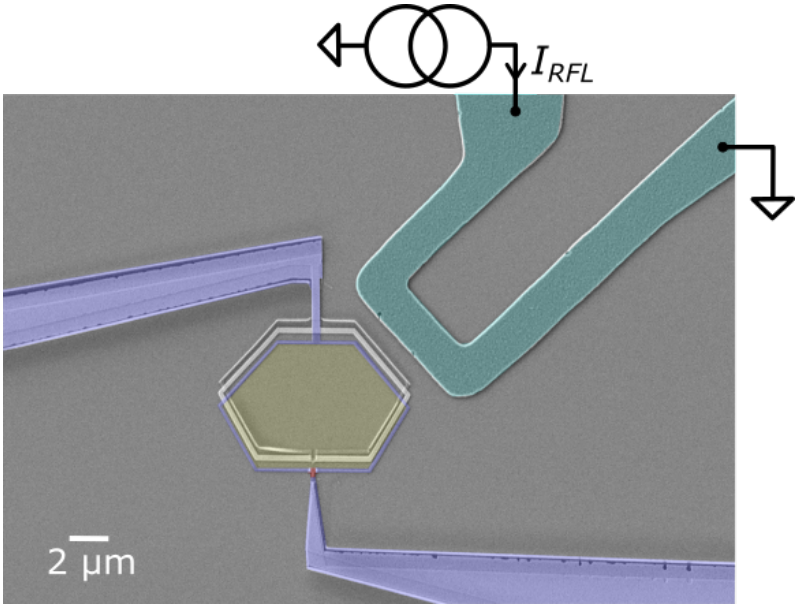

Figure 4.11: SEM view of the SQUIPT (blue) and the rapid flux line (cyan). RFL is connected to a current source at T_{room} and grounded at the sample holder level.

Flux line critical current (I_c). In a four-wire setup, we current bias the rapid flux line and measure the voltage appearing across it. The forward/backward sweeps are shown in Fig. 4.12. We obtain $I_c \approx 740$ μA at T= 50 mK. Having obtained the critical current of

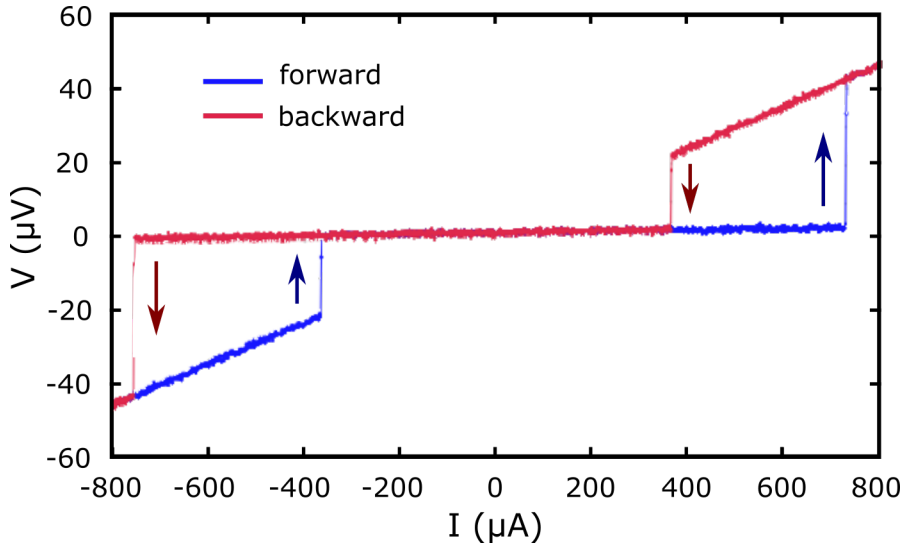

Figure 4.12: V(I) curve of the rapid flux line. The forward sweep is marked in blue. The reverse sweep (red) features a retrapping current $I_R \approx 360$ μA which originates from the thermal hysteresis.

the rapid flux line, we move on to the mutual coupling measurements. In order to have $\Phi = \Phi_0$ induced by I_{RFL}, we require $M = \Phi_0/I_c(T = 50\,\text{mK}) \approx 2.8\,\text{pH}$

Mutual coupling (M).

$P_{out}(\vec{B})$ characterization: We proceed with the RF measurements. As it was the case with the previous sample, the idea is to sweep $\vec{B}$ by applying current $I_{RFL}^{\Phi_x=\Phi_0}$ on the rapid flux line and measure P_{out} simultaneously. The phase slips following the initial one occur at a sweeping period $\Phi_x = \Phi_0$. It is therefore possible to extract the mutual coupling as $M = \Phi_0/I_{RFL}$. In Fig. 4.13, we compare the $P_{out}(\vec{B}, V)$ responses between a $\vec{B}$ sweep with (a) the coil and (b) the rapid flux line. The feature we would like to emphasize is the gradual heating from $I_{RFL} \approx 200$ μA onward in the RFL measurement. The rounding of the subgap conductance and the disappearing ZBA peak clearly demonstrate this effect. We observe no phase slip on the vertical slice at $V_{bias} = 0$ V. At this stage, it is possible to draw following conclusions from the experiment

1. Previously we had measured $I_c^{RFL} \approx 740$ μA. The onset of Joule heating at $I_{RFL} \approx 200$ μA indicates that the cause lies somewhere else, most likely at the heating of instruments. A steady-state current $I_{RFL} = 200$ μA leads to $\sim$ 900 nW of dissipation on the 20 dB attenuator residing at the mixing chamber stage. This might eventually lead to the overheating of the sample chip above the T_{base} via heat current.

2. We could not observe the phase slips provoked by the flux line. Therefore, our

method fails to obtain the mutual coupling.

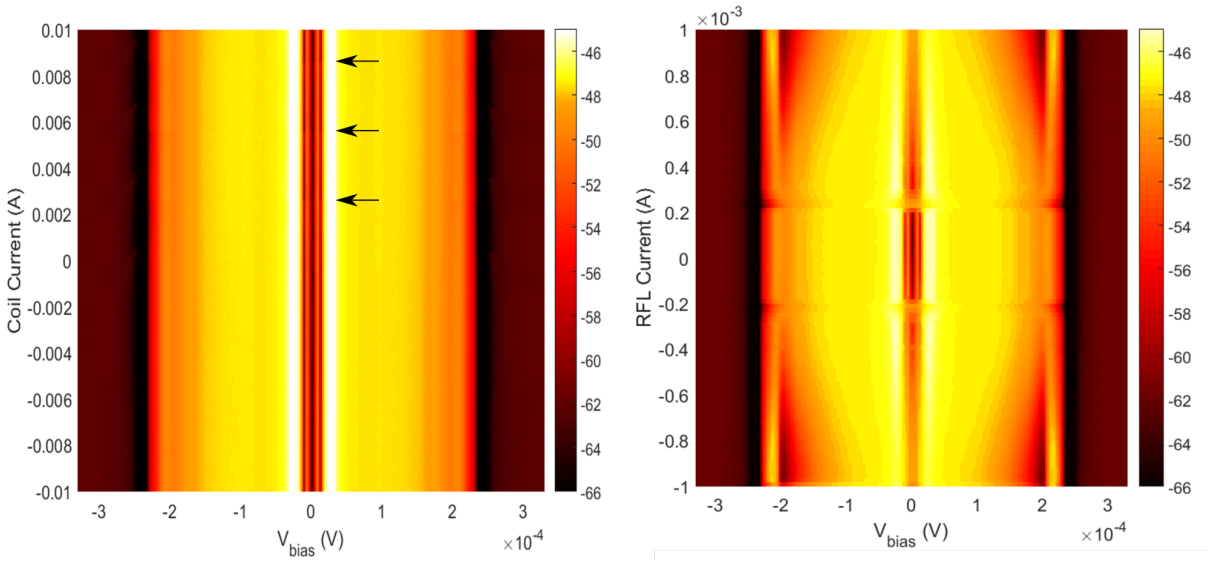

Figure 4.13: 2-D color maps of the SQUIPT combining two measurements: P_{out} is measured (color scale) while V_{bias} (horizontal) and the current on the flux source source (vertical) are swept. The figure compares the responses of the ***a.*** *coil and* ***b.*** *RFL driven measurements. Black arrows point to the phase slip events.*

2. Measurement combining the coil and the rapid flux line: We have both the coil and the RFL operational. Therefore, we can come up with a combined measurement scheme to obtain the mutual coupling (Fig. 4.14). Our strategy is as follows:

1. Sweep the coil up to $\varphi \lessapprox \pi/2$
2. Hold the coil at $\varphi \lessapprox \pi/2$ and let the measurement free run to make sure that the phase bias is stable.
3. Send a μs range current pulse on the RFL.
4. Increase the pulse amplitude until a phase slip occurs.
5. Ramp the coil current down and up again to reset the SQUIPT.

As we have the information on the phase periodicity for the coil, we also know precisely the phase bias φ_{coil} we impose on the SQUIPT. We can therefore make the correspondence between the additional Φ provided by RFL to complement the phase jump and the current pulse amplitude to deduce the mutual coupling.
Result: We repeat the measurements at three phase bias points, $\varphi_{bias} = (0.4, 0.3, 0.2)\pi$. Each time, a current pulse with the threshold value $I_{RFL} \approx (80, 156, 230)$ μA systematically generates a phase slip. For example, in the case of $I_{RFL} = 80\,\mu$A, the current pulse

on the rapid flux line (I_{RFL}) complements $\varphi = 2\pi\Phi/\Phi_0 = 0.1\pi$ from which we deduce $\Phi \approx 1.033 \times 10^{-16}$ Wb. Inserting Φ and I_{RFL} in $M = \frac{\Phi}{I_{RFL}}$, we obtain M≈ 1.3 pH.
Conclusion: Obtaining $M \approx 1.3$ pH points out an important design flaw in our device. The flux line needs to withstand I = Φ_0/M = 1.6 mA for a phase quantum which is largely beyond $I_c = 740$ μA. This clearly indicates that we need to change the design so as to improve the mutual coupling. In the following section, we will address the question on improving the coupling and introduce the new design.

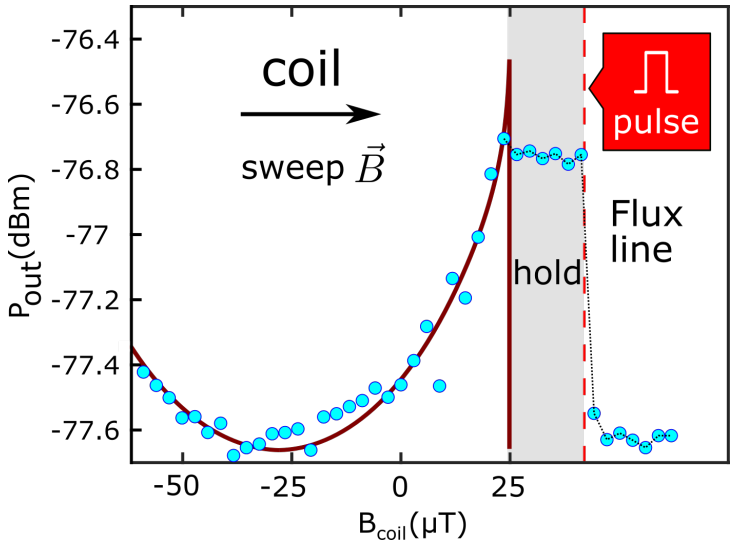

Figure 4.14: Mutual coupling measurement combining the coil and the flux line. Using the coil, the phase is swept up to a given φ. Next, we let the measurement free fun to check the stability of the phase point. The slip is then provoked by the pulse of a fixed amplitude sent on RFL at a time t highlighted by the vertical dashed red line.

4.4.3 Final design

Mutual coupling (M) estimation. In our previous design, the RFL was positioned somewhat arbitrarily with respect to the SQUIPT loop inspired by the earlier work of Claudon et al [204]. Eventually, we observed that our device suffered from the insufficient mutual coupling. To alleviate this problem, we adopt a more rigorous approach for our next device. In a series of calculations based on the Biot-Savart law of classical electromagnetism, we parameterize the device dimensions in order to obtain the desired mutual coupling. The flux threading the loop is written as

$$\Phi = \iint \vec{B} \cdot \vec{ds} \tag{4.9}$$

inserting Biot-Savart law for a straight wire ($B = \frac{\mu_0 I}{2\pi R}$)

$$\Phi = \int_0^x \int_{y_0}^y \frac{\mu_0 I}{2\pi y'} dx dy' \tag{4.10}$$

which yields

$$\Phi = \frac{\mu_0 I}{2\pi} x \ln\left(\frac{y}{y_0}\right) \tag{4.11}$$

Finally, isolating the left hand side in mutual coupling, we obtain

$$M = \frac{\Phi}{I} = \frac{\mu_0 x}{2\pi} \ln\left(\frac{y}{y_0}\right) \tag{4.12}$$

Figure 4.15 shows the 2D contour plot of the mutual coupling with respect to the device dimensions. Taking into account the hexagonal shape of our loop, we estimate $M \approx 10.5$ pH for the nominal values of $x = 30\ \mu m$ and $y = 10\ \mu m$ at a fixed distance $y_0 = 2\ \mu m$ from the RFL center line. Recalculating the I_{RFL} for a phase slip, we find out that $M \approx 10.5$ yields $I = \Phi_0/M \approx 197\ \mu$A for a single phase slip which we consider safe for the superconducting regime.

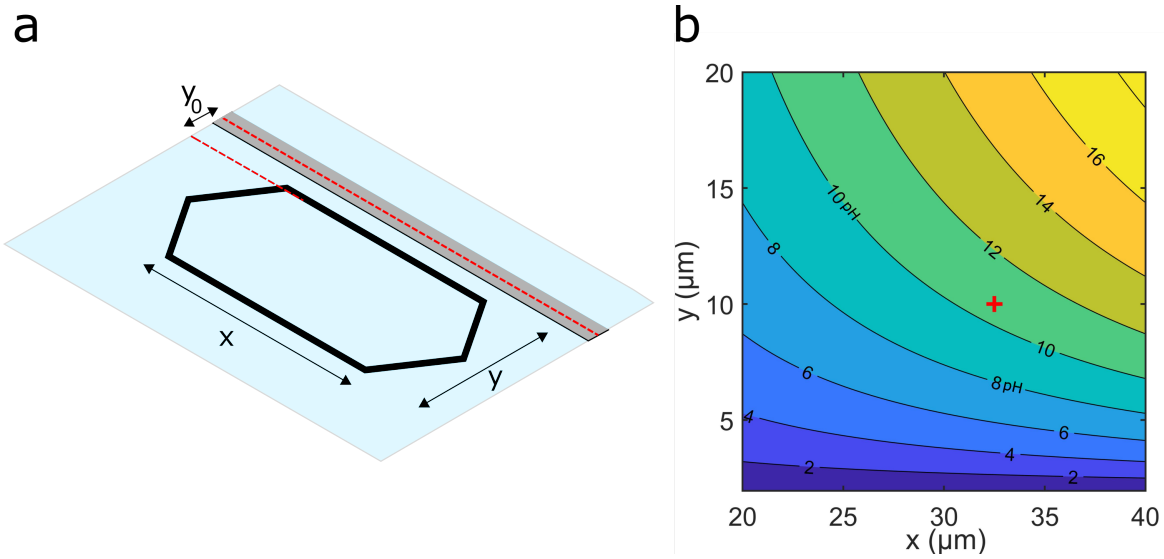

Figure 4.15: Mutual inductance estimations (a) drawing shows the x-y directions used in calculations and $y_0 = 2\ \mu m$, fixed distance from RFL (b) Contour plot demonstrating the mutual inductance as a function of loop dimensions. The estimation of M (red cross) takes into account the hexagonal shape of the sample

Device geometry. Based on the mutual coupling calculations, the new SQUIPT becomes bigger especially in the direction of the RFL (Fig. 4.16). The main rectangle is $30\,\mu\text{m} \times 10\,\mu\text{m}$. Including the side lobes, the total surface area amounts to $\sim 330\,\mu\text{m}^2$. The T-shaped normal island is $760\,\text{nm} \times 240\,\text{nm} \times 35\,\text{nm}$ and has a $\sim 120\,\text{nm}$ overlap with the superconducting leads on both ends. The bottom extension which forms the tunnel junction is $\sim 180\,\text{nm} \times 220\,\text{nm}$. The material choice and the thicknesses for the SQUIPT loop are the same as the previous designs. The superconducting parts are made of Al whereas the normal metal is of copper. We used niobium for the rapid flux line due to its higher supercurrent density. The RFL is 500 nm wide and 100 nm thick. Its central line is $1.9\,\mu$m away from the loop which leaves enough space for the shadow evaporations.

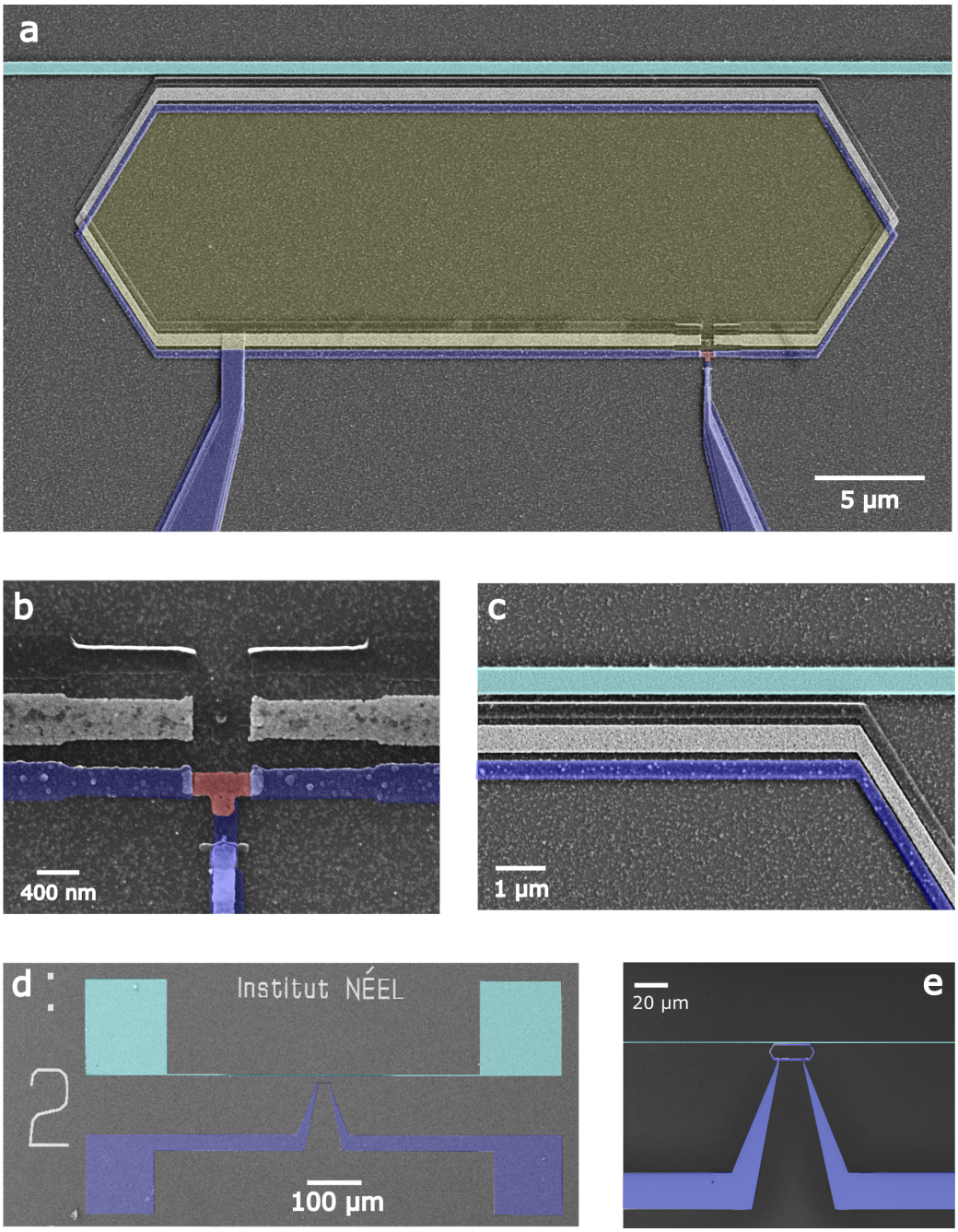

Figure 4.16: The false coloured SEM view of the SQUIPT device. The superconducting electrodes are marked in blue, the absorber normal metal in red and RFL in cyan. In ***b.*** *and* ***c.*** *the shadow depositions are clearly visible.* ***d.*** *The view of the single device on a sample chip. The contact pads are* $150\,\mu m \times 150\,\mu m$.

$P_{out}(\vec{B})$ characterization

Mutual coupling. The operation of RFL as a reliable fast flux source hinges on a sufficient mutual coupling with the SQUIPT loop. To test our estimation on M for the new device geometry, we connect the RFL in a DC current source and measure P_{out} while I_{RFL} is being swept slowly. Figure 4.17a shows the traces of such a measurement at T_{bath} = 50 mK, 200 mK and 400 mK within the sweeping range of 0 − 1 mA. From a phase slip period in current $I_{RFL} \approx 170 \pm 5$ μA, we extract $M \approx 12.1 \pm 0.4$ pH, that is, 15 % higher than estimated from the Biot-Savart calculation. We attribute this to a slightly smaller distance between the SQUIPT and the RFL, of approximately 1.9 μm instead of 2 μm by design and to the fact that the I_{RFL} has a finite distribution along the width whereas the theoretical calculations consider an ideal line.

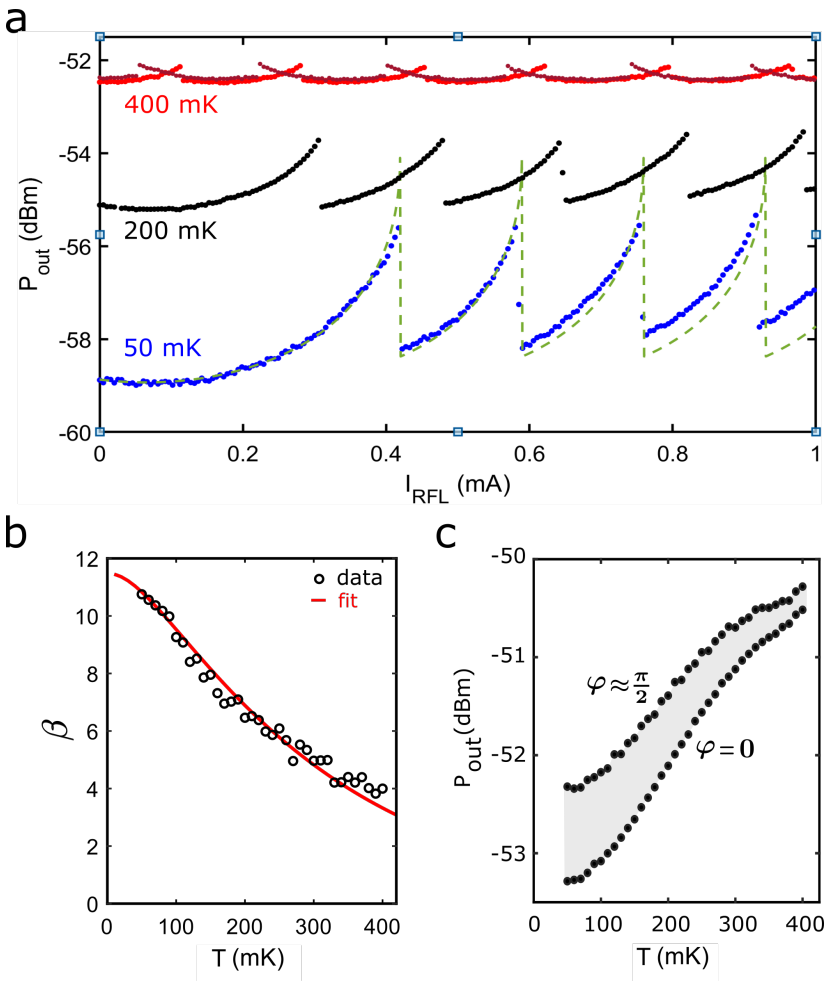

Figure 4.17: ***a.*** *$P_{out}(I_{RFL})$ measurement at T = 50 mK, 200 mK and 400 mK. The calculated response at T = 50 mK is shown in dashed green. The divergence of the data from the theoretical curve at high RFL currents points to a residual heating problem.* ***b.*** *$\beta(T)$ measurement between 50 mK and 400 mK. The fit is computed by Usadel formalism which yields $I_c(T)$ and we fix L = 0.6 nH, E_{Th}/Δ = 0.12 and R_N = 1.3 Ω* ***c.*** *$P_{out}(T)$ measurements at $\varphi = 0$ and $\varphi = \pi/2$. The shaded area corresponds to all possible temperature readouts for a given φ.*

$\beta(T)$ measurement Although we do not have direct access to I_c via measurements, we can extract β at a given T from the ratio of Φ_{in}/Φ_0 as Eq. (4.8) suggests. We repeat the $P_{out}(I_{RFL})$ sweeps at every 10 mK between 50 mK - 400 mK. We obtain $\beta(T = 50\,\text{mK}) \approx 10.8$ which is ~ 70 % greater than the β found in the previous design (Fig. 4.17b). This is somehow an expected result. The device perimeter now amounts to ~ 74 μm compared to ~ 19 μm in the previous design. Therefore, both the geometric (L_{geo}) and the kinetic (L_{kin}) inductances have higher values. The 3.9 fold increase in β is somewhat counterbalanced by the longer N size (200%) which yields a smaller I_c. Overall, $\beta(T)$ follows a very similar trend to $I_c(T)$ of a typical SNS junction and decreases by ∼70% of $I_c(T = 50$ mK) at T= 400 mK.

The Calibration curve $P_{out}(T)$: Our thermometer probes $G(T)$ of the ZBA peak and provides P_{out}(dBm) via $S_{21}(T)$. To convert the power measurement to temperature information, we extract $P_{out}(\varphi = 0)$ and $P_{out}(\varphi = \pi/2)$ from $P_{out}(\vec{B})$ curves at every T and assume that sample is thermalized to T_{bath}. The $P_{out}(T)$ plot gives us a family of isophase curves which we can use as the calibration curve (Fig. 4.17c). Hence, at $\varphi_{bias} = 0$, our thermometer features $\mathbb{R} \approx 0.01$dB/mK of responsivity in the linear regime between T = 100 mK and T = 280 mK. Below T = 100 mK, P_{out} starts to saturate due to the heating and the input noise of the HEMT amplifier. The correct temperature read-out from the power measurements is not straightforward. One needs to make sure that φ_{bias} is fixed during the data acquisition. Moreover, the RF measurement properties such as the sampling frequency have a direct impact on the calibration curve. We will investigate the role of RF setup in the following sections.

$P_{out}(V)$ characterization As it was the case for the first sample, we run a spectroscopy measurement on our device. V_{bias} is swept between ± 330 μV with 1.1 μV of resolution. This time we sample the data at $f_s = 2$ MHz to be in line with the future fast measurements. Figure 4.18 shows two measurements done at T = 50 mK and T= 400 mK. The ZBA peak decrease by ~ 2.25 dB between two temperatures. From the curves, we extract $\Delta = 210 \pm 5$ μeV in the superconducting electrode at T= 400 mK. The minigap of the proximitised N is found ~ 29 μeV.

4.5 Real Time Detection

At the current stage of our experiment, our achievements are (1) a SQUIPT device operating in the hysteretic regime with $\beta(\text{T} = 50\text{mK}) \approx 10.83$, (2) the ZBA peak which features $\mathcal{R} \approx 0.01$ dB/mK of responsivity and (3) a rapid flux line which is inductively coupled $M \approx 12.1$ pH to the SQUIPT loop. Having obtained the necessary ingredients, we now proceed to the real-time detection of phase slips.

Measurement Protocol for Detecting Phase Slips The real-time aspect of phase slip detection requires strict control of the timing of events. For this reason, we use a triggered measurement scheme in which the occurrence of a phase slip and the data

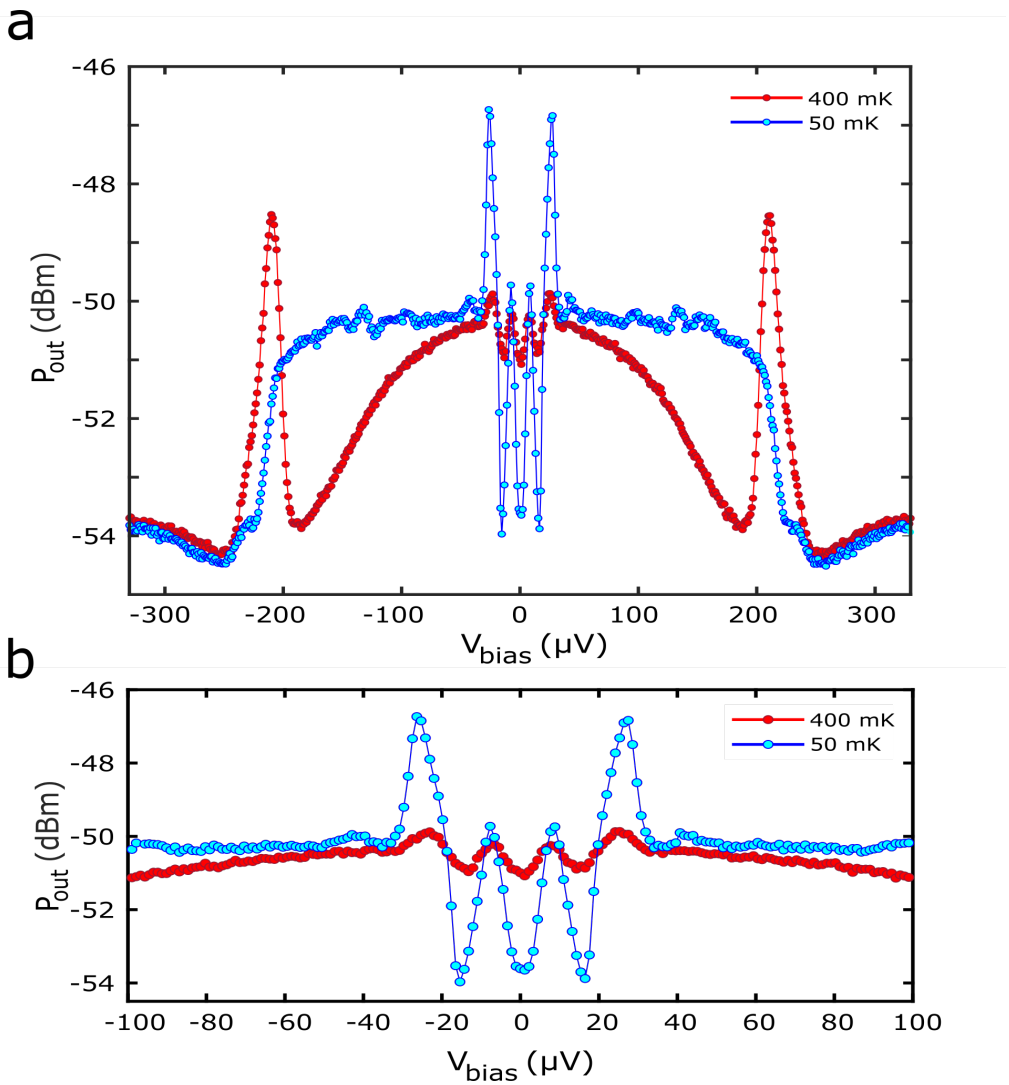

Figure 4.18: ***a.*** *The tunneling spectroscopy of the SQUIPT taken at T = 50 mK (blue) and T = 400 mK (red)* ***b.*** *Zoomed view of the tunneling spectroscopy at* $V_{bias} \pm 100\,\mu V$

acquisition is orchestrated by an auxiliary pulse (Fig. 4.19). A pair of Aeroflex 3025 signal generator and Aeroflex3035c digitizer is used as a vector network analyzer. Both modules are mounted on the same PXI rack. The pulse signal on the RFL is provided by the second channel (CH2) of the Siglent6032 arbitrary wave generator. We use the first channel (CH1) as a trigger. All devices share a 10 MHz reference clock for a synchronous operation. A typical detection experiment takes place as follows:

1. The signal generator (Aeroflex 3025) generates a continuous sine wave at fixed frequency and power.

2. The digitizer (Aeroflex 3035c) operates in stand-by mode, waiting for the trigger to start measuring at a predefined sampling frequency and duration.

3. The arbitrary wave generator: at 2 kHz rate, Channel 2 (AWG:CH2), sends a trigger pulse simultaneously to the digitizer and AWG:CH1.

4. The digitizer starts recording data, typically at sampling frequency $f_s = 2$ MHz and during 500 μs.

5. 20 μs after the trigger signal, AWG:CH1 sends a 70 μs pulse to the rapid flux line, which generates thus a flux pulse and induces a phase slip.

We repeat the above procedure and average over a large ($\sim 10^5$) number of individual phase slips, to increase the signal-to-noise ratio.

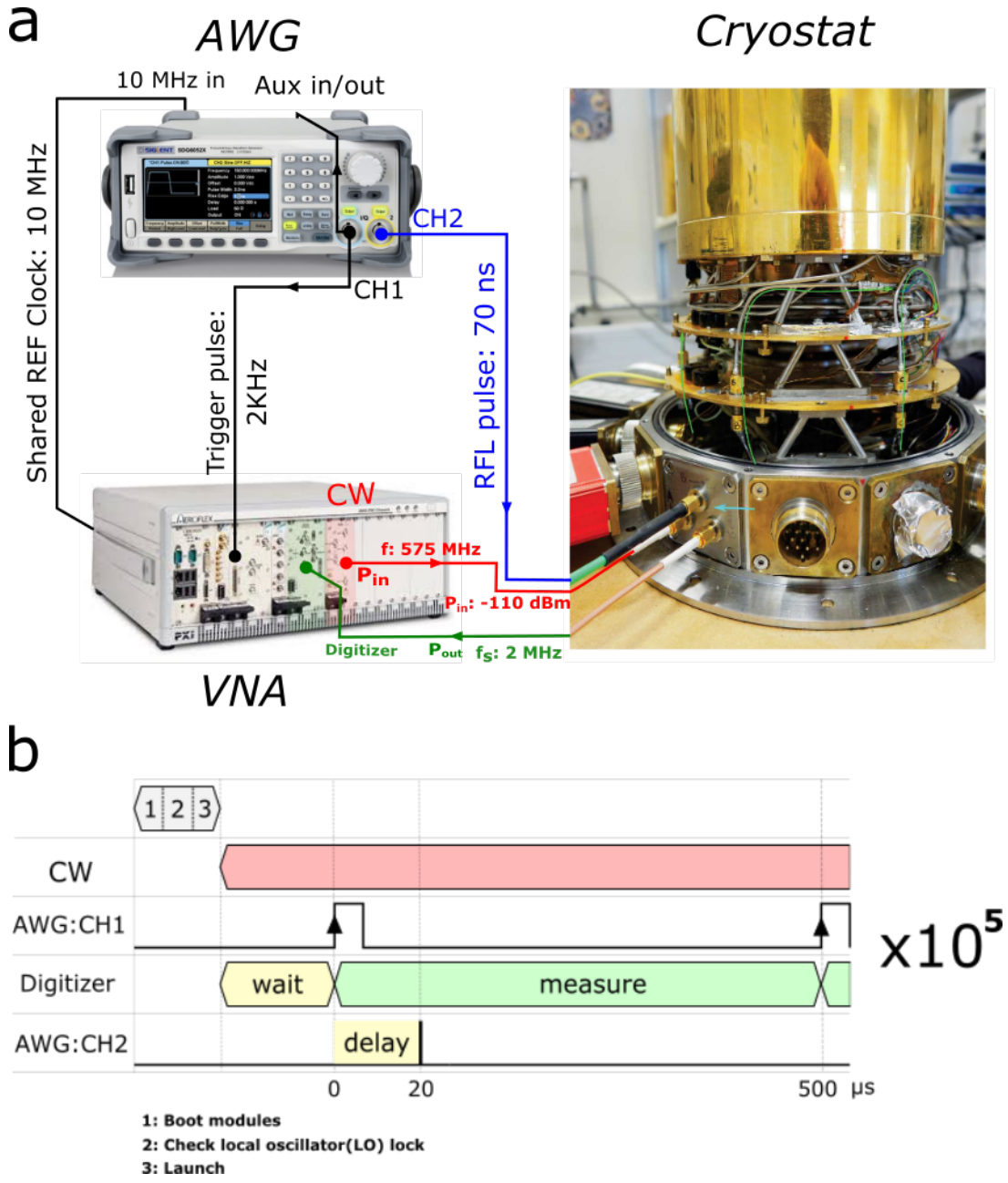

Figure 4.19: ***a.*** *The device setup and the cabling diagram. We have three RF lines dedicated to the input signal (P_{in}), the readout signal (P_{out}) and RFL. P_{in} and P_{out} are referenced to the sample.* ***b.*** *Timing diagram of a single repetition of the real-time measurement.*

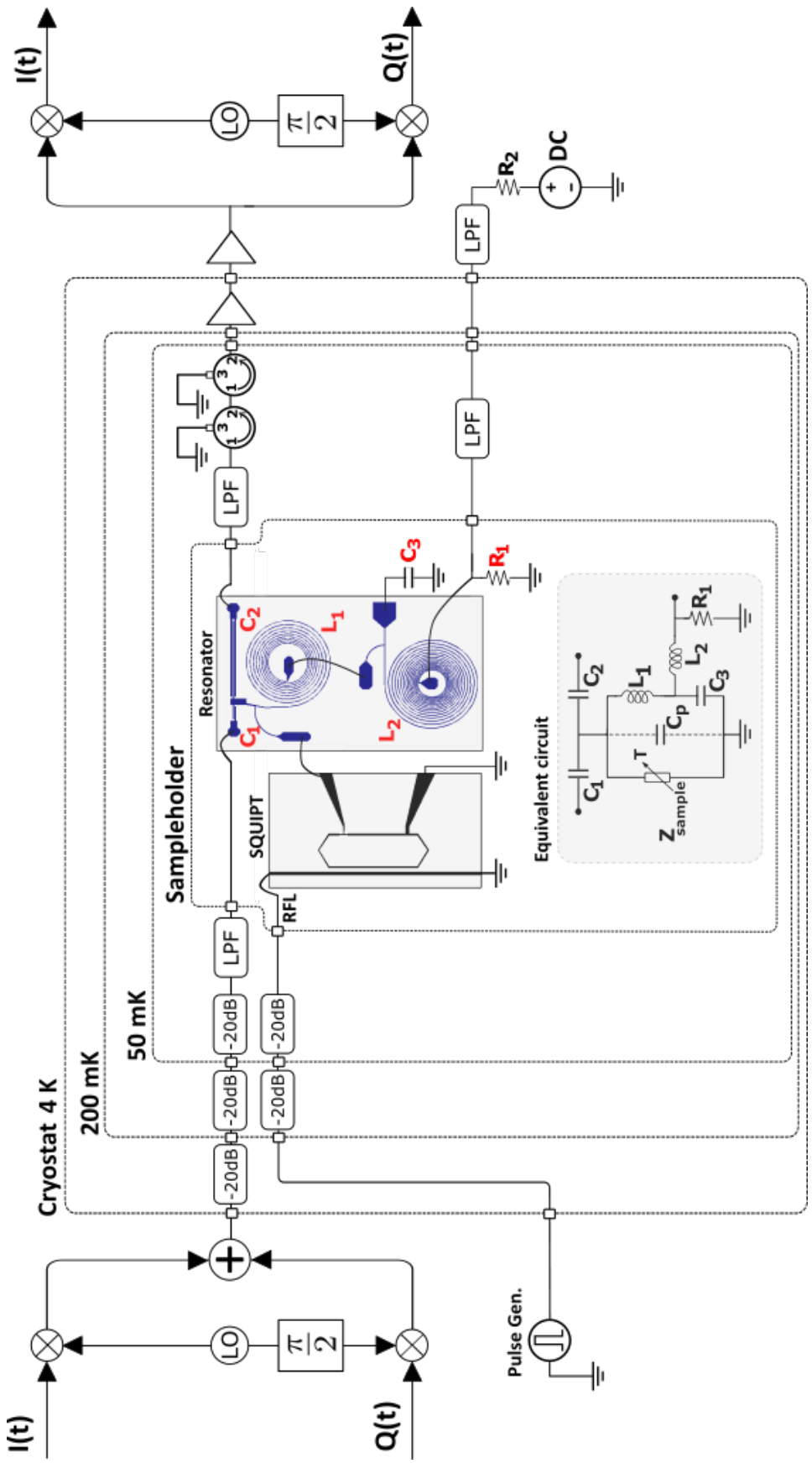

Figure 4.20: Experimental microwave setup diagram, including the drawing of the equivalent electrical circuit of the tunnel junction coupled to the resonator. The incoming signal is attenuated at different temperature stages and low pass filtered (LPF), with a cutoff frequency $f_c = 780$ MHz. The rapid flux pulses are applied through another coaxial line, with a total -40 dB attenuation. Two circulators (shown as grounded circles) provide a total 40 dB isolation between the sample and the low noise amplifier (LNA) residing at 4K stage. The low noise amplifier (LNF-LNC0.3_14A) and a secondary amplifier (Mini-Circuits ZX60-V63) at room temperature provide ~ 60 dB of gain.

Sampling frequency A real-world signal conveys information on the behaviour of a given physical system. Therefore, it is of continuous nature in most of the cases. On the other hand, the experimental tools used by an experimentalist for recording and treating these signals live in the digital realm. Thus comes the question of how to represent a continuous function $f(t)$ by a sequence of sampled data $f[n]$ without any loss of information. In the domain of digital signal processing, the question is answered by the Nyquist-Shannon sampling theorem [205] which states that a function f(t) with a bandwidth B can be fully reconstructed with any sampling rate f_s, fulfilling the condition $f_S \geq 2B$. Considering the fact that we are aiming to resolve in real-time the thermal relaxation following a phase slip, the above-mentioned theorem therefore sets the minimum f_s for our experiment (Fig. 4.21). The relaxation dynamics of the temperature in N is governed by the electron-phonon coupling which is faster than exponential decay in the initial stage. However, for the ease of calculations on f_s it is safe to assume a decaying exponential $f(t =)e^{-t/\tau}$ with $\tau = 2\,\mu s$. Applying Fourier transform $\mathcal{F}\{f(t)\}$, the magnitude in the frequency domain takes the form $|F(\omega)| = 1/(\sqrt{\omega^2 + (1/\tau)^2})$. It should be noted that in principle the Nyquist-Shannon theorem applies to the bandlimited signals. We therefore introduce a cutoff condition as $f_c = 0.1\,max(|F(\omega)|)$ which yields a one-sided bandwidth $B =$ 395 kHz. So, it is sufficient to set 790 kHz to avoid aliasing. Overall, the Nyquist-Shannon theorem elucidates the required sampling frequency and rather falls within the framework of communication theory. However, from an experimentalist's point of view, more datapoint means more confidence on a given measurement. That is why we would like to increase f_s as much as possible. Next, we investigate what sets the upper limit for f_s .

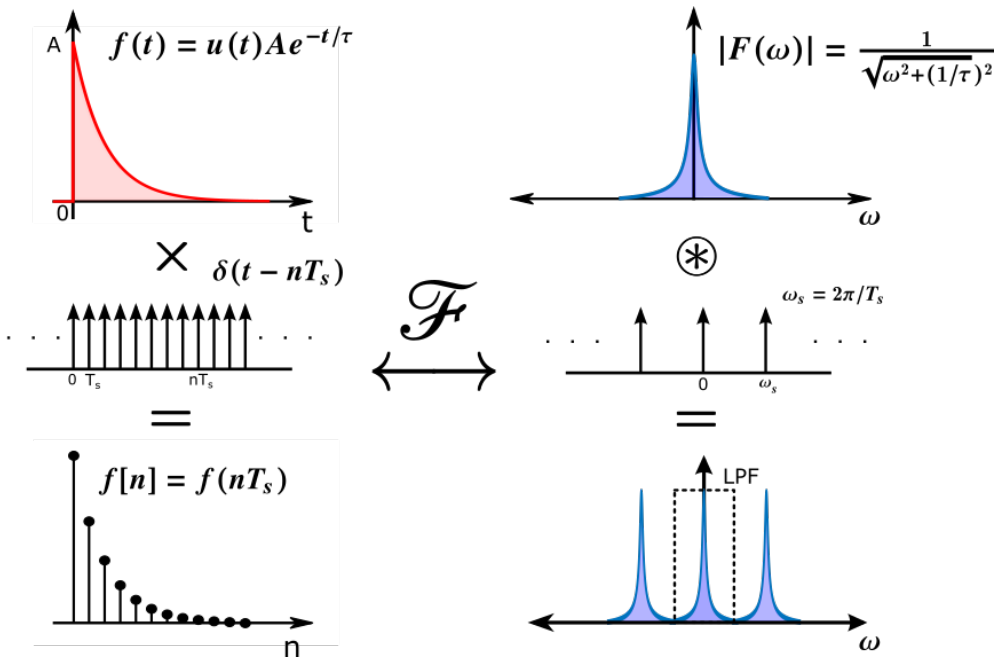

Figure 4.21: The sampling theorem in a nutshell. Time and frequency domain equivalence of the signals and the operations are shown in left and right columns, respectively.

Trade-off between f_s and $\mathcal{R}$ In the previous section, we assumed that f_s was an adjustable parameter defined by the user. In fact, this is an illusion because f_s is physically determined by the data acquisition hardware. The workaround to modify f_s is that whenever the user sets f_s, the device software (1) introduces a downsampling factor M and resamples the digitized sequence with a period M such that $g[m] = f[nM]$ (2) readjusts the cutoff frequency of the anti-aliasing filter to the new f_s. The combination of downsampling and filtering is called decimation. Decimation allows the user to adapt the measurement bandwidth to his/her needs. By reducing the measurement bandwidth, we limit the noise power present in the data which increases the dynamic range (Fig. 4.22). This is called the processing gain. In Fig. 4.23, we present several $P_{out}(T)$ curves with f_s ranging from 50 kHz to 4 MHz. It is clear that as we increase f_s, the noise floor (dynamic range) increases (decreases) and the relative contribution of the noise power in the total measured power increases. We are therefore faced with a trade-off between f_s and $\mathbb{R}$. In our experiments, a maximum $f_s = 250$ MHz is set by the Aeroflex 3035c digitizer card which, in the default settings, would result in a highly oversampled and noisy measurement. Thus, we opt for $f_s = 2$ MHz which we find to be the optimum compromise.

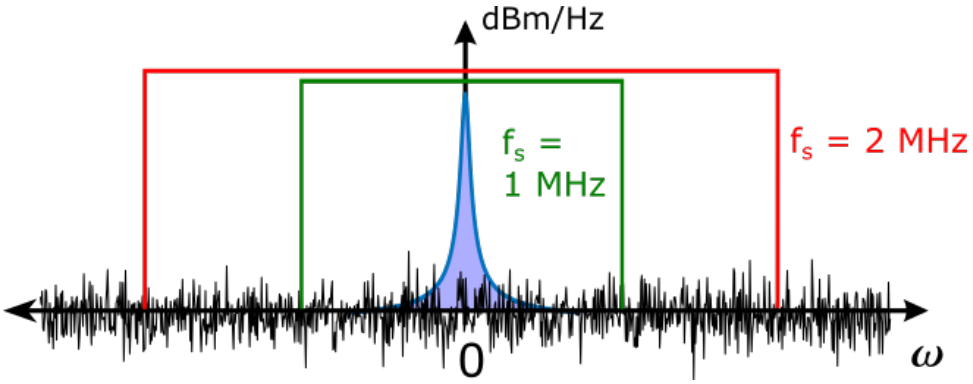

Figure 4.22: The power spectral density plot demonstrating the baseband signal together with the bandlimited noise power in two cases: f_s = 1 MHz (green) and f_s = 2 MHz (red). The larger sampling frequency leads admits more noise in the system.

Noise floor The real-world radio receivers measure noise which emanates from various sources. The sum of all unwanted signal in the absence of the desired input corresponds to a signal level denoted as the noise floor. At $T_{room} = 290$ K, the ultimate noise floor of the receiver is determined by the thermal noise ($P_{noise} = k_B T B$) of the 50 Ω termination which yields $NF = -174$ dBm within 1 Hz. Including the measurement bandwidth, we can formulate the noise floor as

$$NF = -174 + 10\log_{10}(B[Hz]) \tag{4.13}$$

Therefore, with $f_s = 2$ MHz we obtain $NF \approx -111$ dBm. In Fig. 4.24 we depict the major noise sources in our transmission line and the corresponding noise floor with respect to the measurement bandwidth. The dominant contribution comes from the low

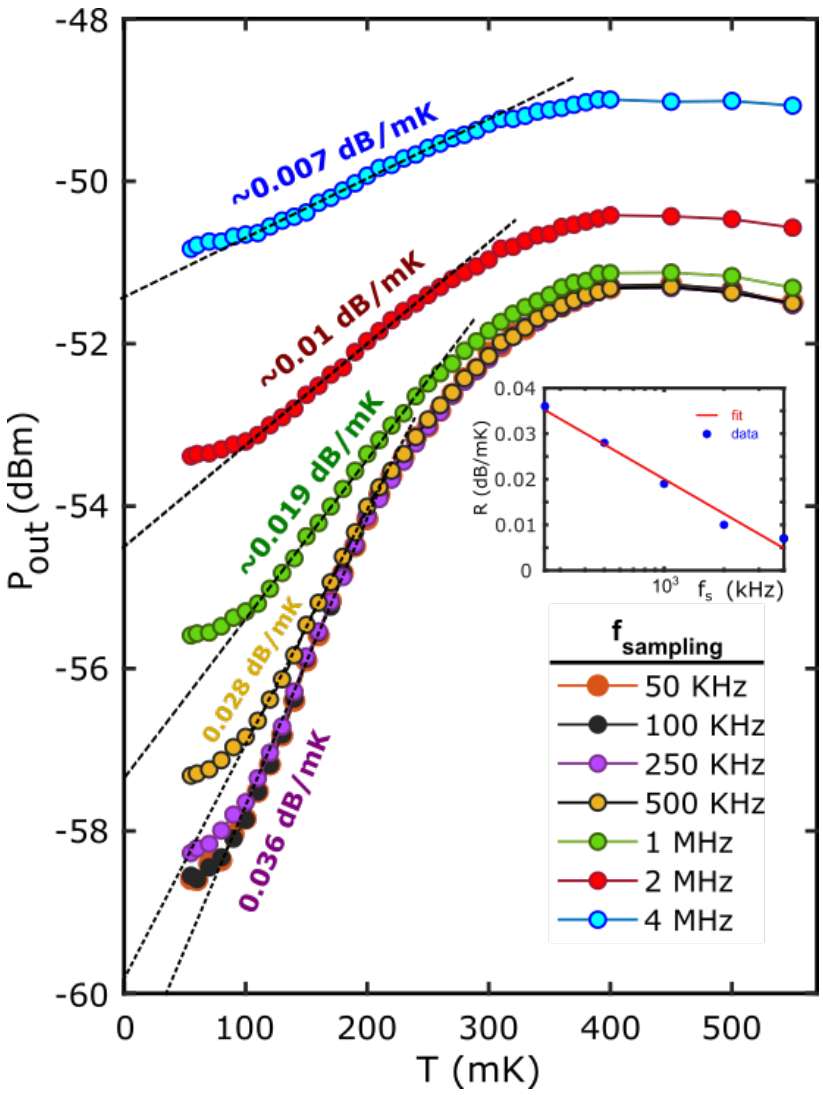

Figure 4.23: $P_{out}(T)$ curves at various sampling frequencies. The trade-off between f_s and $\mathbb{R}$ is remarkable. $\mathbb{R}(f_s)$ extracted from the main figure together with the fit $\mathbb{R} = 0.09574 + 0.02525 \log_{10}\left(\frac{1}{f_s}\right)$ is shown in the inset. The systematic flattening of the curves below $T = 100$ mK stems from the saturation due to the noise floor.

noise HEMT amplifier situated at 4K stage. We follow the procedure described in the Methods section of Ref. [3] to extract the effective noise temperature of it. Basically, the method consists of cancelling the noise emanating from the sample by slightly detuning the probe signal frequency off resonance and applying a finite V_{bias} to position the probed energy level oustide ZBA peak. Next, we measure the standard deviation of the input noise which is dominated by the 4K amplifier as a function the input power. Fitting the curve with a single independent variable, we extract the $T_{noise} \approx 6.2$ K.

Signal-to-Noise ratio (SNR): Having defined the noise floor, the signal-to-noise ratio (SNR) is simply the ratio of the input signal to the noise floor. In our experiment, a typical signal with $P_{in} = -110$ dBm, passing through the resonator circuit S_{21} and the amplification chain $(\sim 62\,)$dBm reaches the digitizer at $P \approx -61\,$dB. Compared to the

$\mathrm{NF}(\mathrm{f_s} = 2\mathrm{MHz}) = -54.1\,\mathrm{dBm}$, we have a $SNR < 1$. We will therefore have to repeat the measurement and do ensemble averaging which improves the SNR by $\sqrt{N}$ where N is the number of repetition.

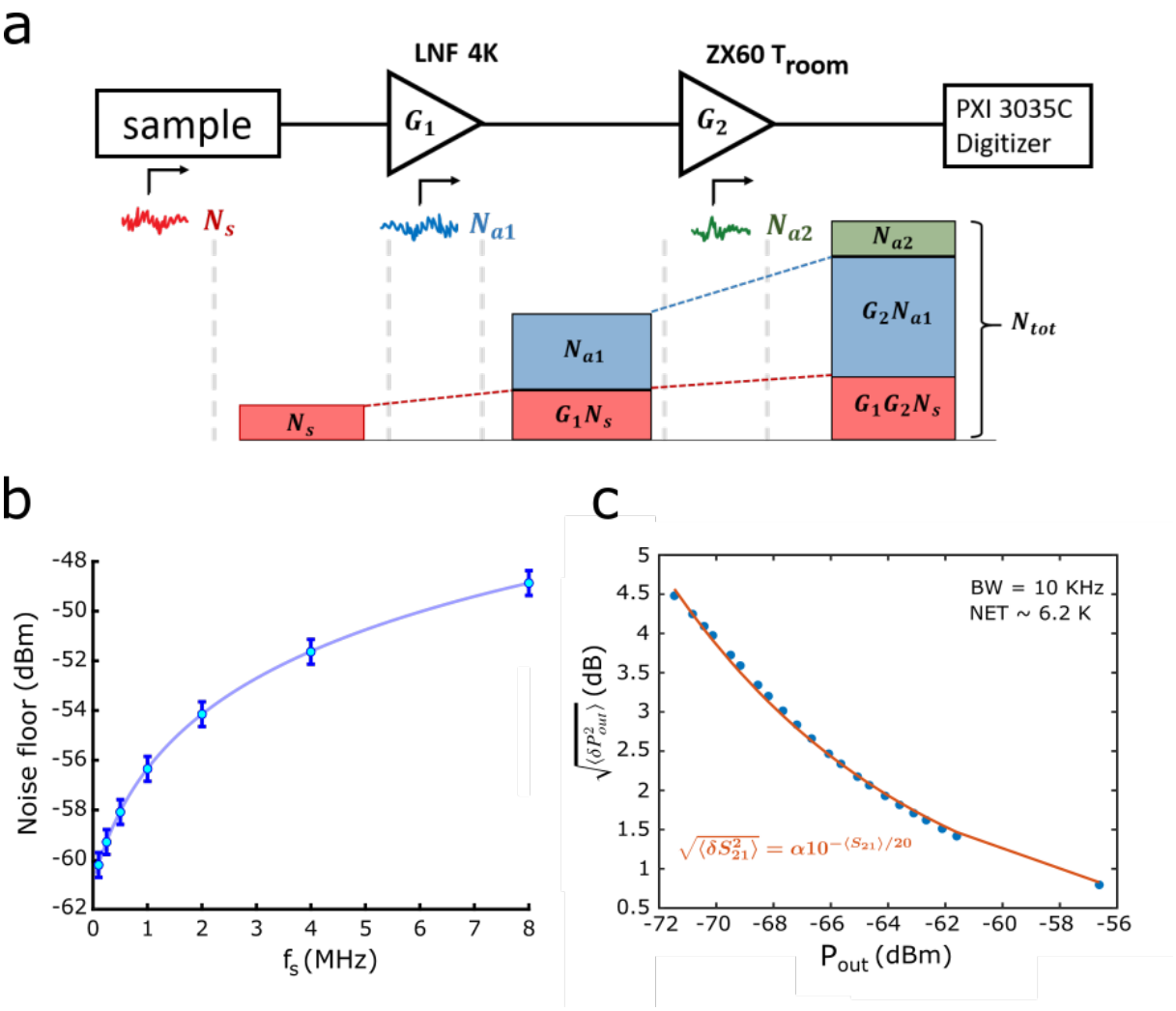

Figure 4.24: ***a.*** *The sketch showing the cascaded noise at the digitizer input. The major contribution originates from the electronic noise of the 4K HEMT amplifier.* ***b.*** *Calculated noise floor of the digitizer as a function of the sampling frequency. The error bars represent the imprecision in the total amplification gain.* ***c.*** *Noise measurement as a function of P_{in} at BW = 10 kHz yielding NET ≈ 6.2 K.*

Threshold amplitude for a phase slip. The minimum pulse amplitude necessary for generating a phase slip should be determined at every measurement temperature before the real-time detection experiment. Because the on-chip flux line, which is connected to the transmission line via wire bonds, is not impedance matched and the mismatch loss is unknown, the pulse amplitude cannot be determined a priori. For this reason, we employ an empirical approach in which we apply square-wave signals with increasing amplitude, until a phase slip is observed. The square-wave width is set to 100 μs with $t_{rise} = t_{fall} = 3$ μs to facilitate the slip detection and P_{out} is measured during 200 μs. Figure 4.25 demonstrates the realization of such a measurement. Up to a certain threshold

value, P_{out} responds to the φ_{bias} imposed by the pulse amplitude (blue scale). Beyond, a phase slip is generated and the following relaxation is of thermal origin.

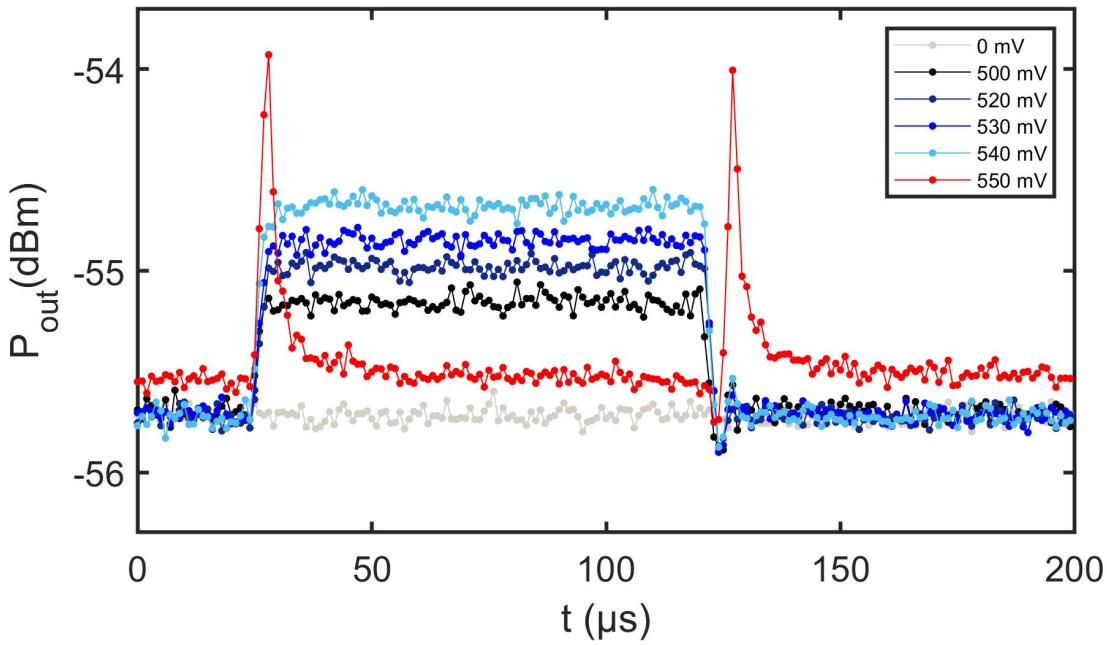

Figure 4.25: Measuring the threshold pulse amplitude for the phase slips. The curves corresponding to the pulse amplitudes below the threshold are marked in gradient of blue. The red curve is the only measurement where the pulse provoked a phase slip.

The real time detection. In the empirical determination of the threshold amplitude, we used long pulses ($t = 100$) μs with 3 μs rise/fall time to facilitate the measurement. Once we obtained the threshold, we narrow the flux pulse duration down to 70 ns. As discussed in Section 4.3, the energy transfer to the quasiparticles after a phase slip takes places in picosecond timescale whereas the following thermal relaxation is in the μ-second range. We set the pulse duration below the sampling period ($T_s = 500$ ns) so that the φ recovers its initial value and is fixed much before the obtention of the first data on the relaxation. This way, we ensure that the calibration curve yields a correct power/temperature conversion. In Fig. 4.26a, we show the real time measurements of the absorber temperature. The fast flux pulse at t=0 generates two consecutive phase slips, one during the forward sweeping branch and the other on the backward, which leads to an abrupt increase of the electronic temperature. To give an example, at $T = 75$ mK, two back to back phase slips caused by the flux pulse deposits $\Delta U \sim 85$ meV of energy on the absorber and increases the temperature by $\Delta T \approx 160$ mK. We repeat the same measurement with the increments of 25 mK up to $T = 275$ mK. Note that the thermal relaxation dynamics accelerates as we increase the temperature thanks to the stronger electron-phonon coupling. Beyond $T = 200$ mK, we are unable to resolve the thermal relaxations at $f_s = 2$ MHz. Figure 4.26b,c focus on the returning to the equilibrium of ΔT at various T_{base}. The nonlinear heat balance equation is solved numerically. Overall, we observe

that the fast decaying initial stage is in good agreement with the relaxation dynamics given by $\Delta\dot{T} \sim \dot{Q}_{e-ph} = \Sigma\mathcal{V}(T_e^n - T_{ph}^n)$ where $n = 4.85$ and $\Sigma = 2.825 \times 10^9$ W K$^{-4.85}$ m^{-3} and $\mathcal{V} \approx 8 \times 10^{-21}$ m^{-3}. In ordered metals, deviations of $\dot{Q}_{e-ph} = \Sigma\mathcal{V}(T_e^n - T_{ph}^n)$ from $n = 5$ are possible in confined absorber geometries where dimensionality plays a role in electron-phonon scattering [206]. In the long-term and only at love tempereatures, we observe a slower relaxation ($\tau \approx 140\,\mu s$) which was already reported for nanoscale copper absorbers [155].

Figure 4.27a plots the initial temperature increase ΔT_0 after a back-and-forth phase slip. ΔT_0 falls down by $\sim 72\%$ between the starting temperatures of 75 mK and 275 mK. This mainly stems from the increasing heat capacity ($\sim T$) of the absorber and the weaker dissipation $\Delta U (\sim I_c\Phi_0)$ which simply follows $I_c(T)$. The calculation used for fitting the data on $\Delta T_0(T)$ assumes a specific heat $\gamma = 71\text{Jm}^{-3}\text{K}^{-2}$ for the copper absorber [155]. As $\delta T \sim T$ goes beyond the linear regime, we integrate the relation $dU = CdT$. Hence, T_{high} following the phase slip is written as

$$T_{high} = \sqrt{\frac{2\Delta U}{\gamma\mathcal{V}} + T_0^2} \tag{4.14}$$

In our calculations, we take into account the asymmetry between the dissipation caused by the forward and backward swept phase slips. As the latter occurs at a higher temperature, the heat release is less important (Fig. 4.27b).

Single shot detection A body which is in thermal contact with a heat reservoir keeps exchanging energy with the reservoir event at equilibrium. The entire thermodynamic system undergoes continual random transitions among its microstates which causes its properties to deviate momentarily their mean values [109]. We can therefore attribute statistical properties to the observables of the system. Likewise, the electron population of the absorber permanently exchanges energy with the phonons in our thermometer. Hence, the electronic temperature (T_e) is subject to fluctuations which is given by the fluctuation-dissipation theorem as $k_B T^2/C$ where C is the absorber heat capacity. In Fig. 4.28, we compare the noise equivalent temperatures (NET) of the relevant signals in our system and we point out the suitable regime for single-shot detection of the individual phase slips. The dashed black line represents the fundamental temperature fluctuations of the absorber which is given as $NET_0 = \sqrt{\frac{2k_b}{5\Sigma\mathcal{V}}}T^{-1}$. The red line corresponds to the required noise equivalent temperature $NET_{req} = \frac{\Delta U}{5\sigma\gamma}T^{-5/2}$ for the observation of individual phase slips. The signal-to-noise ratio is simply defined as $NET_{req}/\max(NET_0, NET_{HEMT})$, where NET_{HEMT} defined as $NET_{HEMT} = \sqrt{\langle\delta T^2\rangle/2\Delta f}$ and Δf is the measurement bandwidth. In an ideal scenario, we would be able to detect the thermal signature of an individual phase slip at $T = 50$ mK with $SNR \approx 22$ dB. However, in reality the electronic noise of the HEMT amplifier severely degrades the SNR. We convert the instrumental noise to $\langle\delta T^2\rangle$ via $\langle\delta T^2\rangle = \mathcal{R}^{-2}\langle\delta P_{out}^2\rangle$. It is seen that the presence of HEMT noise lowers the threshold temperature where $SNR = 1$ for a single phase slip down to ~ 45 mK which is beyond reach in our experimental setup. A possible improvement would be

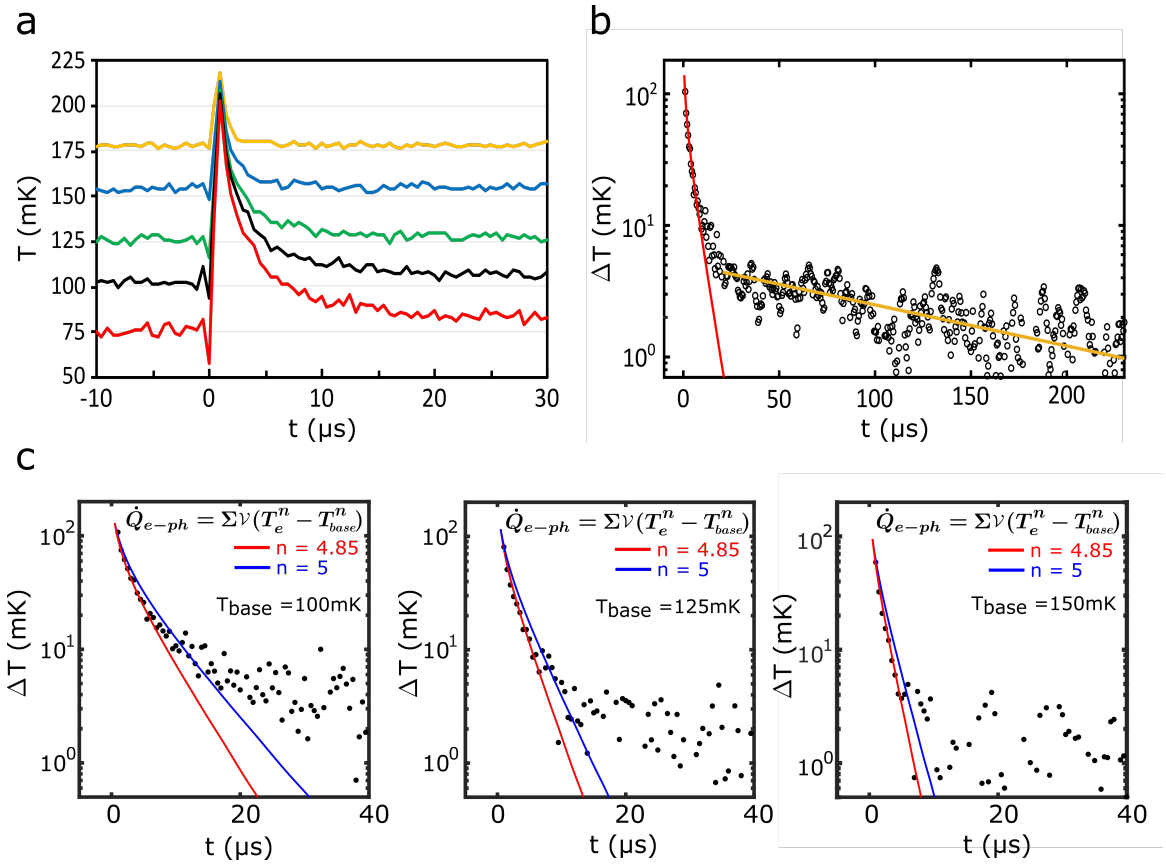

Figure 4.26: ***a.*** *Time-resolved electron temperature in the absorber, at different starting temperatures set by the cryostat bath, following a 70-ns flux pulse at $t = 0$.* ***b.*** *Return to equilibrium $\Delta T(t)$ at 100 mK, following a flux pulse. Same data as the black curve in a., but in a semi-log-scale representation and over a wider time window. The red line is a calculation based on the model discussed in the text, with $n = 4.85$. The yellow line represent the exponential decay with $\tau \approx 140\,\mu s$* ***c.*** *Comparison between the calculated relaxation curves with $n = 4.85$ (red) and $n = 5$ (blue) on the return to equilibrium curves at T= 100 mK, 125 mK and 150 mK.*

to place a Josephson parametric amplifier [207] as a pre-amplifying stage between the sample and the HEMT amplifier. Although operating dominantly in the GHz regime, a JPA tunable between 540 MHz - 640 MHz which provides $\sim$ 18 dB of gain has been reported recently [208]. The incorporation of such an amplifier in our experiment would significantly increase the detection sensitivity. In Fig. 4.28, it is seen that the threshold temperature where $SNR = 1$ goes up to $\sim$ 238 mK and $SNR_{T=50\,mK} \approx 16$ dB which should enable the single-shot detection of individual phase slips in the future.

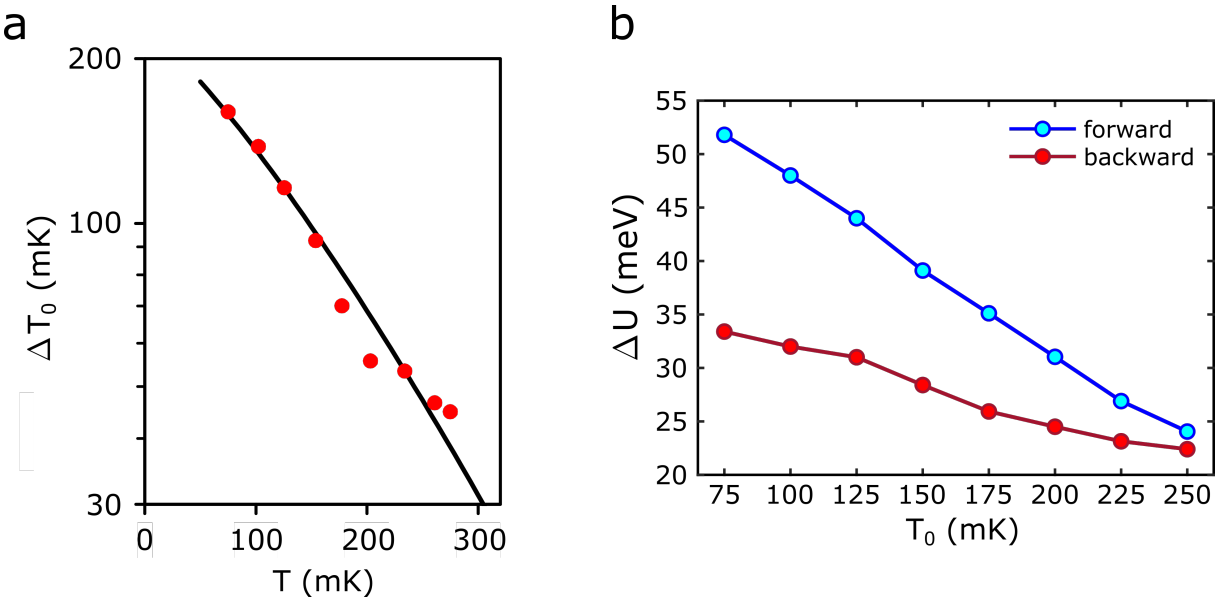

Figure 4.27: ***a.*** *The initial temperature increase ΔT_0 after a back-and-forth phase slip. The calculated $\Delta T_0(T)$ is marked in black.* ***b.*** *The decomposition of ΔT_0 into forward and backward phase slips based on the numerical calculations. The obtaining of $\beta(T)$ allows the calculation the heat deposited during the first phase slip, the temperature reached afterwards and the heat deposited by the secondary phase slip. Backward phase slips deposit less heat as they occur at a higher T_0.*

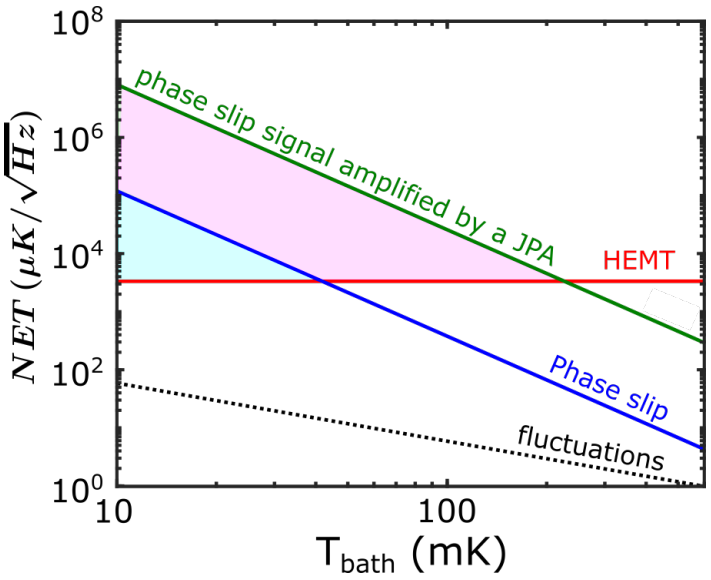

Figure 4.28: The comparison of relevant signals in terms of NET for the single shot detection. The region shaded in light blue corresponds to the regime where a single shot detection is possible with the 4K HEMT amplifier. Including JPA (green), improves the SNR and increases the single-shot regime up to higher temperatures. (shaded pink).

Conclusion

Classical thermodynamics is concerned with the macroscopic consequences of the atomic modes lost in the statistical averaging due to the coarseness of observations [109]. As the quantum devices gain ground, a rethinking of the thermodynamics within the quantum framework grows in parallel. Hence, the fundamental concepts of thermodynamics such as work, dissipation and heat transport as well as the concepts related to the manipulation of information such as Maxwell's demon and Landauer's principle are being reformulated at the quantum level [209–214]. In that regard, the development of the nanoscale thermometers, calorimeters and the novel measurement techniques including fast readout, cross-correlation measurements prove essential to foster the field.

In this thesis, we demonstrated the real-time detection of the tunneling of a magnetic flux quantum (Φ_0) in/out of a hysteretic SQUID. Here, the novelty does not lie in the experimental proof of the flux quantization as it was proven decades ago [77, 78] nor it is in the frontiers of the detection sensitivity as much more sensitive nano-calorimeters already exist [137, 144]. Nevertheless, the real-time detection of the thermal signature of an elementary process ubiquitous to superconducting devices can be considered as a step forward for the field of fast nano-calorimeters. Our demonstration brings together the previously reported concepts of proximity thermometer, fast readout and SQUIPT, and has the potential for further improvement as well as for the alternative uses.

One straight-forward extension would be the study of the thermal properties of the proximitized N used as the calorimeter absorber in our project. Several theoretical reports pointed out the phase dependence of the e-ph scattering rates and the specific heat in N under proximity effect [44, 45, 159]. In principle, it seems possible to investigate these phenomena with our device configuration by generating phase slips and rapidly fixing the phase bias imposed on the SNS junction. This way, one can investigate the time constant which governs the relaxation of the electronic temperature of N as a function of the phase bias on the SNS junction. An alternative experiment can be conceived in the frequency domain which exploits the dependence of the noise spectral density on the phase-dependent thermal conductance. In our setup, we could not achieve the above-mentioned experiments as the influence of the proximity effect on the thermal properties was too small to observe at T = 50 mK. However, the suitable regime is within experimental reach by fine-tuning the device properties and reaching a base temperature $T_{base} \approx 30\,\mathrm{mK}$.

On the material side, copper was chosen mainly for its ease of fabrication and the com-

patibility with the Al superconducting leads. The recent studies on the 2D Van der Waals materials showcases the promising properties of these materials for calorimetry purposes [215–219]. Incorporation of a such material together with the improvements on the amplification chain by introducing quantum limited amplifiers can significantly improve the sensitivity of our device, thereby opening the way for the single shot measurements.
On the long run, the nano-calorimeters might be used for the readout of qubit states [220]. In the standard dispersive readout method, long readout pulses ($\sim \mu$s) are used to achieve an improved SNR. This approach creates a bottleneck for the error-correction schemes where the pulses as short as possible are required to keep the error rates below a certain threshold. Introducing fast-calorimeters capable of detecting single microwave photons in the GHz range where most of the readout transmons operate might bring the readout times to the nanosecond scale.

References

[1] B. Karimi and J. P. Pekola. Noninvasive thermometer based on the zero-bias anomaly of a superconducting junction for ultrasensitive calorimetry. *Physical Review Applied* 10 (5):2018, p. 054048.

[2] B. Karimi et al. Optimized proximity thermometer for ultrasensitive detection. *Physical Review Applied* 13 (5):2020, p. 054001.

[3] B. Karimi et al. Reaching the ultimate energy resolution of a quantum detector. *Nature communications* 11 (1):2020, p. 1–6.

[4] F. Giazotto et al. Superconducting quantum interference proximity transistor. *Nature Physics* 6 (4):2010, p. 254–259.

[5] D. Schmidt, C. Yung, and A. Cleland. Nanoscale radio-frequency thermometry. *Applied physics letters* 83 (5):2003, p. 1002–1004.

[6] S Gasparinetti et al. Fast electron thermometry for ultrasensitive calorimetric detection. *Physical Review Applied* 3 (1):2015, p. 014007.

[7] H. Onnes. The disappearance of the resistivity of mercury, Comm. *Leiden 119b, 120b, 122b, 124c*:1911.

[8] W. Meissner and R. Ochsenfeld. Ein neuer Effekt bei Eintritt der Supraleitfhigkeit. *Die Naturwissenschaften* 21 (44):Nov. 1933, p. 787–788.

[9] F. London, H. London, and F. A. Lindemann. The electromagnetic equations of the supraconductor. *Proceedings of the Royal Society of London. Series A - Mathematical and Physical Sciences* 149 (866):Mar. 1935. Publisher: Royal Society, p. 71–88.

[10] V. Ginzburg and L. Landau. Theory of superconductivity. *Zh. Eksp. Teor. Fiz.(USSR)* 20 (12):1950.

[11] J. Bardeen, L. N. Cooper, and J. R. Schrieffer. Theory of Superconductivity. *Physical Review* 108 (5):Dec. 1957, p. 1175–1204.

[12] L. N. Cooper. Superconductivity in the Neighborhood of Metallic Contacts. *Physical Review Letters* 6 (12):June 1961, p. 689–690.

[13] L. P. Gor'kov. Microscopic derivation of the Ginzburg-Landau equations in the theory of superconductivity. *Sov. Phys. JETP* 9 (6):1959, p. 1364–1367.

[14] L. Gor'kov. The critical supercooling field in superconductivity theory. *Soviet Physics JETP* 10:1960, p. 593–599.

[15] L. Esaki. New Phenomenon in Narrow Germanium p − n Junctions. *Physical Review* 109 (2):Jan. 1958, p. 603–604.

[16] I. Giaever. Electron Tunneling Between Two Superconductors. *Physical Review Letters* 5 (10):Nov. 1960. Publisher: American Physical Society, p. 464–466.

[17] A. Pippard. Experimental analysis of the electronic structure of metals. *Reports on Progress in Physics* 23 (1):1960, p. 176.

[18] B. D. Josephson. Possible new effects in superconductive tunnelling. *Physics Letters* 1 (7):July 1962, p. 251–253.

[19] P. W. Anderson and J. M. Rowell. Probable Observation of the Josephson Superconducting Tunneling Effect. *Physical Review Letters* 10 (6):Mar. 1963. Publisher: American Physical Society, p. 230–232.

[20] K. K. Likharev. Superconducting weak links. *Reviews of Modern Physics* 51 (1):Jan. 1979, p. 101–159.

[21] A. Barone and G. Paterno. *Physics and applications of the Josephson effect*. Volume 1. Wiley Online Library, 1982.

[22] A. A. Golubov, M. Y. Kupriyanov, and E. Il'ichev. The current-phase relation in Josephson junctions. *Reviews of Modern Physics* 76 (2):Apr. 2004, p. 411–469.

[23] P. W. Anderson and A. H. Dayem. Radio-Frequency Effects in Superconducting Thin Film Bridges. *Physical Review Letters* 13 (6):Aug. 1964, p. 195–197.

[24] J. Clarke. Supercurrents in Lead-Copper-Lead Sandwiches. *Proceedings of the Royal Society of London. Series A, Mathematical and Physical Sciences* 308 (1495):1969. Publisher: The Royal Society, p. 447–471.

[25] J. G. Shepherd. Supercurrents Through Thick, Clean S-N-S Sandwiches. *Proceedings of the Royal Society of London. Series A, Mathematical and Physical Sciences* 326 (1566):1972. Publisher: The Royal Society, p. 421–430.

[26] P. G. de Gennes. Boundary Effects in Superconductors. *Reviews of Modern Physics* 36 (1):Jan. 1964. Publisher: American Physical Society, p. 225–237.

[27] V. V. Ryazanov et al. Intrinsically frustrated superconducting array of superconductor-ferromagnet-superconductor π junctions. *Physical Review B* 65 (2):Dec. 2001, p. 020501.

[28] M. G. Blamire and J. W. A. Robinson. The interface between superconductivity and magnetism: understanding and device prospects. *Journal of Physics: Condensed Matter* 26 (45):Nov. 2014, p. 453201.

[29] C. W. J. Beenakker. Specular Andreev Reflection in Graphene. *Physical Review Letters* 97 (6):Aug. 2006, p. 067007.

[30] H. B. Heersche et al. Bipolar supercurrent in graphene. *Nature* 446 (7131):Mar. 2007. Number: 7131 Publisher: Nature Publishing Group, p. 56–59.

[31] V. E. Calado et al. Ballistic Josephson junctions in edge-contacted graphene. *Nature Nanotechnology* 10 (9):Sept. 2015, p. 761–764.

[32] L. Fu and C. L. Kane. Josephson current and noise at a superconductor/quantum-spin-Hall-insulator/superconductor junction. *Physical Review B* 79 (16):Apr. 2009, p. 161408.

[33] M. Z. Hasan and C. L. Kane. *Colloquium* : Topological insulators. *Reviews of Modern Physics* 82 (4):Nov. 2010, p. 3045–3067.

[34] L. Fu and C. L. Kane. Superconducting Proximity Effect and Majorana Fermions at the Surface of a Topological Insulator. *Physical Review Letters* 100 (9):Mar. 2008. Publisher: American Physical Society, p. 096407.

[35] C. W. J. Beenakker. Search for Majorana fermions in superconductors. *Annu. Rev. Condens. Matter Phys.* 4 (1):2013. Publisher: Annual Reviews, p. 113–136.

[36] V. Mourik et al. Signatures of Majorana Fermions in Hybrid Superconductor-Semiconductor Nanowire Devices. *Science* 336 (6084):May 2012, p. 1003–1007.

[37] J. Alicea. New directions in the pursuit of Majorana fermions in solid state systems. *Reports on progress in physics* 75 (7):2012. Publisher: IOP Publishing, p. 076501.

[38] W. C. Stewart. Current-voltage characteristics of josephson junctions. *Applied Physics Letters* 12 (8):Apr. 1968. Publisher: American Institute of Physics, p. 277–280.

[39] D. E. McCumber. Effect of ac impedance on dc voltage-current characteristics of superconductor weak-link junctions. *Journal of Applied Physics* 39 (7):1968. Publisher: American Institute of Physics, p. 3113–3118.

[40] R. Gross and A. Marx. Applied Superconductivity: Josephson Effect and Superconducting Electronics, chapter 3. *Walther-Meissner-Institut, Bayerische Akademie der Wissenschaften*:2005.

[41] D. Nikolic. Spectral Properties and Heat Transport in Mesoscopic Superconducting Circuits. PhD Thesis. Konstanz, 2021.

[42] S. Guéron et al. Superconducting Proximity Effect Probed on a Mesoscopic Length Scale. *Physical Review Letters* 77 (14):Sept. 1996, p. 3025–3028.

[43] H. Le Sueur et al. Phase controlled superconducting proximity effect probed by tunneling spectroscopy. *Physical Review Letters* 100 (19):2008. Publisher: APS, p. 197002.

[44] T. T. Heikkilä and F. Giazotto. Phase sensitive electron-phonon coupling in a superconducting proximity structure. *Physical Review B* 79 (9):Mar. 2009. Publisher: American Physical Society, p. 094514.

[45] H. Rabani et al. Phase-Dependent Electronic Specific Heat in Mesoscopic Josephson Junctions. *Physical Review B* 78 (1):July 2008. arXiv: 0805.0853, p. 012503.

[46] J.-X. Zhu. *Bogoliubov-de Gennes Method and Its Applications*. Volume 924. Lecture Notes in Physics. Springer International Publishing, 2016.

[47] A. Andreev. Thermal conductivity of the intermediate state of superconductors II. *Sov. Phys. JETP* 20:1965, p. 1490.

[48] Y. V. Nazarov and Y. M. Blanter. *Quantum Transport: Introduction to Nanoscience*. Cambridge: Cambridge University Press, 2009.

[49] T. Heikkilä et al. *Superconducting proximity effect in mesoscopic metals*. Helsinki University of Technology, 2002.

[50] F. K. Wilhelm, G. Schön, and A. D. Zaikin. Mesoscopic Superconducting–Normal Metal–Superconducting Transistor. *Physical Review Letters* 81 (8):Aug. 1998, p. 1682–1685.

[51] B. Pannetier and H. Courtois. Andreev Reflection and Proximity effect. *Journal of Low Temperature Physics* 118 (5):Mar. 2000, p. 599–615.

[52] I. Kulik. Macroscopic quantization and the proximity effect in SNS junctions. *Soviet Journal of Experimental and Theoretical Physics* 30:1969, p. 944.

[53] M. Ferrier et al. Phase-dependent Andreev spectrum in a diffusive SNS junction: Static and dynamic current response. *Physical Review B* 88 (17):Nov. 2013, p. 174505.

[54] S. Gueron. Quasiparticles in a diffusive conductor: Interaction and pairing. PhD thesis. Université Pierre et Marie Curie-Paris VI, 1997.

[55] P Dubos et al. Josephson critical current in a long mesoscopic SNS junction. *Physical Review B* 63 (6):2001, p. 064502.

[56] A. M. Black-Schaffer and S. Doniach. Self-consistent solution for proximity effect and Josephson current in ballistic graphene SNS Josephson junctions. *Physical Review B* 78 (2):2008. Publisher: APS, p. 024504.

[57] K. Halterman and M. Alidoust. Josephson currents and spin-transfer torques in ballistic SFSFS nanojunctions. *Superconductor Science and Technology* 29 (5):Mar. 2016. Publisher: IOP Publishing, p. 055007.

[58] M. Hurd, S. Datta, and P. F. Bagwell. Current-voltage relation for asymmetric ballistic superconducting junctions. *Physical Review B* 54 (9):Sept. 1996. Publisher: American Physical Society, p. 6557–6567.

[59] N. Kopnin. *Theory of nonequilibrium superconductivity*. Volume 110. Oxford University Press, 2001.

[60] W. Belzig et al. Quasiclassical Green's function approach to mesoscopic superconductivity. *Superlattices and Microstructures* 25 (5-6):May 1999. arXiv: cond-mat/9812297, p. 1251–1288.

[61] G. Eilenberger. Transformation of Gorkov's equation for type II superconductors into transport-like equations. *Zeitschrift für Physik A Hadrons and nuclei* 214 (2):Apr. 1968, p. 195–213.

[62] K. D. Usadel. Generalized Diffusion Equation for Superconducting Alloys. *Physical Review Letters* 25 (8):Aug. 1970. Publisher: American Physical Society, p. 507–509.

[63] A. de Cecco. Quantum electronics in nanostructures explored by scanning probe microscopy. PhD Thesis. Université Grenoble Alpes, 2018.

[64] D. J. Thouless. Maximum Metallic Resistance in Thin Wires. *Physical Review Letters* 39 (18):Oct. 1977. Publisher: American Physical Society, p. 1167–1169.

[65] T. Matsubara. A new approach to quantum-statistical mechanics. *Progress of theoretical physics* 14 (4):1955. Publisher: Oxford University Press, p. 351–378.

[66] E. Fradkin. The Green's function method in quantum statistics. *Nuclear Physics* 12 (5):1959, p. 465–484.

[67] P. C. Martin and J. Schwinger. Theory of Many-Particle Systems. I. *Physical Review* 115 (6):Sept. 1959. Publisher: American Physical Society, p. 1342–1373.

[68] P. Dubos. Transport électronique dans les nanojonctions supraconducteur-métal normal-supraconducteur. PhD thesis. Université Joseph-Fourier-Grenoble I, 2000.

[69] W. L. McMillan. Tunneling Model of the Superconducting Proximity Effect. *Physical Review* 175 (2):Nov. 1968, p. 537–542.

[70] A. A. Golubov and M. Y. Kupriyanov. Theoretical investigation of Josephson tunnel junctions with spatially inhomogeneous superconducting electrodes. *Journal of Low Temperature Physics* 70 (1):Jan. 1988, p. 83–130.

[71] A. Altland, B. D. Simons, and D. T. Semchuk. Field theory of mesoscopic fluctuations in superconductor-normal-metal systems. *Advances in Physics* 49 (3):May 2000, p. 321–394.

[72] E. Scheer et al. Proximity Effect and Multiple Andreev Reflections in Gold Atomic Contacts. *Physical Review Letters* 86 (2):Jan. 2001, p. 284–287.

[73] H. Le Sueur. Cryogenic AFM-STM for mesoscopic physics. PhD thesis. Université Pierre et Marie Curie-Paris VI, 2007.

[74] J. C. Hammer et al. Density of states and supercurrent in diffusive SNS junctions: role of nonideal interfaces and spin-flip scattering. *Physical Review B* 76 (6):Aug. 2007. arXiv: 0704.2358, p. 064514.

[75] F. Zhou et al. Density of States in Superconductor-Normal Metal-Superconductor Junctions. *Journal of Low Temperature Physics* 110 (3):Feb. 1998, p. 841–850.

[76] R Feynman, R Leighton, and M Sands. The feynman lectures on physics, vol. iii: the new millennium edition: quantum mechanics.

[77] B. S. Deaver and W. M. Fairbank. Experimental Evidence for Quantized Flux in Superconducting Cylinders. *Physical Review Letters* 7 (2):July 1961. Publisher: American Physical Society, p. 43–46.

[78] R. Doll and M. Näbauer. Experimental Proof of Magnetic Flux Quantization in a Superconducting Ring. *Physical Review Letters* 7 (2):July 1961. Publisher: American Physical Society, p. 51–52.

[79] Y. Aharonov and D. Bohm. Significance of Electromagnetic Potentials in the Quantum Theory. *Physical Review* 115 (3):Aug. 1959. Publisher: American Physical Society, p. 485–491.

[80] J. F. Annett et al. *Superconductivity, superfluids and condensates*. Volume 5. Oxford University Press, 2004.

[81] K. Matveev, A. Larkin, and L. Glazman. Persistent current in superconducting nanorings. *Physical Review Letters* 89 (9):2002, p. 096802.

[82] K. Y. Arutyunov, D. S. Golubev, and A. D. Zaikin. Superconductivity in one dimension. *Physics Reports* 464 (1-2):2008, p. 1–70.

[83] V. A. Kashurnikov et al. Supercurrent states in one-dimensional finite-size rings. *Physical Review B* 53 (19):May 1996, p. 13091–13105.

[84] F. W. J. Hekking and L. I. Glazman. Quantum fluctuations in the equilibrium state of a thin superconducting loop. *Physical Review B* 55 (10):Mar. 1997, p. 6551–6558.

[85] D. S. Golubev and A. D. Zaikin. Quantum tunneling of the order parameter in superconducting nanowires. *Physical Review B* 64 (1):June 2001, p. 014504.

[86] J. Lukens, R. Warburton, and W. Webb. Onset of quantized thermal fluctuations in" one-dimensional" superconductors. *Physical Review Letters* 25 (17):1970, p. 1180.

[87] R. Newbower, M. Beasley, and M Tinkham. Fluctuation effects on the superconducting transition of tin whisker crystals. *Physical Review B* 5 (3):1972, p. 864.

[88] J. S. Langer and V. Ambegaokar. Intrinsic Resistive Transition in Narrow Superconducting Channels. *Physical Review* 164 (2):Dec. 1967, p. 498–510.

[89] H. Grabert and U. Weiss. Crossover from Thermal Hopping to Quantum Tunneling. *Physical Review Letters* 53 (19):Nov. 1984. Publisher: American Physical Society, p. 1787–1790.

[90] N. Giordano and E. Schuler. Macroscopic quantum tunneling and related effects in a one-dimensional superconductor. *Physical Review Letters* 63 (21):Nov. 1989, p. 2417–2420.

[91] A. Bezryadin, C. Lau, and M Tinkham. Quantum suppression of superconductivity in ultrathin nanowires. *Nature* 404 (6781):2000, p. 971–974.

[92] C. N. Lau et al. Quantum Phase Slips in Superconducting Nanowires. *Physical Review Letters* 87 (21):Nov. 2001, p. 217003.

[93] J. S. Lehtinen et al. Evidence of quantum phase slip effect in titanium nanowires. *Physical Review B* 85 (9):Mar. 2012. Publisher: American Physical Society, p. 094508.

[94] O. Astafiev et al. Coherent quantum phase slip. *Nature* 484 (7394):2012, p. 355–358.

[95] J. T. Peltonen et al. Coherent flux tunneling through NbN nanowires. *Physical Review B* 88 (22):Dec. 2013, p. 220506.

[96] C. H. Webster et al. NbSi nanowire quantum phase-slip circuits: dc supercurrent blockade, microwave measurements, and thermal analysis. *Physical Review B* 87 (14):Apr. 2013, p. 144510.

[97] J. E. Mooij et al. Josephson Persistent-Current Qubit. *Science* 285 (5430):Aug. 1999. Publisher: American Association for the Advancement of Science, p. 1036–1039.

[98] I. M. Pop et al. Measurement of the effect of quantum phase slips in a Josephson junction chain. *Nature Physics* 6 (8):Aug. 2010. Number: 8 Publisher: Nature Publishing Group, p. 589–592.

[99] V. E. Manucharyan et al. Fluxonium: Single Cooper-Pair Circuit Free of Charge Offsets. *Science* 326 (5949):Oct. 2009. Publisher: American Association for the Advancement of Science, p. 113–116.

[100] A. Ergül et al. Localizing quantum phase slips in one-dimensional Josephson junction chains. *New Journal of Physics* 15 (9):Sept. 2013, p. 095014.

[101] R. C. Jaklevic et al. Quantum Interference Effects in Josephson Tunneling. *Physical Review Letters* 12 (7):Feb. 1964, p. 159–160.

[102] J. Clarke. Superconducting quantum interference devices for low frequency measurements. *Superconductor applications: SQUIDs and machines*. Springer, 1977, p. 67–124.

[103] J. E. Zimmerman, P. Thiene, and J. T. Harding. Design and Operation of Stable rf-Biased Superconducting Point-Contact Quantum Devices, and a Note on the Properties of Perfectly Clean Metal Contacts. *Journal of Applied Physics* 41 (4):Mar. 1970. Publisher: American Institute of Physics, p. 1572–1580.

[104] J. E. Mercereau. Superconducting magnetometers. *Revue de Physique Appliquée* 5 (1):Feb. 1970. Publisher: Société Française de Physique, p. 13–20.

[105] M. Nisenoff. Superconducting magnetometers with sensitivities approaching 10 -10 gauss. *Revue de Physique Appliquée* 5 (1):Feb. 1970. Publisher: Société Française de Physique, p. 21–24.

[106] R. P. Giffard, R. A. Webb, and J. C. Wheatley. Principles and methods of low-frequency electric and magnetic measurements using an rf-biased point-contact superconducting device. *Journal of Low Temperature Physics* 6 (5):1972. Publisher: Springer, p. 533–610.

[107] J. P. Pekola et al. Calorimetric measurement of work in a quantum system. *New Journal of Physics* 15 (11):2013, p. 115006.

[108] J. P. Pekola. Towards quantum thermodynamics in electronic circuits. *Nature Physics* 11 (2):2015, p. 118–123.

[109] H. B. Callen. Thermodynamics and an Introduction to Thermostatistics. 1998.

[110] L. D. Landau and E. M. Lifshitz. *Statistical Physics: Volume 5*. Volume 5. Elsevier, 2013.

[111] T. J. Quinn. *Temperature*. Academic press, 2013.

[112] H. D. Young et al. *University physics*. Volume 9. Addison-Wesley Reading, MA, 1996.

[113] F. Pobell. *Matter and methods at low temperatures*. Springer Science & Business Media, 2007.

[114] J. Pekola et al. Thermometry by arrays of tunnel junctions. *Physical Review Letters* 73 (21):1994, p. 2903.

[115] S. Farhangfar et al. One dimensional arrays and solitary tunnel junctions in the weak Coulomb blockade regime: CBT thermometry. *Journal of low temperature physics* 108 (1):1997, p. 191–215.

[116] M. Meschke et al. Electron thermalization in metallic islands probed by coulomb blockade thermometry. *Journal of low temperature physics* 134 (5):2004, p. 1119–1143.

[117] J. Pekola. Trends in thermometry. *Journal of low temperature physics* 135 (5):2004, p. 723–744.

[118] Y. M. Blanter and M. Büttiker. Shot noise in mesoscopic conductors. *Physics reports* 336 (1-2):2000, p. 1–166.

[119] L. Rubin, B. Brandt, and H. Sample. Cryogenic thermometry: a review of recent progress, II. *Cryogenics* 22 (10):1982, p. 491–503.

[120] J Fischer and B Fellmuth. Temperature metrology. *Reports on progress in physics* 68 (5):2005, p. 1043.

[121] S. Saito and T. Sato. Matsushita carbon resistors as thermometers for use at low temperatures and in high fields. *Review of Scientific Instruments* 46 (9):1975, p. 1226–1230.

[122] I Bat'ko et al. Design of RuO2-based thermometers for the millikelvin temperature range. *Cryogenics* 35 (2):1995, p. 105–108.

[123] C. Enss and S. Hunklinger. *Low-temperature physics*. Springer Science & Business Media, 2005.

[124] L. Pascal. Electronic refrigeration and thermal couplings in supraconductor hybrid devices. PhD thesis. Université de Grenoble, 2012.

[125] B. Dutta. Energetics in metallic-island and quantum-dot based single-electron devices. PhD thesis. Université Grenoble Alpes, 2018.

[126] S. Rajauria et al. Andreev current-induced dissipation in a hybrid superconducting tunnel junction. *Physical Review Letters* 100 (20):2008, p. 207002.

[127] J. P. Pekola et al. Limitations in cooling electrons using normal-metal-superconductor tunnel junctions. *Physical Review Letters* 92 (5):2004, p. 056804.

[128] H. Courtois et al. Origin of hysteresis in a proximity Josephson junction. *Physical Review Letters* 101 (6):2008, p. 067002.

[129] E. Burstein and S. Lundqvist. *Tunneling phenomena in solids*. Springer, 1969.

[130] J. Rowell and L. Shen. Zero-bias anomalies in normal metal tunnel junctions. *Physical Review Letters* 17 (1):1966, p. 15.

[131] G. L. Pilbratt. Herschel mission: status and observing opportunities. *Optical, Infrared, and Millimeter Space Telescopes*. Volume 5487. SPIE. 2004, p. 401–412.

[132] A. Poglitsch et al. The photodetector array camera and spectrometer (PACS) on the Herschel space observatory. *Astronomy & astrophysics* 518:2010, p. L2.

[133] P. W. Graham et al. Experimental searches for the axion and axion-like particles. *Annual Review of Nuclear and Particle Science* 65:2015, p. 485–514.

[134] J. Wei et al. Ultrasensitive hot-electron nanobolometers for terahertz astrophysics. *Nature nanotechnology* 3 (8):2008, p. 496–500.

[135] D. L. Woolard et al. Terahertz frequency sensing and imaging: A time of reckoning future applications? *Proceedings of the IEEE* 93 (10):2005, p. 1722–1743.

[136] A. K. Sood et al. Development of low dark current SiGe-detector arrays for visible-NIR Imaging Sensor. *Infrared Technology and Applications XXXV*. Volume 7298. SPIE. 2009, p. 1262–1272.

[137] R. Kokkoniemi et al. Bolometer operating at the threshold for circuit quantum electrodynamics. *Nature* 586 (7827):2020, p. 47–51.

[138] P. Richards. Bolometers for infrared and millimeter waves. *Journal of Applied Physics* 76 (1):1994, p. 1–24.

[139] J.-J. Yon, E. Mottin, and J.-L. Tissot. Latest amorphous silicon microbolometer developments at LETI LIR. *Infrared technology and Applications XXXIV*. Volume 6940. SPIE. 2008, p. 631–638.

[140] B. Wang et al. Nanostructured vanadium oxide thin film with high TCR at room temperature for microbolometer. *Infrared Physics & Technology* 57:2013, p. 8–13.

[141] U. Perera. *Bolometers*. Intechopen, 2012.

[142] K. Inomata et al. Single microwave-photon detector using an artificial Λ-type three-level system. *Nature communications* 7 (1):2016, p. 1–7.

[143] N. Du et al. Search for invisible axion dark matter with the axion dark matter experiment. *Physical Review Letters* 120 (15):2018, p. 151301.

[144] R. Kokkoniemi et al. Nanobolometer with ultralow noise equivalent power. *Communications Physics* 2 (1):2019, p. 1–8.

[145] H. Jung et al. Design and characteristics of a-Si-based micro-bolometers with shared-anchor structure in vacuum packaged systems. *Microsystem technologies* 20 (4):2014, p. 899–905.

[146] V Goudon et al. Design and fabrication of cooled silicon bolometers for mm wave detection. *Nuclear Instruments and Methods in Physics Research Section A: Accelerators, Spectrometers, Detectors and Associated Equipment* 912:2018, p. 78–81.

[147] A Aliane et al. Superconducting Ti/TiN thin films for mm-wave absorption. *Journal of Low Temperature Physics* 193 (5):2018, p. 655–660.

[148] L Dussopt et al. High-Impedance Surfaces for Above-IC Integration of Cooled Bolometer Arrays at the 350-μm Wavelength. *Journal of Low Temperature Physics*:2022, p. 1–6.

[149] F. Brange et al. Nanoscale quantum calorimetry with electronic temperature fluctuations. *Physical Review B* 98 (20):2018, p. 205414.

[150] G.-H. Lee et al. Graphene-based Josephson junction microwave bolometer. *Nature* 586 (7827):2020, p. 42–46.

[151] R. Lescanne et al. Irreversible qubit-photon coupling for the detection of itinerant microwave photons. *Physical Review X* 10 (2):2020, p. 021038.

[152] Z. Wang et al. Single electron-spin-resonance detection by microwave photon counting. *arXiv preprint arXiv:2301.02653*:2023.

[153] T. Van Duzer and C. W. Turner. Principles of superconductive devices and circuits:1981.

[154] F. Wellstood, C Urbina, and J. Clarke. Hot-electron effects in metals. *Physical Review B* 49 (9):1994, p. 5942.

[155] K. Viisanen and J. Pekola. Anomalous electronic heat capacity of copper nanowires at sub-kelvin temperatures. *Physical Review B* 97 (11):2018, p. 115422.

[156] A Sergeev and V Mitin. Electron-phonon interaction in disordered conductors: Static and vibrating scattering potentials. *Physical Review B* 61 (9):2000, p. 6041.

[157] P Kivinen et al. Electron–phonon heat transport and electronic thermal conductivity in heavily doped silicon-on-insulator film. *Journal of applied physics* 94 (5):2003, p. 3201–3205.

[158] M. Gershenson et al. Millisecond electron–phonon relaxation in ultrathin disordered metal films at millikelvin temperatures. *Applied Physics Letters* 79 (13):2001, p. 2049–2051.

[159] D. Nikolić, D. M. Basko, and W. Belzig. Electron cooling by phonons in superconducting proximity structures. *Physical Review B* 102 (21):2020, p. 214514.

[160] P. Koppinen and I. Maasilta. Phonon cooling of nanomechanical beams with tunnel junctions. *Physical Review Letters* 102 (16):2009, p. 165502.

[161] J. Muhonen et al. Electronic cooling of a submicron-sized metallic beam. *Applied Physics Letters* 94 (7):2009, p. 073101.

[162] A. Clark et al. Cooling of bulk material by electron-tunneling refrigerators. *Applied Physics Letters* 86 (17):2005, p. 173508.

[163] A. Luukanen et al. On-chip refrigeration by evaporation of hot electrons at subkelvin temperatures. *Journal of low temperature physics* 120 (3):2000, p. 281–290.

[164] L. Pascal et al. Existence of an independent phonon bath in a quantum device. *Physical Review B* 88 (10):2013, p. 100502.

[165] S. Rajauria et al. Electron and phonon cooling in a superconductor–normal-metal–superconductor tunnel junction. *Physical Review Letters* 99 (4):2007, p. 047004.

[166] E. T. Swartz and R. O. Pohl. Thermal boundary resistance. *Reviews of modern physics* 61 (3):1989, p. 605.

[167] A. Abrikosov. *Fundamentals of the Theory of Metals*. Courier Dover Publications, 2017.

[168] D. Saha and T. G. Birdsall. Quadrature-quadrature phase-shift keying. *IEEE Transactions on Communications* 37 (5):1989, p. 437–448.

[169] K. L. Viisanen et al. Incomplete measurement of work in a dissipative two level system. *New Journal of Physics* 17 (5):2015, p. 055014.

[170] S. Gasparinetti et al. Dissipation at the Nanoscale: Cooper-pair Pumping and Electron Thermometry. PhD thesis. 2014.

[171] B. Karimi et al. Observing temperature fluctuations of a mesoscopic electron system. *arXiv preprint arXiv:1904.05041*:2019.

[172] C Berdou et al. One hundred second bit-flip time in a two-photon dissipative oscillator. *arXiv preprint arXiv:2204.09128*:2022.

[173] M. Göppl et al. Coplanar waveguide resonators for circuit quantum electrodynamics. *Journal of Applied Physics* 104 (11):2008, p. 113904.

[174] A. Wallraff et al. Approaching unit visibility for control of a superconducting qubit with dispersive readout. *Physical review letters* 95 (6):2005, p. 060501.

[175] B. Abdo et al. Nonlinear dynamics in the resonance line shape of NbN superconducting resonators. *Physical Review B* 73 (13):2006, p. 134513.

[176] C. Theodorou and G. Ghibaudo. Low-frequency noise and random telegraph noise in nanoscale devices: modeling and impact on circuit operation. *25th International Conference on Noise and Fluctuations ICNF 2019*. 2019.

[177] R. L. Kautz and J. M. Martinis. Noise-affected I-V curves in small hysteretic Josephson junctions. *Physical Review B* 42 (16):1990, p. 9903.

[178] V. Ambegaokar, B. Halperin, and J. Langer. Hopping conductivity in disordered systems. *Physical review B* 4 (8):1971, p. 2612.

[179] T. Fulton and L. Dunkleberger. Lifetime of the zero-voltage state in Josephson tunnel junctions. *Physical Review B* 9 (11):1974, p. 4760.

[180] R. F. Voss and R. A. Webb. Macroscopic quantum tunneling in 1-μm Nb Josephson junctions. *Physical Review Letters* 47 (4):1981, p. 265.

[181] A. O. Caldeira and A. J. Leggett. Influence of dissipation on quantum tunneling in macroscopic systems. *Physical Review Letters* 46 (4):1981, p. 211.

[182] A. Garg. Escape-field distribution for escape from a metastable potential well subject to a steadily increasing bias field. *Physical Review B* 51 (21):1995, p. 15592.

[183] F. Tafuri, editor. *Fundamentals and Frontiers of the Josephson Effect*. Volume 286. Springer Series in Materials Science. Cham: Springer International Publishing, 2019.

[0] J. A. Blackburn, M. Cirillo, and N. Grønbech-Jensen. Switching current distributions in Josephson junctions at very low temperatures. *EPL (Europhysics Letters)* 107 (6):2014, p. 67001.

[185] K. K. Likharev. *Dynamics of Josephson junctions and circuits*. Routledge, 2022.

[186] D. Schmidt, R. Schoelkopf, and A. Cleland. Photon-mediated thermal relaxation of electrons in nanostructures. *Physical Review Letters* 93 (4):2004, p. 045901.

[187] M. Meschke, W. Guichard, and J. P. Pekola. Single-mode heat conduction by photons. *Nature* 444 (7116):2006, p. 187–190.

[188] A. V. Timofeev et al. Electronic refrigeration at the quantum limit. *Physical Review Letters* 102 (20):2009, p. 200801.

[189] S. Jezouin et al. Quantum limit of heat flow across a single electronic channel. *Science* 342 (6158):2013, p. 601–604.

[190] S. S. Mohan et al. Simple accurate expressions for planar spiral inductances. *IEEE Journal of solid-state circuits* 34 (10):1999, p. 1419–1424.

[191] A. Glezer Moshe, E. Farber, and G. Deutscher. Granular superconductors for high kinetic inductance and low loss quantum devices. *Applied Physics Letters* 117 (6):2020, p. 062601.

[192] P. Coumou et al. Electrodynamic response and local tunneling spectroscopy of strongly disordered superconducting TiN films. *Physical Review B* 88 (18):2013, p. 180505.

[193] H. l. Sueur et al. Microscopic charged fluctuators as a limit to the coherence of disordered superconductor devices. *arXiv preprint arXiv:1810.12801*:2018.

[194] W. Zhang et al. Microresonators fabricated from high-kinetic-inductance aluminum films. *Physical Review Applied* 11 (1):2019, p. 011003.

[195] A. J. Kerman. Metastable superconducting qubit. *Physical Review Letters* 104 (2):2010, p. 027002.

[196] J. Peltonen et al. Hybrid rf SQUID qubit based on high kinetic inductance. *Scientific reports* 8 (1):2018, p. 1–8.

[197] N. A. Masluk et al. Microwave characterization of Josephson junction arrays: Implementing a low loss superinductance. *Physical Review Letters* 109 (13):2012, p. 137002.

[198] P. Winkel et al. Nondegenerate parametric amplifiers based on dispersion-engineered Josephson-junction arrays. *Physical Review Applied* 13 (2):2020, p. 024015.

[199] P. Dubos et al. Coherent Low-Energy Charge Transport in a Diffusive S-N-S Junction. *Physical Review Letters* 87 (20):Oct. 2001, p. 206801.

[200] H Courtois et al. Long-range coherence in a mesoscopic metal near a superconducting interface. *Physical Review Letters* 76 (1):1996, p. 130.

[201] M. E. Ware. Flux-tunable superconducting transmons for quantum information processing. PhD thesis. Syracuse University, 2015.

[202] S. Richer et al. Inductively shunted transmon qubit with tunable transverse and longitudinal coupling. *Physical Review B* 96 (17):2017, p. 174520.

[203] R. Lescanne et al. Exponential suppression of bit-flips in a qubit encoded in an oscillator. *Nature Physics* 16 (5):2020, p. 509–513.

[204] J Claudon et al. Coherent oscillations in a superconducting multilevel quantum system. *Physical Review Letters* 93 (18):2004, p. 187003.

[205] A. V. Oppenheim and R. W. Schafer. Digital signal processing(Book). *Research supported by the Massachusetts Institute of Technology, Bell Telephone Laboratories, and Guggenheim Foundation. Englewood Cliffs, N. J., Prentice-Hall, Inc., 1975. 598 p*:1975.

[206] J. Karvonen and I. Maasilta. Influence of phonon dimensionality on electron energy relaxation. *Physical Review Letters* 99 (14):2007, p. 145503.

[207] T. Yamamoto et al. Flux-driven Josephson parametric amplifier. *Applied Physics Letters* 93 (4):2008, p. 042510.

[208] S. Simbierowicz et al. A flux-driven Josephson parametric amplifier for sub-GHz frequencies fabricated with side-wall passivated spacer junction technology. *Superconductor Science and Technology* 31 (10):2018, p. 105001.

[209] C. Elouard, M. Richard, and A. Auffèves. Reversible work extraction in a hybrid opto-mechanical system. *New Journal of Physics* 17 (5):2015, p. 055018.

[210] P. P. Hofer and B. Sothmann. Quantum heat engines based on electronic Mach-Zehnder interferometers. *Physical Review B* 91 (19):2015, p. 195406.

[211] J. P. Pekola and B. Karimi. Colloquium: Quantum heat transport in condensed matter systems. *Reviews of Modern Physics* 93 (4):2021, p. 041001.

[212] N. Cottet et al. Observing a quantum Maxwell demon at work. *Proceedings of the National Academy of Sciences* 114 (29):2017, p. 7561–7564.

[213] A. Bérut et al. Experimental verification of Landauer's principle linking information and thermodynamics. *Nature* 483 (7388):2012, p. 187–189.

[214] M. P. Blencowe and V. Vitelli. Universal quantum limits on single-channel information, entropy, and heat flow. *Physical Review A* 62 (5):2000, p. 052104.

[215] M. A. Aamir et al. Ultrasensitive Calorimetric Measurements of the Electronic Heat Capacity of Graphene. *Nano Letters* 21 (12):2021, p. 5330–5337.

[216] M. Polini et al. Materials and devices for fundamental quantum science and quantum technologies. *arXiv preprint arXiv:2201.09260*:2022.

[217] J. Waissman et al. Electronic thermal transport measurement in low-dimensional materials with graphene non-local noise thermometry. *Nature Nanotechnology* 17 (2):2022, p. 166–173.

[218] E. Y. Andrei et al. The marvels of moiré materials. *Nature Reviews Materials* 6 (3):2021, p. 201–206.

[219] G Di Battista et al. Revealing the ultra-sensitive calorimetric properties of superconducting magic-angle twisted bilayer graphene. *arXiv preprint arXiv:2111.08735*:2021.

[220] J. P. Pekola and B. Karimi. Ultrasensitive calorimetric detection of single photons from qubit decay. *Physical Review X* 12 (1):2022, p. 011026.